

LOW-LYING DIPOLE STRENGTH IN ^{20}O

By

Erik J. Tryggestad

A DISSERTATION

Submitted to
Michigan State University
in partial fulfillment of the requirements
for the degree of

DOCTOR OF PHILOSOPHY

Department of Physics and Astronomy

2001

ABSTRACT

LOW-LYING DIPOLE STRENGTH IN ^{20}O

By

Erik J. Tryggestad

Theoretical calculations suggest that a significant fraction of dipole ($E1$) strength is shifted towards lower excitation energies in neutron-rich nuclei. The availability of fast radioactive beams allows the possibility for probing the $E1$ strength function in unstable nuclei via Coulomb excitation. Therefore, we have performed two experiments at the NSCL at Michigan State University to investigate low-lying $E1$ strength in both ^{18}O and ^{20}O via virtual photon scattering. 100 MeV/u beams of $^{18,20}\text{O}$ impinged on a 30 mg/cm² enriched ^{208}Pb target. De-excitation γ -rays were detected with the large ORNL-TAMU-MSU BaF₂ array placed at forward angles. The γ -ray energies were Doppler-corrected and a nearest neighbor add-back was performed, improving the response of the array. The γ -ray energy was correlated with projectile energy-loss measured with the S800 spectrograph. γ -rays having (projectile-frame) energies between 1 and 8 MeV were collected for both ^{18}O and ^{20}O .

Monte Carlo simulations which have utilized the radiation detection code GEANT while incorporating known information for ^{18}O and theoretical predictions for ^{20}O were used to make direct comparisons with the experimental results. The analysis reveals that the observed excitation function for ^{20}O is dominated by transitions resulting from $E1$ excitations, while that for ^{18}O is dominated by decays following $E2$ excitations. We have established the existence of two previously unmeasured ^{20}O 1^- levels at 5.35 and 6.85 MeV. The γ -decay branching from these states has been approximately determined, while $B(E1)$ information has also been extracted. Specifically, $B(E1; 0.00 \rightarrow 5.35) \uparrow \geq 0.062 e^2 \text{ fm}^2$, while $B(E1; 0.00 \rightarrow 6.85) \uparrow \geq 0.035 e^2 \text{ fm}^2$.

To Grandpa

ACKNOWLEDGMENTS

Alas, it has recently been discovered that the experience of finishing a Ph.D. is rather anticlimactic. From time to time I have had visions of what it would be like being a “Dr.” – so far I have to say that it is not all it’s cracked up to be. The achievement of this esteemed title, while not intensely thrilling, has, nevertheless, been personally rewarding. I am indebted to so many for their support over the years, both academic and personal.

First and foremost I would like to acknowledge my advisor, Dr. Michael Thoenessen. Thanks, Mike, for taking me on as a student. Perhaps it was good that you weren’t aware of what you were getting yourself into at the time! Thanks also for your patient guidance all throughout my naive experimental and data-analysis journeys. Your relatively relaxed approach to mentoring is one which has been ideal for my personality and also for my problem-solving development. A warm thanks to my experimental collaborators, from here, ORNL, and abroad. I hope I’ll have the opportunity to work with you again soon! Thanks also to my pre-advisor, Dr. Aaron Galonsky, who first introduced me to the world of nuclear physics when I came to the lab as an R.E.U. intern. I had a wonderful time that summer of ’95 working with you, your students and with your neutron-wall collaborators from Hungary and Japan. It was indeed a worldly experience. I would also like to thank Dr. Thomas Baumann, for his always-enthusiastic help with so many of my recent struggles, especially thesis formatting questions. Thomas, thanks for putting up with me – you are a god of PAW and L^AT_EX.

I owe a special thank-you to the NSCL computer department and support staff. The great work you guys do every day is what makes this place run smoothly. From day-1 I was impressed with the open atmosphere at the lab. People here are always willing to help solve your problem, which provides for a very friendly and professional

environment. I must also acknowledge the financial support for this study which came from the N.S.F.

I would also like to thank certain physics professors at M.S.U., namely Dr. Stump, Dr. Repko, Dr. Mahanti and (especially) Dr. Zelevinsky for their lecturing abilities and teaching philosophies which allowed for stimulating courses at a time in my life when I was most-exhausted mentally! Thank you for sharing your talents!

I owe a wealth of gratitude to the graduate students at the NSCL who, daily, provide a wonderful, friendly and stimulating environment that is a joy to be a part of. Thanks (in order of their graduation) to old-timers Jack Caggiano, Heiko Scheit, Jon Kruse, Don Anthony, Valentina Maddalena, Barry Davids and Marcus Chromik. Together you represent the old-school breed which the newer generations here strive to emulate! Thank you, Jon, for being my first friend here, and introducing me to everything I had to know to get by. For example, Jon, you introduced me to the Peanut Barrel, to the Beastie Boys (re-introduction), to Spartan sorry-football, to silicon detectors and oscilloscope etiquette, to Bells Oberon (Black Label too), to fly fishing, to espresso, to peanut-butter chili...need I go on?? Thanks for convincing me to come to M.S.U. Thanks also for having me usher at your wedding to Jodi, despite my bad haircut at the time. You two are one of the coolest couples that I know – I hope to stay in touch. Jon, Jack, Heiko, Valentina and Barry, especially Barry, thanks for putting up with my incessant pestering regarding questions of physics. Without folks like you around I wouldn't be where I am today. On a more personal note, Barry, thanks, also, for introducing me to the superiority of pressed coffee, and for sharing my undying enthusiasm for the International Bread Company. Cheers to the Bumstead! Don, once god-father of the laboratory, thanks for your conversation, for your witty attitude, your advice, for your love of beer and food, and for marrying Poala! I aspire to fix up an old house and throw dinner parties of the caliber that you and your wife have established. Don, beware of the screen! Marcus, fellow “big-ugly,”

thanks for all the fun times we've had over the years. Thanks for helping me with my thesis experiment. I was lucky to be able to take part in your thesis experiment here, from which I gained invaluable experience such as how to align a beam pipe properly by making use of a 2x4. Thanks for looking sad enough to get us free court-side seats to the 1999 season, big-ten basketball closer against Wisconsin (A-J-Granger!). Thanks for participating in ENAM and Euroschool with me, these were fun times. I promise I will share any royalties, 50-50, that are received from the "Big Ugly's Chicken Experience" which will soon be an enticing contribution to the sandwich entourage at the Peanut Barrel.

And as for the current graduate posse here at the lab, consisting of honorable folks such as Joann Prisciandaro, Daniel Groh, Ben Perry, Jeremy Seitz, Mark Wallace, Declan Mulhall, Ryan Clement, Chris Freigang, Paul Heckman, Pat Lofy and Katie Miller – thanks for being the delightful people that you are! Special thanks to my office mates Paul, Dan, and Ben for putting up with me. Ben, I'm sorry I called you "Benjamin," and I dig that blond hair. Huge thanks also to my group-mate Paul for all of the left-wing conversations, for helping me with my painful analysis (I hope I have provided you with some help also), and for loaning me the golf clubs! Thanks to Mark Wallace for his interest and ability in the sport of volleyball. (No, I'm not available on Monday to sub.) And finally, thanks to Pat for his enthusiasm, his perpetual high-and-tight hair cut, and his impromptu D.J.-ing abilities. Pat, it wasn't the same without you at our last party..."oh yeah, that's the spot!" Thanks for organizing all the softball over the years, it's been an honor to proudly display the name "Art's" on my chest with the bold "00" on my back.

Thanks so much to my family, who have always been so supportive of me in my academic pursuits. While you, Mom and Dad, Søren and Maia, may not have always understood my love of physics, nor felt like you could communicate with me about the details of my studies, you have always acknowledged me by way of your love and

by your pride, both vocal and demonstrated. Mom and Dad, you have taught me how to think and how to set goals for myself. Now you have to listen to me complain about not knowing what to do with the rest of my life!

Finally, I must also thank the newest, most-important addition to my life, my dearest Angela! While you may not think that you have contributed, you've said as much just yesterday in fact, this is most assuredly not the case. Just being able to come home to you at the end of every day, to sit with you and vent-away the stress from hours spent sitting in front of this very computer terminal, both in conversation and in silence, has made me a very lucky person. You are there for me every day, all the time. My new life with you has helped me to put all other goals into a humbled perspective. Because of you, my days on this earth are taken for granted much less-often, and this gets right down to the meaning of life. My love, I am so looking forward to our future ventures together.

Contents

1	Introduction	1
1.1	Experimental motivation	2
1.2	Coulomb excitation	5
1.3	Accessible states in ^{18}O	8
1.4	^{208}Pb contributions	10
1.5	Status of ^{20}O spectroscopy and shell model predictions	11
2	Experimental details	13
2.1	The S800 spectrometer	15
2.1.1	Position-sensitive CRDC detectors	17
2.1.2	Ionization chamber and scintillation detectors	19
2.1.3	S800 electronics	19
2.2	The ORNL-TAMU-MSU BaF_2 Array	21
2.2.1	Detector construction	22
2.2.2	BaF_2 properties	23
2.2.3	BaF_2 electronics	23
3	Experimental data analysis	27
3.1	Projectile analysis with the S800	27
3.1.1	^{18}O and ^{20}O identification	27
3.1.2	CRDC mask calibration	30
3.1.3	Corrections to S800 parameters	31
3.1.4	Effects of the beam blocker on $\theta_{f,t}$	35
3.2	γ -ray analysis with the ORNL-TAMU-MSU BaF_2 Array	36
3.2.1	Energy calibration	36
3.2.2	Background suppression	39
3.2.3	Shower reconstruction	43
3.2.4	Doppler correction	46
3.3	Beam rate monitoring with the MCP detectors	48
3.4	Experimental results	49
3.4.1	Random background removal	49
3.4.2	S800– BaF_2 energy correlation	49
3.4.3	^{18}O and ^{20}O strength distributions	51
3.4.4	^{18}O and ^{20}O angular distributions	53

4	Interpretation of experimental results	55
4.1	The simulation	56
4.1.1	Selection of the excitation channel	56
4.1.2	Selection of the de-excitation path	58
4.1.3	Projectile scattering	59
4.1.4	γ -ray decay	61
4.1.5	Simulating BaF ₂ detector response	64
4.1.6	Simulating S800 response	70
4.1.7	Limitations of the simulation and related comments	77
4.2	¹⁸ O results	79
4.2.1	Projectile energy-loss vs. total γ -ray energy	79
4.2.2	¹⁸ O strength distributions	83
4.2.3	Angular distributions	86
4.3	Extension to ²⁰ O	87
4.3.1	Initial interpretations	87
4.3.2	γ -decay branching estimates	88
4.3.3	²⁰ O strength distribution and results	92
5	Closing remarks	100
5.1	Experimental conclusions	100
5.2	Future virtual photon scattering studies with ²⁰ O at the NSCL	102
A	Reaction kinematics	105
A.1	Review of Lorentz transformations	106
A.2	Two-body collision dynamics	109
B	Intermediate-energy Coulomb excitation	114
B.1	The excitation cross section	114
B.2	Quantum mechanical corrections	119
B.3	Differential cross section functions	119
	<i>Bibliography</i>	123

List of Figures

1.1	Comparison of the total photoneutron excitation function for the stable oxygen isotopes, $^{16,17,18}\text{O}$	4
1.2	Summary of states in ^{18}O which could be populated.	9
1.3	Summary of states in ^{208}Pb which could contribute as background. . .	10
1.4	Known ^{20}O spectroscopic information along with theoretical predictions.	12
2.1	Schematic of the ^{20}O experimental setup.	14
2.2	Schematic of the S800 Spectrometer.	15
2.3	Schematic of the S800 focal plane.	16
2.4	Simplified diagram of the S800 electronics.	20
2.5	The front face of the forward BaF_2 array.	21
2.6	Perspective drawing of one BaF_2 detector.	22
2.7	Diagram of the ORNL trigger box, TB8000.	24
2.8	Simplified diagram of the electronics for the BaF_2 arrays.	25
3.1	Example of the first step in the ^{18}O identification process.	28
3.2	2-D histogram of RF_E1_TAC vs. E1_GEO_MEAN used for ^{18}O identification.	28
3.3	2-D histogram of E1_DOWN vs. E1_UP also used for ^{18}O identification.	29
3.4	2-D histogram of RF_E1_TAC vs. S801_CEN_FIT which illustrates the final step in the ^{20}O identification process.	30
3.5	Calibrated mask spectra from CRDC1 along with a template of the mask.	31
3.6	Mean $^{18,20}\text{O}$ raw parameter RF_E1_TAC vs. experimental run number.	32
3.7	Mean $^{18,20}\text{O}$ CRDC drift time parameter vs. experimental run number.	33
3.8	Uncorrected ^{20}O θ_t and ϕ_t distributions for runs 91–95.	34
3.9	Simplified picture to illustrate the effect of the beam blocker.	35
3.10	Comparison of ^{18}O dispersive angular distributions gated on projectile energy-loss.	36
3.11	Examples of raw ^{88}Y and PuBe calibration data for one BaF_2 detector.	37
3.12	Calibration fits for BaF_2 detectors 135 and 202.	38
3.13	Sample ^{88}Y and PuBe calibration spectra for detectors 135 and 202. .	38
3.14	^{18}O BaF_2 time spectra for selected detectors.	39
3.15	Comparison of the calculated T.O.F. _(RF-Array) parameter for ^{18}O against that for ^{20}O	41

3.16	Comparison of a fast vs. slow 2-D histogram generated for a particular BaF ₂ forward detector using data from the ¹⁸ O against the ²⁰ O equivalent.	42
3.17	A gate placed a 2-D plot of calibrated BaF ₂ energy vs. T.O.F. _(RF-Array) constrains a ¹⁸ O fast vs. slow histogram.	43
3.18	Cluster multiplicity as a function of incident γ -ray energy.	45
3.19	Sample PuBe calibration data showing the improvement of the array response when shower reconstruction is employed.	45
3.20	Representation which describes how the γ -ray emission angle was determined.	47
3.21	T.O.F. vs. energy for ¹⁸ O data showing the prompt γ -ray gate along with the shifted gate.	49
3.22	Shows the final event selection criterion for the ¹⁸ O and ²⁰ O studies.	50
3.23	Projection of events included within energy gates shown in Fig. 3.22 onto the Doppler-corrected axis for ¹⁸ O and ²⁰ O.	51
3.24	Doppler-corrected, experimental strength distributions for ¹⁸ O and ²⁰ O.	52
3.25	¹⁸ O and ²⁰ O angular distributions.	53
3.26	Comparison of Doppler-corrected strength distributions obtained after gating on specific ϕ_t regions for ¹⁸ O and ²⁰ O.	54
4.1	Schematic representation of the selection of a particular step in the decay sequence.	58
4.2	Sample input file for the ¹⁸ O simulation.	59
4.3	Comparison of Monte Carlo-generated ¹⁸ O angular distributions with the corresponding differential cross section functions generated using MATHEMATICA.	60
4.4	The geometrical setup of this experiment defined within GEANT.	65
4.5	GEANT particle tracks resulting from twenty ¹⁸ O excitations.	66
4.6	BaF ₂ resolution fit for a determination of the constants in Eq. 4.16.	66
4.7	Comparison of simulated against actual calibration data.	68
4.8	Doppler-corrected, ¹⁸ O BaF ₂ energy spectra for two extreme examples of calibration drifting.	69
4.9	The observed (θ_t, ϕ_t) acceptance “window” for ¹⁸ O.	70
4.10	Simplified illustration which defines the parameters in Eq. 4.18.	71
4.11	Elastically scattered beam (blocker out) energy distributions for ¹⁸ O and ²⁰ O projectiles as measured by the S800.	73
4.12	Sample data from the CRDC1 mask calibration which has been gated on the central region of CRDC2 to select straight-line trajectories.	75
4.13	Angular distributions for elastically scattered ¹⁸ O and ²⁰ O projectiles.	77
4.14	Projectile energy-loss vs. total, forward, reconstructed, Doppler-corrected γ -ray energy for ¹⁸ O.	79
4.15	Projectile energy-loss vs. forward, reconstructed, Doppler-corrected γ -ray energy for simulated ¹⁸ O data.	81
4.16	Projectile energy-loss for ¹⁸ O events in which the forward array recorded between 4.48 and 5.52 MeV.	82

4.17	Comparison of simulated ^{18}O strength distribution generated using known $B(E\lambda)$ and branching information with the experimental result.	84
4.18	Comparison of simulated ^{18}O strength distribution generated using slightly adjusted $B(E\lambda)$ and branching information with the experimental result.	85
4.19	Changes that were made to previously established ^{18}O experimental quantities in generating Fig. 4.18.	85
4.20	Final ^{18}O θ_t and ϕ_t experimental angular distributions shown against the results obtained from the improved simulation.	86
4.21	Comparison of the simulated ^{18}O strength function from Fig. 4.18 with that obtained after increasing the area of the acceptance “window” by a factor of two.	87
4.22	Projectile energy-loss vs. total, forward, reconstructed, Doppler-corrected γ -ray energy for ^{20}O	88
4.23	Projections of “decay gates” 1 and 2 from Fig. 4.22 onto the γ -ray energy axis.	90
4.24	Simulated ^{20}O strength distribution shown with experimental data.	92
4.25	Simulated projectile energy-loss vs. forward, reconstructed, Doppler-corrected γ -ray energy for ^{20}O	93
4.26	Improved ^{20}O simulated strength distribution shown with experimental data.	96
4.27	The simulated strength curves resulting from excitations to the two 1^- states.	98
4.28	The final ^{20}O θ_t and ϕ_t experimental angular distributions shown against the results obtained from the simulation.	99
5.1	^{20}O $E1$ strength prediction from Ref. 27.	102
5.2	Predictions for intensities of γ -rays between 8 and 20 MeV.	103
A.1	Scattering of two particles in the laboratory frame.	106
A.2	Scattering of two particles in the center-of-mass frame.	111
B.1	Coulomb excitation of the projectile as it scatters from the Coulomb field of the target.	115
B.2	Approximate and exact differential cross section functions, $df_{E\lambda}(\vartheta, \xi)/d\Omega$, for $E1$, $E2$, and $E3$ excitations, shown for different values of the adiabaticity parameter, ξ	121

List of Tables

1.1	The result of total Coulomb excitation cross section calculations for excitations to discrete 1^- , 2^+ and 3^- states in ^{18}O assuming an angular acceptance of 20 mrad.	9
1.2	The result of total Coulomb excitation cross section calculations for excitations to discrete 2^+ and 3^- states in ^{208}Pb assuming an angular acceptance of 20 mrad.	11
2.1	Relevant experimental quantities	14
3.1	The beam's dispersive and non-dispersive angular offsets.	34
4.1	Angular widths used to modify the incoming and outgoing projectile distributions in the simulation. All values are in mrad.	77
4.2	$E1$ branching from the first two excited 1^- states calculated from the predicted level scheme presented in Fig. 1.4.	90
4.3	The projectile and target level schemes utilized in the production of the simulated results presented in Fig. 4.24.	94
4.4	All ^{20}O branching used for the simulated results presented in Fig. 4.24.	94
4.5	The projectile and target level schemes utilized in the production of the improved ^{20}O simulated results presented in Fig. 4.26.	97
4.6	1^- branching used for the improved simulated results presented in Fig. 4.26.	97
5.1	^{20}O shell model predictions for 1^- levels	101
B.1	The factors by which the curves in Fig. B.2 should be multiplied	122

Chapter 1

Introduction

The structure of the atomic nucleus, which is made up of N neutrons and Z protons ($N + Z = A$ total nucleons) bound together by an attractive force known as the nuclear strong force, is, in general, extremely complex. Stable nuclear species, or those which are more readily found in nature, have been studied exhaustively. Over the last fifty years, useful theoretical tools have been developed which have described various observable aspects of these nuclear systems with a varying degree of success. The so-called *nuclear shell model*, which has stood out as the most successful of these tools, emerged out of an attempt to describe the observed “magic” numbers of nucleons $Z, N = 2, 8, 28, 50, 82, 126$ (as in ${}^4\text{He}$, ${}^{16}\text{O}$, etc.), which are linked to strong nuclear binding. Formally speaking, the shell model is a *microscopic* theory, in that it deals with the individual nucleons; a simplified description of the problem which the shell model attempts to solve is that of independent protons and neutrons moving within an average nuclear potential, or *mean field*, while simultaneously interacting with one another. Indeed, within this context, the mean field itself is a manifestation of the collection of nuclei, and is therefore a macroscopic feature.

As alluded to, the shell model, when applied to stable nuclear systems, is impressive in its ability to explain nuclear magicity and, for example, predict observable

features such as nuclear mass (nuclear binding) or energies and quantum numbers for excited levels. The natural progression of scientific technology in the realm of nuclear research facilities and their instrumentation has allowed for new experimental techniques, thereby opening the door for exciting studies of β and nucleon-unstable nuclei. In an effort to better understand the structure of these radioactive nuclei, e.g., to further challenge and extend the shell model and other working models of nuclear structure, modern nuclear science has undertaken the difficult task of the systematic investigation of short-lived species. One intriguing feature that has come to light in this new environment, for example, is new proton and neutron magicity, i.e., remarkable stability has appeared on the nuclear (Z,N) landscape in places where it was not predicted to exist from studies of the stable nuclei. (In this sense, modern nuclear science has witnessed the *break-down* of the traditional nuclear shell model.) Neutron or proton *halos* and *skins*, which are further examples of interesting features observed in unstable nuclei, are directly attributed to more extreme asymmetry in the neutron-to-proton ratio of the nucleus. Halos (typically 1 neutron or proton *loosely* bound to a stable core) result in large RMS nuclear radii and small binding energies, while skins (a small number of neutrons or protons bound to a stable core) are responsible for interesting collective effects such as the “Pigmy” resonance (e.g., Refs. 15 and 27). These and other phenomena have provided the impetus for ground-breaking experimental work which complements an increasingly complex nuclear theory, and vice versa.

1.1 Experimental motivation

Collective modes, which, in general, are excitations or resonances which can be described within the context of cooperative motion of the individual nucleons comprising the nucleus, are important probes of nuclear structure. The Isovector Giant Dipole

Resonance (IVGDR) is one such collective excitation which can be thought of as the motion of a neutron sphere or fluid against that of the protons. In heavy, spherical nuclei, the average excitation energy of this single-peaked resonance, E_{GDR} , varies rather smoothly with the number of nucleons, A . Specifically, $E_{\text{GDR}} \propto A^{-1/3}$, the constant of proportionality being approximately 79 MeV from a fit to experimental results. It should be mentioned that this $A^{-1/3}$ dependence is not an analytic result, but rather, can be derived from simple assumptions (see, e.g., Ref. 15). In lighter nuclei, $A \leq 50$, the GDR resonance energies are seen to deviate from this simple relation, favoring lower values. Additionally, the GDR excitation (or strength) function for lighter systems tends to display multiple peaks, which is a feature resulting from the growing importance of the individual nucleon (or single particle) sub-structure.

While the GDR has been studied extensively for stable nuclei, very little experimental information exists for unstable nuclear configurations. Recently there has been a great deal of theoretical speculation surrounding the question of how collective strength evolves as one progresses towards greater neutron excess. For example, the excitation function for the GDR mode is expected to fragment substantially, favoring, in particular, the onset of increasing strength at lower excitation energies (see Refs. 12, 14, 27 and references therein). The low-energy, or *soft*, portion of the strength distribution in neutron-rich nuclei is often ascribed to a so-called Pigmy resonance. Mentioned above, this excitation can be thought of as oscillation of the neutrons which comprise the neutron skin against the residual nuclear core.

Indeed, the evolution of the GDR in the stable oxygen isotopes sheds favorable light on the theoretical predictions. Shown in Fig. 1.1 is experimental (total) photon-neutron cross section data which has been collected (for example) by way of quasi-monochromatic annihilation photon scattering [17]. The experimental motivation for the current studies which will be described within this thesis came from the necessity to extend this picture further to ^{20}O . Photon-induced reactions using short-lived

nuclei (such as ^{20}O), however, require more sophisticated experimental strategies, as the system under study is not a target but instead is a relativistic projectile.

Two complementary methods for these types of experiments exist. Both methods rely on the virtual excitation of the projectile, i.e., Coulomb excitation, whereby the projectile is excited as it passes through the Coulomb field of a high- Z target. The so-called “virtual photon absorption” method takes advantage of particle decay modes following excitations to the projectile continuum, specifically, the (γ, xn) channels. This method has been proven viable, having been employed with a great deal of success, for example, by the LAND (Large Area Neutron Detector) collaboration at GSI. In fact, an experiment to measure the dipole strength function in the oxygen isotopes, specifically $^{18,20,22}\text{O}$, has been performed at GSI and the results have recently

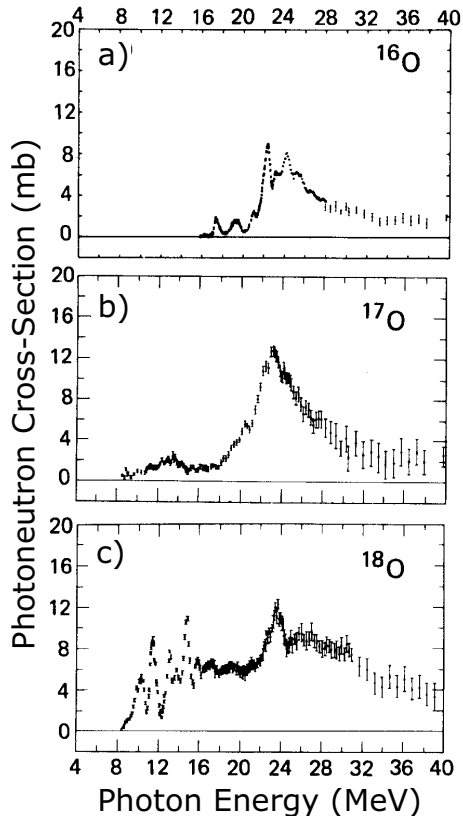


Figure 1.1: Comparison of the total photoneutron (GDR) excitation function for the stable oxygen isotopes, $^{16,17,18}\text{O}$, taken from Ref. 17. Low-lying strength emerges with the addition of neutrons to the doubly-magic core.

been published [5, 21]. The second method, known as “virtual photon scattering”, relies on real projectile γ -ray decay following virtual excitation [6, 24]. As compared with the absorption technique, this method suffers from a large suppression factor (between roughly 10^{-2} and 10^{-3}) related to the relatively low probability of the (γ, γ') decay channel. However, the scattering method is advantageous with regard to its dipole ($E1$) selectivity, since the absorption method is inclusive of contamination from other virtual photon multipolarities. Additionally, the scattering method has the ability to probe the strength function below the neutron separation energy (S_n), which is ideal.

Out of a need to establish the viability of this alternate method for GDR studies of radioactive systems, we chose to perform successive virtual photon scattering experiments with beams of ^{18}O and ^{20}O . The projectiles collided with a lead target, providing the virtual photon field. Given the fact that ^{18}O is stable and its strength function established (e.g., Fig 1.1c), this experiment was carried out first to serve as the control for the more difficult radioactive beam experiment which followed. Unfortunately, due to the small cross section for GDR virtual photon scattering events, essentially no γ -ray statistics were collected above S_n for either experiment. The experimental analysis, which will be the subject of all discussion to follow, was therefore dedicated to the discrete region of these nuclei. Specifically, the analysis sought to further establish the level structure of ^{20}O , as its discrete, 1^- , states had not been previously explored. Possessing this information, conclusions could then be drawn regarding discrete $E1$ strength in ^{20}O as compared with ^{18}O .

1.2 Coulomb excitation

Coulomb excitation, mentioned above, is a well-understood process which occurs during interactions of a projectile (Z_A) with a target (Z_B) whereby one of the participat-

ing nuclei is excited as it passes through the electromagnetic field of the other. The process can therefore be thought of as the absorption of a *virtual* photon by either the target or the projectile. Because, in pure Coulomb excitation, the participating nuclei stay outside the range of the nuclear strong force, the excitation cross section can be expressed in terms of the same multipole matrix elements that characterize excited-state γ -ray decay. Hence, Coulomb excitation amplitudes are strongly coupled with valuable nuclear structure information. This fact is illuminated when one examines an expression for the differential Coulomb cross section for the projectile which has been taken from state $|i\rangle$ to state $|f\rangle$ [1]:

$$\frac{d\sigma_{E\lambda}}{d\Omega} = \left(\frac{Z_B e}{\hbar v} \right)^2 a^{-2\lambda+2} B(E\lambda, I_i \rightarrow I_f) \frac{df_{E\lambda}(\vartheta, \xi)}{d\Omega}, \quad (1.1)$$

where, as given in Appendix B, a is half the distance of closest approach, ξ is the adiabaticity parameter, v is the incoming velocity of the projectile, and ϑ is the scattering angle of the projectile in the center-of-mass.

The important $B(E\lambda, I_i \rightarrow I_f)$ factor appearing in Eq. 1.1 is the reduced (electric) transition probability, which is proportional to the electric multipole matrix element. Specifically,

$$B(E\lambda, I_i \rightarrow I_f) = \frac{1}{2I_i + 1} |\langle I_f || \mathcal{M}(E\lambda) || I_i \rangle|^2. \quad (1.2)$$

This matrix element, which depends directly on the wave functions of the involved states, $|I_i\rangle$ and $|I_f\rangle$, is a measure of collectivity in the nuclear transition and is therefore linked to structural features such as nuclear rotation or vibration. Indeed, transitions which couple states $|I_i\rangle$ and $|I_f\rangle$ that are comprised mostly of single particle motion (which cannot give rise to collective phenomenon) will be marked by small matrix elements, $\langle I_f || \mathcal{M}(\pi\lambda) || I_i \rangle$. Therefore, Coulomb excitation tends to probe collective configurations in nuclei.

The derivation of Eq. 1.1 involves a semi-classical approach. The trajectory of the projectile is treated classically, assuming a Rutherford scattering distribution, while the interaction which causes the nuclear transition in the projectile or target is found using first-order perturbation theory, i.e.,

$$\frac{d\sigma}{d\Omega} = \left(\frac{d\sigma}{d\Omega} \right)_{\text{Ruth.}} P_{i \rightarrow f} , \quad (1.3)$$

where the probability, $P_{i \rightarrow f}$, is given by the square of amplitude of the nuclear excitation process:

$$P_{i \rightarrow f} = |a_{i \rightarrow f}|^2 ; \quad a_{i \rightarrow f} = \frac{1}{i\hbar} \int_{-\infty}^{\infty} \langle f | V(\mathbf{r}(t)) | i \rangle e^{i(E_f - E_i)t/\hbar} dt . \quad (1.4)$$

Since a more-detailed description of the cross section derivation can be found in Appendix B, it is sufficient for the current discussion to present the final expressions. For the experimental analysis it was necessary to include only electric contributions to the virtual excitation spectrum, namely from $E1$, $E2$, and $E3$ (justification is provided below in Sec. 1.3.) Substitution of the differential cross section functions, $df_{E\lambda}/d\Omega$, for these specific cases (given by Eq. B.20) into Eq. 1.1 allows the following:

$$\begin{aligned} \frac{d\sigma_{E1}(\vartheta, \xi)}{d\Omega} &= \left(\frac{\pi}{18} \right) \left(\frac{Z_B \alpha}{\beta} \right)^2 \frac{B(E1, I_i \rightarrow I_f)}{\sin^4(\frac{\vartheta}{2})} [I_{1-1}^2(\vartheta, \xi) + I_{11}^2(\vartheta, \xi)] \\ \frac{d\sigma_{E2}(\vartheta, \xi)}{d\Omega} &= \left(\frac{\pi}{25} \right) \left(\frac{Z_B \alpha}{\beta} \right)^2 \frac{B(E2, I_i \rightarrow I_f)}{a^2 \sin^4(\frac{\vartheta}{2})} \times \\ &\quad \left[\left(\frac{3}{8} \right) \{I_{2-2}^2(\vartheta, \xi) + I_{22}^2(\vartheta, \xi)\} + \left(\frac{1}{4} \right) I_{20}^2(\vartheta, \xi) \right] \\ \frac{d\sigma_{E3}(\vartheta, \xi)}{d\Omega} &= \left(\frac{\pi}{49} \right) \left(\frac{Z_B \alpha}{\beta} \right)^2 \frac{B(E3, I_i \rightarrow I_f)}{a^4 \sin^4(\frac{\vartheta}{2})} \times \\ &\quad \left[\left(\frac{5}{16} \right) \{I_{3-3}^2(\vartheta, \xi) + I_{33}^2(\vartheta, \xi)\} + \left(\frac{3}{16} \right) \{I_{3-1}^2(\vartheta, \xi) + I_{31}^2(\vartheta, \xi)\} \right] , \end{aligned} \quad (1.5)$$

where β is the incoming velocity of the projectile and the substitution $e^2/\hbar c \rightarrow \alpha$ has been utilized. It is assumed that the reduced transition probability is expressed in units of $e^2 \cdot \text{fm}^{2\lambda}$.

The $I_{\lambda\mu}(\vartheta, \xi)$ functions in Eq. 1.5 are defined in Ref. 1 as the Coulomb excitation functions and are given by Eq. B.11 in complicated integral form. However, the fact that the projectiles detected in this study were limited to small forward angles ensures that the approximate expression for the $I_{\lambda\mu}(\vartheta, \xi)$ functions, Eq. B.13, is valid (see Fig. B.2). It should be mentioned that Eq. 1.5 has been derived assuming projectile excitation. To convert these expressions to relations which are valid for excitation of the target, one need only exchange Z_B for Z_A .

1.3 Accessible states in ^{18}O

Given the relatively small probability for $M1$ virtual photons, and the fact that no (unnatural parity) 1^+ states exist in the region below the neutron binding energy [35], it was sufficient to restrict the analysis to electric excitations. The existence of states with spin and parity of 1^- , 2^+ and 3^- , in principle, allows for excitations with $\lambda = 1 \rightarrow 3$. Shown in Fig. 1.2 is the low-lying level structure of ^{18}O which is relevant to the current study. The $B(E\lambda)$ strengths given in Fig. 1.2a are known experimental values [31, 35]. (The upper limit for the 1_1^- state comes from an electron scattering study [22].) The complicated radiative decay scheme for these excited configurations, included as Fig. 1.2b, demonstrates that excitations to only a few levels will, in general, produce rather convoluted results.

To gain some perspective regarding the relative importance of these excitation channels for the ^{18}O study, note the total cross section values in Table 1.1 that have been calculated (using the formalism introduced in Sec. 1.2) assuming an overall projectile angular acceptance of 20 mrad in the center-of-mass. Based on these $B(E\lambda)$

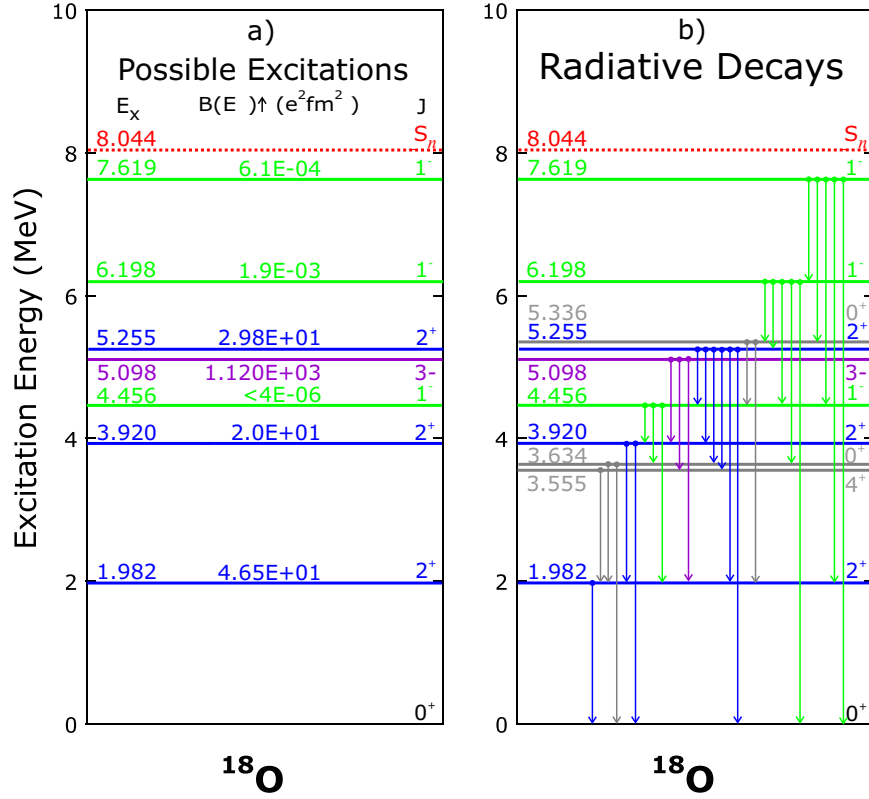


Figure 1.2: Summary of states in ^{18}O which were accessible. a) Experimentally determined $B(E\lambda)$ information for excitations from the ground state [22,31,35]. b) Possible radiative decays resulting from the excitations in (a). *Images in this dissertation are presented in color.*

Table 1.1: The result of total Coulomb excitation cross section calculations for excitations to discrete 1^- , 2^+ and 3^- states in ^{18}O assuming an angular acceptance of 20 mrad.

Coulomb excitation predictions for ^{18}O			
J_n^π	Energy (MeV)	$B(E\lambda)$ ($e^2\text{fm}^{2\lambda}$)	σ (μb)
1_1^-	4.456	<4E-06	<3E-01
1_2^-	6.198	1.9E-03	4.1E+01
1_3^-	7.619	6.1E-04	5.2E+00
2_1^+	1.982	4.65E+01	2.35E+03
2_2^+	3.920	2.0E+01	6.9E+02
2_3^+	5.255	2.98E+01	6.76E+02
3_1^-	5.098	1.120E+03	9.860E+00

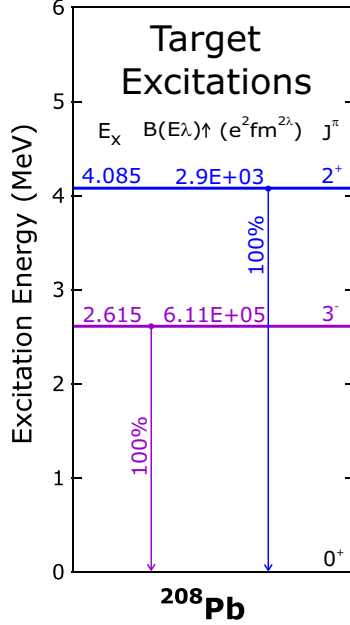


Figure 1.3: Summary of states in ^{208}Pb which could contribute as background. Known $B(E\lambda)$ values are given for excitations from the ground state [23,26]. Both states decay directly back to the ground state configuration.

values, the calculations predict that quadrupole ($E2$) excitations will completely dominate over dipole ($E1$) and octupole ($E3$) excitations. The largest, non- $E2$, contribution comes from the second-excited 1^- state.

1.4 ^{208}Pb contributions

Background resulting from excitations in the target was a significant experimental obstacle. Fig. 1.3 shows the pertinent ^{208}Pb level scheme, which includes 2 states, namely the first-excited 3^- and 2^+ configurations. Included in this figure are known values for the reduced transition probability for excitations of these states [23,26]. A prediction for the relative importance of target contributions follows from comparisons of Coulomb cross section calculations for ^{208}Pb , shown in Table 1.2, with the results obtained for the projectile, ^{18}O (Table 1.1). For example, from these calculations, one would expect that the target should account for $\sim 20\%$ of the total $E2$ cross section

Table 1.2: The result of total Coulomb excitation cross section calculations for excitations to discrete 2^+ and 3^- states in ^{208}Pb assuming an angular acceptance of 20 mrad.

Coulomb excitation predictions for ^{208}Pb			
J_n^π	Energy (MeV)	$B(E\lambda)$ ($e^2 \text{fm}^{2\lambda}$)	σ (μb)
2_1^+	4.085	2.9E+03	9.1E+02
3_1^-	2.615	6.11E+05	5.30E+01

in the ^{18}O experiment.

1.5 Status of ^{20}O spectroscopy and shell model predictions

From the Coulomb excitation cross section calculations for ^{18}O presented above in Sec. 1.3, along with $^{18,20}\text{O}$ systematics, it is reasonable to assume that an analysis which includes $E1$, $E2$, and $E3$ virtual excitations is also required for the ^{20}O study. The fact that limited ^{20}O experimental spectroscopic information exists, however, demands that we look to theoretical predictions for guidance. The left panel of Fig. 1.4 summarizes the pertinent status of ^{20}O spectroscopy [26, 34]. Aside from our knowledge of the $B(E2)$ for the 2_1^+ and the branching from the 2_2^+ , only the energies and spin-parity of observed ^{20}O levels have been established. Notice, especially, that apart from the tentative 3^- assignment of the 5.614 MeV state, no experimental information regarding the ^{20}O negative-parity, discrete structure exists. Meanwhile, the theoretical picture for ^{20}O , illustrated by the right panel of Fig. 1.4, is interesting. Comparing the $B(E2) \uparrow$ predictions from B.A. Brown [9] with measured $B(E2) \uparrow$ values for the analogous excited 2^+ configurations in ^{18}O (see Fig. 1.2a) we see a marked suppression of $E2$ strength. Contrasting this is the trend which unfolds from a comparison of the ^{20}O $B(E1) \uparrow$ predictions with the measured ^{18}O values for the first three 1^- states. As mentioned in Sec. 1.1, a relative increase in low-lying dipole strength in

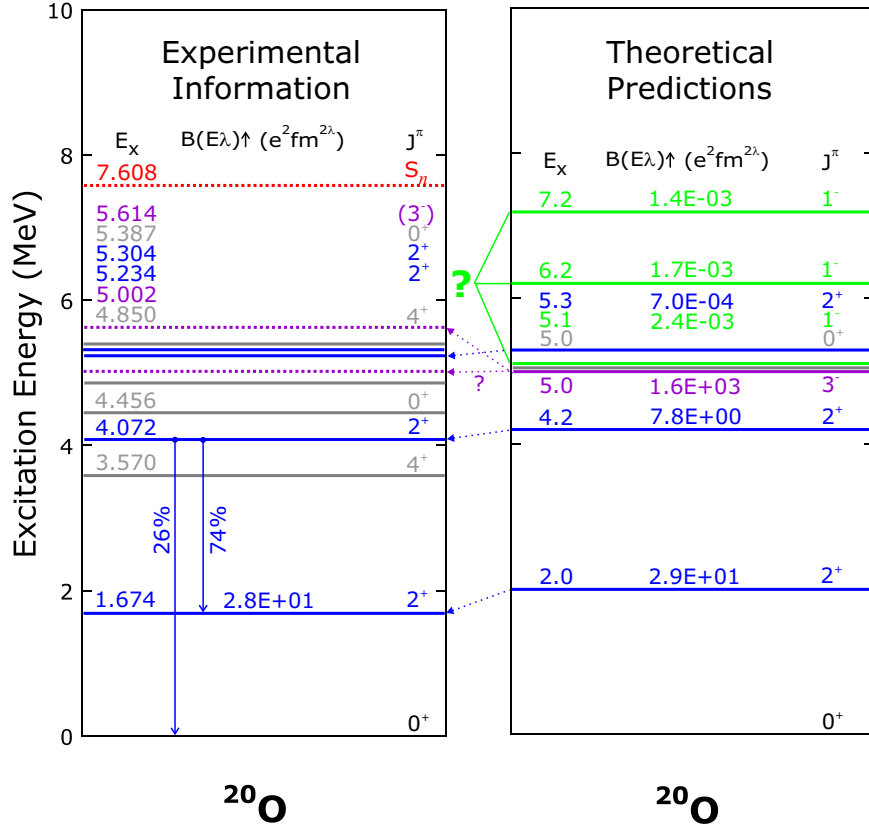


Figure 1.4: Known ^{20}O spectroscopic information [26, 34](left) along with sd shell model predictions from B.A. Brown [9] (right). Included on the left are all states below the neutron separation energy which have determined spin and parity (with the exception of a 5^- state at 7.252 MeV). Only the $B(E2)\uparrow$ value for the 2_1^+ has been measured, and decay-branching is known only for the 2_2^+ . The predicted 1^- states have not yet been observed experimentally.

neutron-heavier ^{20}O is expected. While the cross section calculations in Sec. 1.3 show that 1^- states are not expected to be strongly-excited in the ^{18}O experiment, theory clearly predicts that this will not be the case with ^{20}O .

Chapter 2

Experimental details

In October of 1998, two successive experiments with the goal of investigating virtual photon scattering in ^{18}O and ^{20}O were performed at the National Superconducting Cyclotron Laboratory (NSCL). For the first experiment, ^{18}O , having been accelerated in the K1200 superconducting cyclotron to an energy of 100 MeV/u, was delivered directly to our experimental hall. The second study required a radioactive beam. ^{22}Ne primary was accelerated in the K1200 to an energy of 120 MeV/u. This beam impinged on a thick ^9Be production target. Fragments produced via projectile fragmentation were then analyzed with the A1200 Fragment Separator [29]. Using a combination of two magnetic bends along with a wedge degrader and momentum slits, this device selected ^{20}O at 100 MeV/u with a momentum spread ($\Delta p/p$) of 0.5%.

After being produced and transported to the S800 experimental hall, the $^{18,20}\text{O}$ beams were guided through the S800 analysis line (described in Sec. 2.1) to a target pot, where they impinged on a 30 mg/cm^2 ^{208}Pb (99.09% enrichment) reaction target. Reaction products were then analyzed using the S800 spectrograph. Being primary beam, the intensity of the ^{18}O beam was constrained by the capabilities of the S800 focal plane detectors, which can count up to $\sim 10^4$ frag./second. The ^{20}O intensity, limited by production, was $\sim 5 \times 10^5$ particles/second. Table 2.1 summarizes some

Table 2.1: Relevant experimental quantities

Beam	Energy (MeV/u)	Intensity (part./sec.)	Impurity	Run Time (hrs.)
^{18}O	100	limited by S800	–	13
^{20}O	100	$\sim 5 \times 10^5$	$< 20\%$ ^{17}N	117

relevant experimental quantities.

The set-up specific to the ^{20}O experiment is represented in Fig. 2.1. Two BaF_2 arrays were used to measure γ -ray decays which came in coincidence with the detected reaction fragments. It was anticipated that projectile-correlated BaF_2 timing would be critical for γ -ray selection in the BaF_2 arrays. Because an inherent momentum spread in the secondary beam necessarily results in the spreading of the prompt- γ -ray BaF_2 time peak, two Multi-Channel Plate (MCP) detectors, designed and built at ORNL, were included into the ^{20}O set-up to improve BaF_2 timing. For the primary beam study with ^{18}O , timing was not of concern. Therefore, the MCP detectors were employed only for the ^{20}O experiment. (Incidentally, The MCP detectors additionally allowed for a determination of the ^{20}O beam intensity.)

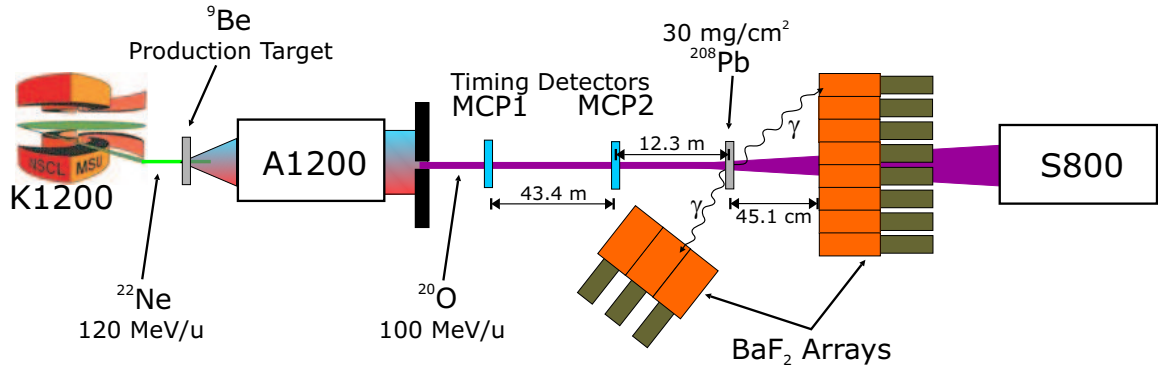


Figure 2.1: A schematic (not to scale) of the ^{20}O experimental setup. The Multichannel Plate (MCP) timing detectors, developed by ORNL, were used to improve BaF_2 timing.

2.1 The S800 spectrometer

As has been mentioned, projectiles and reaction fragments were analyzed using the S800 spectrometer, operated at 0° . As shown in Fig. 2.2, the S800 spectrometer [10] consists of a fragment analysis line and a large magnetic spectrograph. The analysis line itself is comprised of four bending dipoles, one quadrupole doublet, five quadrupole triplets and four sextupoles. The standard S800 target chamber is located at the dispersive image of the analysis line. For the present study it was necessary to remove the target chamber in order that there be sufficient space for the large BaF_2 array. Thus, the ^{208}Pb target was repositioned 85 cm upstream from the usual target position.

The magnetic spectrograph bends nuclear species of appropriate rigidity to its focal plane (enlarged in Fig. 2.3). Two dipole magnets, D1 and D2, each with a bending radius of 2.8 m and maximum central field of 1.6 T, provide an overall bending power of 4 Tm. Quadrupoles Q1 and Q2, located immediately downstream from the target chamber, focus fragments in the dispersive (x) and non-dispersive (y)

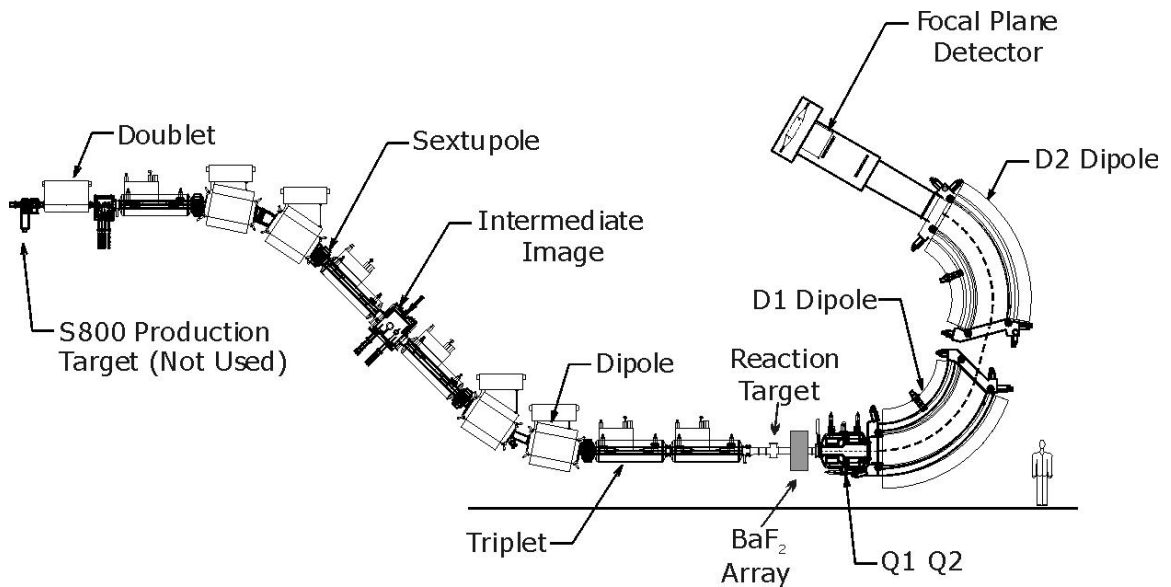


Figure 2.2: Schematic of the S800 Spectrometer. It consists of an analysis line and a large, 4 Tm magnetic spectrograph.

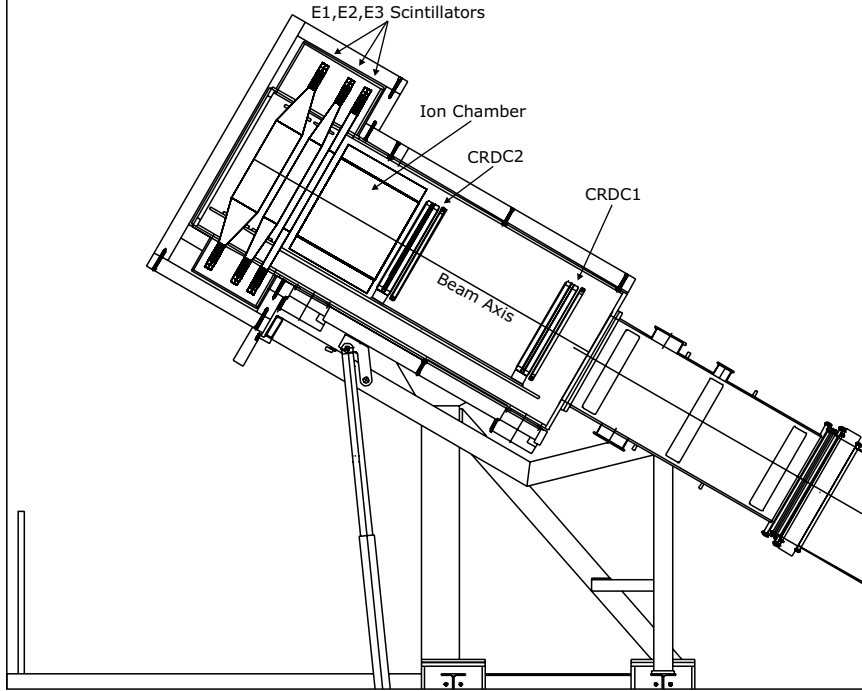


Figure 2.3: Schematic of the S800 focal plane. Fragments are focused onto CRDC1, the first of two position-sensitive detectors. The CRDC detectors, together, provide fragment trajectory information, while the IC, E1, E2 and E3 provide ΔE , E and timing.

directions thereby optimizing the angular acceptance of the device.

Operated with the target at its designed location, the S800 has an angular acceptance of 7° and 10° in the dispersive and non-dispersive directions, respectively [37]. With the target repositioned, from simple geometric arguments, approximately half of this acceptance is lost. The design of the position-sensitive elements of the focal plane detector (to be discussed in Sec. 2.1.1) allows for an angular resolution of 2 mrad. The energy resolution of the device is improved by operating in dispersion-matched, energy-loss mode. Running in this mode, the device compensates for intrinsic beam momentum spreading in the dispersive direction, which ideally results in a zero-width image at the focal plane. For every ~ 10 cm at the dispersive image (reaction target), the S800 is capable of correcting for 1% in $\Delta p/p$.

2.1.1 Position-sensitive CRDC detectors

Two cathode readout drift chamber detectors (CRDC1 and CRDC2) are the position sensitive elements of the S800 focal plane. Each CRDC detector has an active area of $30\text{ cm} \times 59\text{ cm}$ and is filled with a mixture of 80% CF_4 and 20% C_4H_{10} gases to a pressure of 140 Torr.

Charged particles traveling through the detector ionize molecules in the gas. Electrons produced during this process then drift through a region of constant electric field until they reach a grounded Frisch grid. Passing through this grid, the electrons are accelerated towards an anode wire. The radial geometry of the electric field in this region is such that charge amplification, which results from an electron avalanche, takes place near the anode. 224 cathode *pads*, staggered on either side of the anode wire with a spacing of 2.54 mm (over the 59 cm dispersive dimension of the detector) measure induced charges from electron showers collected at the anode. Because no avalanching occurs in the region of constant electric field, the Frisch grid insures that the integration over all pad signals will be independent of the charged fragment's interaction distance from the anode.

A Gaussian fit over non-zero pad signals determines the incident fragment's dispersive (x) position within the detector. The incident fragment's non-dispersive (y) position within the detector is found by measuring the drift time of the electrons from the point of interaction to the anode. Typical drift times of electrons in the CRDC detectors are $\leq 20\ \mu\text{s}$, which directly limits the counting rate to $\sim 10^4$ frag./second. Achievable position resolution in these detectors is designed to be better than 0.48 mm in either direction.

Information collected from the CRDC detectors completely determines the trajectory of fragments reaching the focal plane, parameterized as $(x_f, \theta_f, y_f, \phi_f)$. θ_f and ϕ_f are angles of the trajectory taken in the x - z and y - z planes, respectively, while the subscripts, f , denote that these quantities are measured at the focus. Because

the magnetic fields present within the spectrograph have been mapped (this process is described in detail in Ref. 10), it is possible to reconstruct, analytically, the trajectory of fragments of known magnetic rigidity through the S800. In practice, from knowledge of $(x_f, \theta_f, y_f, \phi_f)$ one is able to calculate (approximately) quantities which describe the motion of the fragments as they left the target $(\theta_t, y_t, \phi_t, \delta_t)$, where δ_t is related to the fragment's kinetic energy. Specifically, $\delta_t = (E - E_c)/E_c$, where E_c is the kinetic energy of projectiles traveling along the central axis of the spectrometer, determined by

$$B\rho_{\text{S800}} = \frac{p_c}{q} = \frac{\sqrt{2mE_c}}{q}. \quad (2.1)$$

Here $B\rho_{\text{S800}}$ is the magnetic rigidity setting of the device and m and q are the mass and charge, respectively, of the fragment.

The matrix equation which relates the target quantities to those at the focus is

$$\begin{pmatrix} \theta_t \\ y_t \\ \phi_t \\ \delta_t \end{pmatrix} = \mathbf{R} \begin{pmatrix} x_f \\ \theta_f \\ y_f \\ \phi_f \end{pmatrix}, \quad (2.2)$$

where \mathbf{R} , known as the inverse matrix, is calculated by the code COSY INFINITY [7], which analytically inverts the direct expression, given by

$$\begin{pmatrix} x_f \\ \theta_f \\ y_f \\ \phi_f \end{pmatrix} = \mathbf{S} \begin{pmatrix} \theta_t \\ y_t \\ \phi_t \\ \delta_t \end{pmatrix}. \quad (2.3)$$

For Eqs. 2.2 and 2.3 the dispersive object beam spot-size at the target (which is not

the same as the beam spot-size due to intrinsic momentum dispersion) is assumed negligible.

2.1.2 Ionization chamber and scintillation detectors

After passing through the CRDC detectors, fragments enter the S800 Ionization Chamber (IC). The IC is filled with P10 gas (90% argon and 10% methane) to a pressure of 300 Torr. As with the CRDC detectors, molecules of the gas are ionized by the charged fragments. Segmented into 16 individual chambers, each with a 1 in. anode oriented perpendicular to the fragment's path, the IC chamber samples a fragment's energy-loss multiple times, thus reducing noise and providing an accurate energy-loss (ΔE) signal.

Fragments are then stopped in a series of three large plastic scintillator detectors, E1, E2, and E3, which, in the standard arrangement, are 5, 10 and 20 cm thick, respectively. (The charged particles of interest for this study did not penetrate beyond E2.) Photons produced by charged-particle interactions within these scintillators travel to either end of the detector where they are collected and converted into an electronic signal by photomultiplier (PMT) tubes (2 per detector). The signals produced in these detectors provide timing as well as ΔE and total energy information. Thus E1, E2, and E3 information, combined with the signal from the IC, allow standard ΔE vs. E and time-of-flight (T.O.F.) vs. E fragment identification techniques to be employed.

2.1.3 S800 electronics

Diagrammed in Fig. 2.4 are the S800 electronics which were used for the present study. Data readout in the S800 was triggered by a simultaneous signal in both the PMTs which sense light output from the E1 scintillator. Specifically, the S800 master gate was created by the logical AND of constant fraction discriminator (CFD) signals from both E1 scintillator PMTs. This master gate was then directed to the trigger

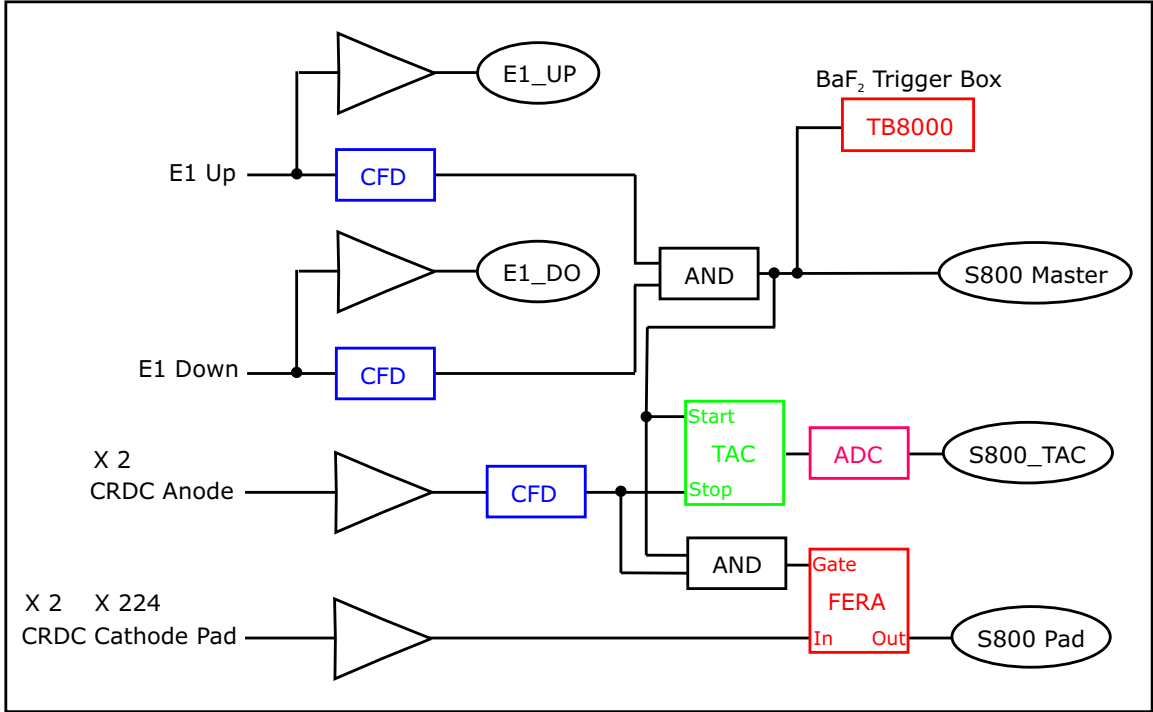


Figure 2.4: Diagram of the S800 electronics. For simplification, only one anode channel and one CRDC pad channel is shown. The triangular symbols represent shaping and/or amplification of the signal. (Adapted from Ref. 10.)

box of the BaF₂ array, which controlled the computer acquisition for this experiment. (BaF₂ electronics will be discussed in detail in Sec. 2.2.3.) The S800 master gate was also piped as the START input to each CRDC time-to-analog converter (TAC), the stop coming from the individual CRDC anodes. Additionally, the S800 master gate was the start for a TAC which measured time relative to the cyclotron RF. The analog signal coming from these TACs was then integrated and digitized by a 12-bit analog-to-digital converter (ADC), thus creating the electron drift-time and S800 T.O.F. parameters. Finally, the master gate, AND-ed with the CRDC anode, became the start for the fast encoding and readout ADCs (FERAs), which integrated the charge collected from the individual, amplified CRDC pad channels.

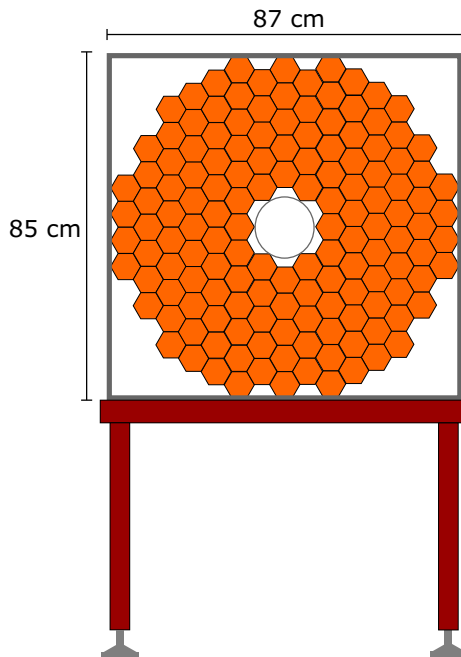


Figure 2.5: The front face of the forward array which consisted of 144 individual hexagonal crystals. The center of the array was placed directly on the beam axis.

2.2 The ORNL-TAMU-MSU BaF₂ Array

γ -rays coming from both projectile and target de-excitations were captured and analyzed using two arrays of BaF₂ detectors. The larger, forward array was placed 45 cm downstream from the target, covering angles between 11° and 48° in the laboratory frame. The forward array consisted of 144 individual hexagonal detectors, packed tightly in hexagonal geometry around the beam pipe, as shown in Fig. 2.5. From the center of the array moving outward, the detectors were positioned systematically closer to the target (in steps of 1 cm). This packing design allowed for an improvement in total solid angle coverage. Those detectors owned by Oak Ridge National Laboratory (ORNL) and Texas A&M University (TAMU), which together represent a large fraction of the forward array's detectors, are essentially identical, having crystals with inscribed diameters of 6.5 cm and lengths of 19.5 cm. The Michigan State University (MSU) crystals, however, have inscribed diameters of only 6 cm and lengths of 24.5 cm. Thus, the placement of the MSU detectors within the array was strategic so

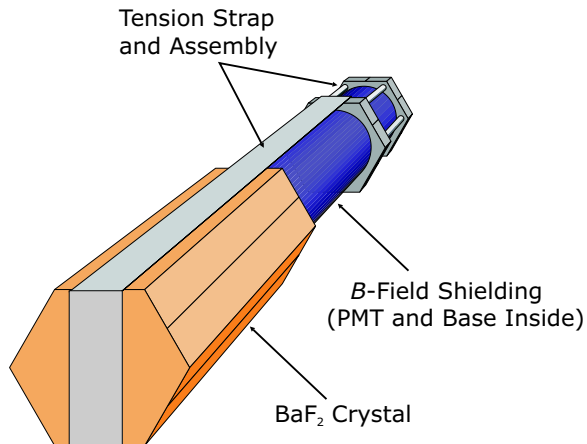


Figure 2.6: Perspective drawing of one BaF_2 detector. The crystal is coupled to the PMT using an optical grease. A tension strap adds stability to the detector.

as not to destroy the tight symmetry (e.g. they were placed mostly at the top of the array).

A smaller, 7-element (backward) BaF_2 array was placed behind the target, $\sim 28^\circ$ off the beam axis, to monitor target contributions within the forward array. The hexagonal crystals which comprised this array were larger – 8.7 cm inscribed diameter and 20 cm in length.

2.2.1 Detector construction

Fig. 2.6 is a representation of an individual BaF_2 detector. The crystal is coupled to the quartz window of the PMT with VISC-600M (General Electric Corp.) optical grease. This grease is chosen because it is transparent to the deep UV (fast) component of light produced by interactions within the crystal lattice [18,28]. (Properties of BaF_2 crystals will be discussed in Sec. 2.2.2.) In order to insure maximum light collection, the crystals are wrapped in Teflon tape, which has good reflective properties, and aluminum foil. The coupled crystal and base are then tightly wrapped in electrical tape to mask all ambient light. A magnetic shielding is placed over the PMT and its base. Stability is added to the coupling joint by tightening a tension strap which is

anchored at the end of the shielding. The hexagonal aluminum rings of the tension assembly, machined to the same dimensions as the crystal, support the weight of the PMT and shield when the detector is lying on its side as in a typical experiment.

2.2.2 BaF₂ properties

Inorganic scintillators emit UV light when fast electrons, resulting from interactions with γ -rays, neutrons, α particles, or other heavy species, displace electrons from the crystal lattice. BaF₂ is one type of inorganic scintillator which has relatively good efficiency and excellent timing properties. Its timing capabilities are directly attributed to the emission of a fast UV (210 nm) burst of light which has a characteristic decay time of 0.6 ns [20]. This fast light is emitted when electrons are displaced from the outer core band of the ionic crystal and a valence electron drops to fill the vacancy [19]. A slow component of light with a longer, 620 ns characteristic decay time is also emitted at slightly longer wavelengths (320 nm). This is the component of the emission which is a result of de-excitations in excited activator atoms. (Free electrons are captured to excited activator orbitals.)

Because of its light emission properties, BaF₂ is also capable of pulse-shape discrimination (PSD). PSD is based on the principle that different particles interact differently within the crystal. PSD between γ -rays, and neutrons (or charged-particles) is achieved with BaF₂ by comparing the amount of fast to slow light emitted by the detector during an event. (Examples of PSD will follow in Sec. 3.2.2.)

2.2.3 BaF₂ electronics

The BaF₂ array used for this study is a relatively mobile device, and as such, its basic operational principle from experiment to experiment changes very little. As depicted in Fig. 2.7, the array's trigger box, TB8000, controlled the type of events which were recorded at run time. Two standard BaF₂ trigger levels exist, hi- γ and

Input Trigger Examples

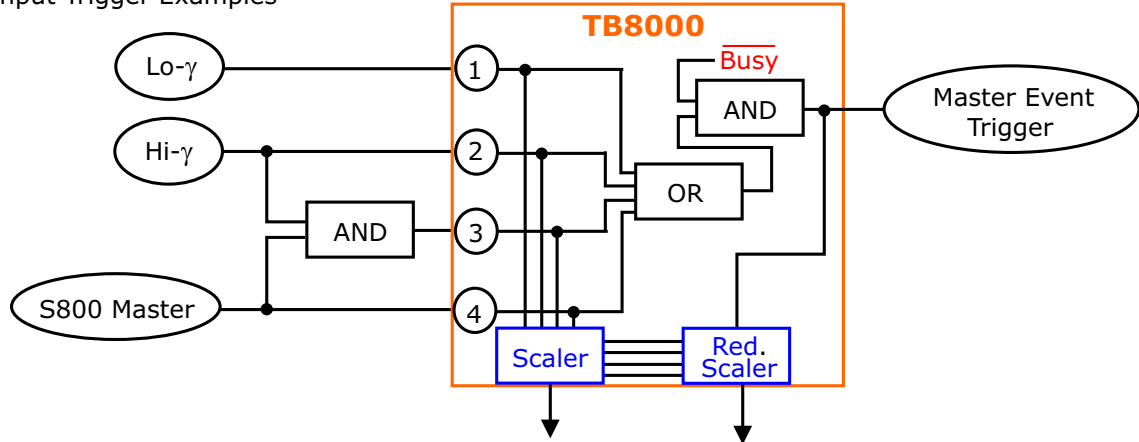


Figure 2.7: Diagram of the ORNL trigger box, TB8000, which controlled the computer acquisition for these experiments. The trigger box accepts multiple trigger inputs, provides down-scaling, and also checks for a system inhibit. (Adapted from Ref. 28)

lo- γ . Hi- γ is true when one element of the array records a signal above T_h , the high threshold setting (between approximately 2 and 4 MeV). It follows that lo- γ is true if one detector fires above T_l , the low threshold setting (below 1 MeV). In either case, only the signals from those detectors which fire above T_l are charge-integrated.

The hi- γ and lo- γ logic signals are fed to TB8000, as well as any logic signals which are specific to the experimenter’s setup – in this case the S800 master gate. For the present study, two other trigger levels were important, namely S800 singles and S800+hi- γ coincidences. In general the lo- γ trigger was used for taking calibration data, while S800 singles and S800+hi- γ coincidences were used to investigate the physics of interest. A trigger is accepted into the data stream with the flip of a toggle switch on the trigger box, which makes for smooth transitions between different types of runs. TB8000 has the capability to reject any input triggers due to a system inhibit (acquisition busy). Optionally, the inputs to TB8000 can be down-scaled. Comparison of the scaler output to the reduced scaler output allowed for a determination of system dead-time.

Because of the type of electronics which were used to readout BaF₂ events, the array was logically subdivided into 16-channel banks. One channel in each bank was

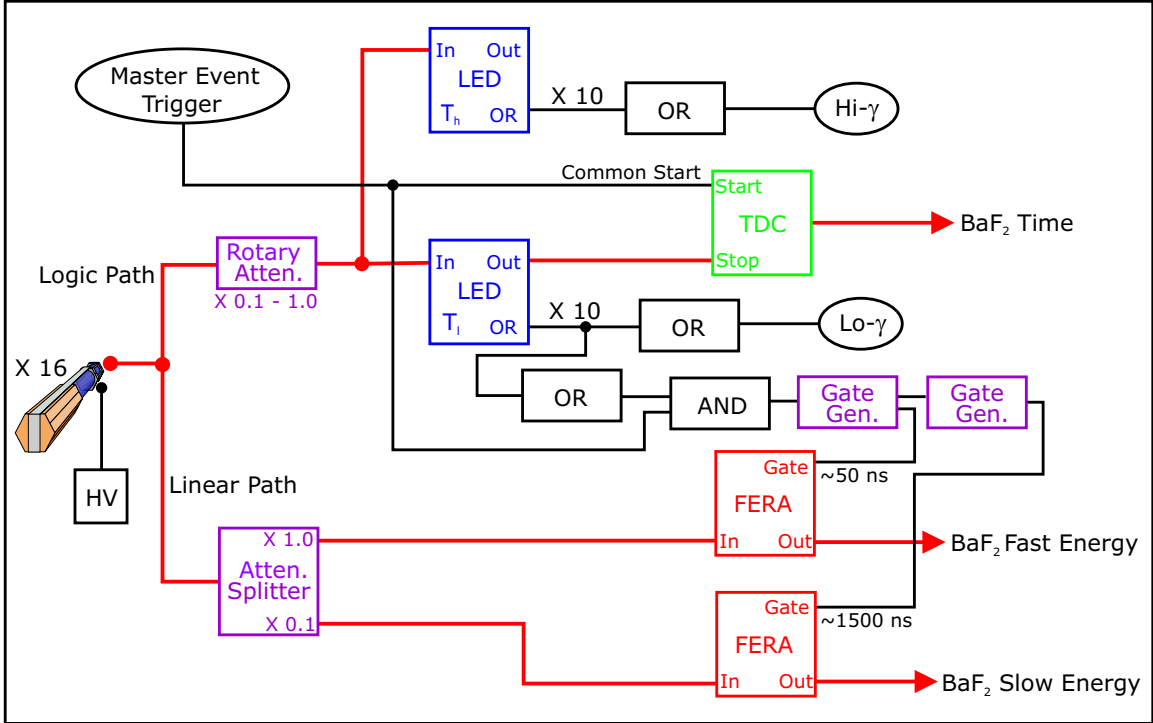


Figure 2.8: Simplified diagram of the electronics for the BaF₂ arrays. The detectors were subdivided into “banks” of 16 for a total of 10 banks. (Adapted from Ref. 28)

reserved as a spare. In all, 10 banks of electronics were therefore required. Fig. 2.8 is a simplified schematic of the electronics set-up for the array.

The signals coming from each detector followed two paths. Tracing the logic path, the individual signals were first attenuated to insure that the T_l and T_h thresholds applied using the leading-edge discriminators (LEDs) were consistent in energy. This was necessary because the LEDs are sensitive to the fast light, while, in general, the ratio of fast to slow light emitted for a given detector is highly dependent on the quality of its crystal-to-PMT coupling. Following attenuation, the NIM signals for each bank were split and converted to 16-channel ribbon cable with a NIM-ECL converter. The ribbon cables carrying the attenuated signals for each bank became inputs for the LEDs. The OR output of the T_h LED from each bank, OR-ed, provided the hi- γ trigger. In addition to providing the lo- γ trigger, the OR output of the T_l LED from each bank, OR-ed, was used to generate the fast (~ 50 ns) and slow

(~ 1500 ns) FERA gates. The individual T_i LED signals, meanwhile, provided the individual FASTBUS TDC stops.

The linear path was less complicated. The NIM signals for each bank were sent to a splitter/attenuator/delay box which was designed and built at ORNL. This module splits the signals, the outputs being 16-channel ribbon cable format. One ribbon cable provided the input for the fast FERA, while the other was sent to the slow FERA.

Chapter 3

Experimental data analysis

The experimental data analysis for both experiments was performed in a consistent fashion. Fragments produced via interactions of the beam projectiles with the ^{208}Pb target were swept to the focal plane of the S800 Spectrometer, where identification could take place. Except when used to monitor the S800 set-up, elastically scattered beam fragments were not of interest to this study. To eliminate these background events from the data stream, a beam blocker was strategically placed in front of CRDC1. After selecting only those S800+ γ coincident events where a beam projectile was detected at the focus, the projectile's measured energy loss was compared with the total decay γ -ray energy captured in the BaF₂ array.

3.1 Projectile analysis with the S800

3.1.1 ^{18}O and ^{20}O identification

As mentioned, being able to select those events where a beam projectile scattered inelastically from the target was the first step in the analysis of these experiments. In order to achieve this, the ΔE , E and T.O.F. information gathered at the focal plane was utilized. Specifically, particle identification (PID) for the ^{18}O experiment

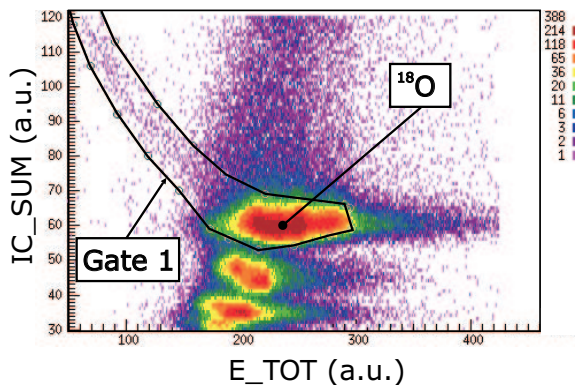


Figure 3.1: The first step in the ^{18}O identification process. A gate is placed on a 2-D histogram of IC_SUM vs. E_TOT.

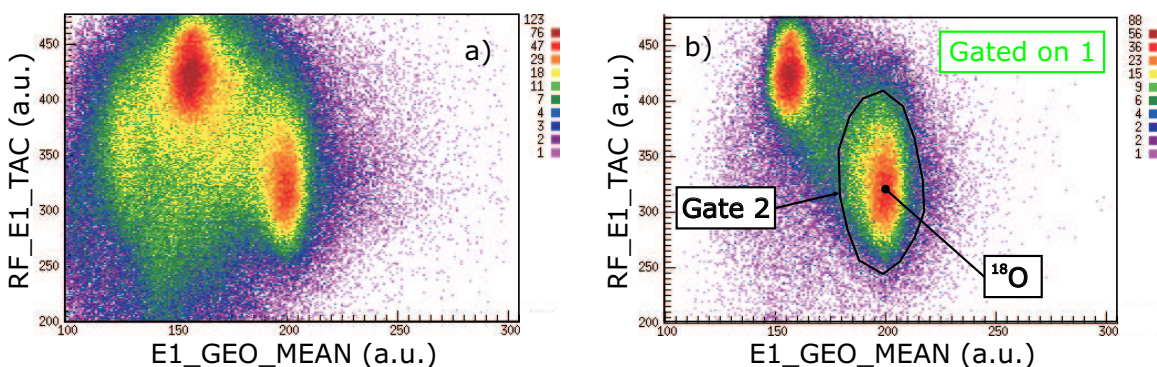


Figure 3.2: 2-D histogram of RF_E1_TAC vs. E1_GEO_MEAN before (a) and after (b) the application of PID gate 1. On b) the next PID gate is defined.

involved a three-step gating process. First, a gate was placed on a 2-dimensional (2-D) histogram of the fragment's energy loss in the Ionization Chamber (IC_SUM) vs. its total energy as measured in scintillators E1 and E2 (E_TOT). An example is given in Fig. 3.1.

For an ideal S800 experiment, this gate would be very effective in suppressing contaminants. Unfortunately, one of scintillator E2's photo-multiplier tubes was spontaneously jumping between two gain settings, the higher of which resulted in signals from beam projectiles being off-scale. Therefore, only one PMT from E2 was utilized for PID. An attempt was made to correct this lone E2 signal for position sensitivity. E_TOT is a parameter which includes these corrections.

The next step in the ^{18}O identification process involved applying a condition

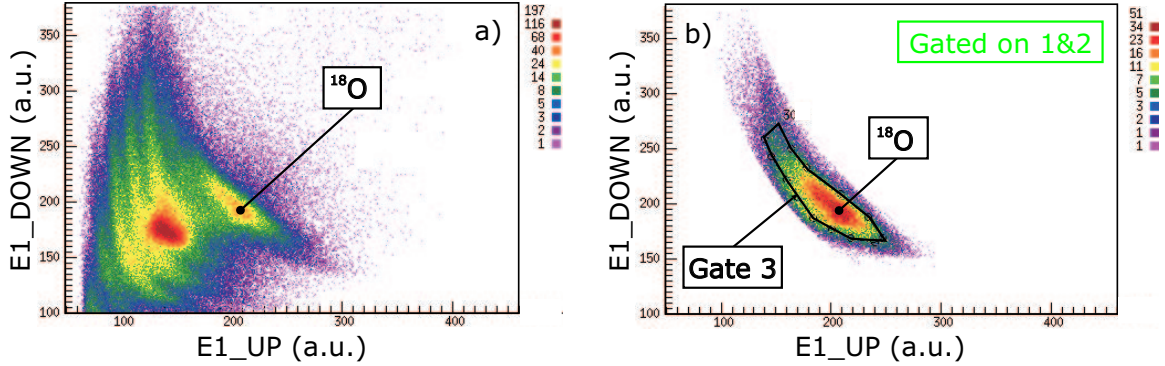


Figure 3.3: A 2-D histogram of E1_DOWN vs. E1_UP before (a) and after (b) the application of PID gates 1 and 2. Note the appearance of lighter-mass bands below the ^{18}O band in a). The final PID constraint is shown in b).

on T.O.F. and ΔE parameters. As discussed in Sec. 2.1.3, the T.O.F. parameter, RF_E1_TAC, is measured between the S800 master (the E1 signals) and the cyclotron RF. The ΔE parameter used in this step is the geometric mean of the signals from scintillator E1, defined as,

$$\text{E1_GEO_MEAN} = \sqrt{\text{E1_UP} \times \text{E1_DOWN}} .$$

The advantage of defining E1's ΔE parameter in this way is that the detector's position sensitivity has been effectively removed. Fig. 3.2b shows an example of this PID gate.

The final, arguably redundant, step in ^{18}O identification is shown in Fig. 3.3b. A constraint was placed on the individual PMT signals E1_UP and E1_DOWN. Fig. 3.3a is an example of a 2-D histogram of these parameters before any gating has been applied. Note the appearance of lower-mass contours below the uppermost band, ^{18}O . Application of the gates 1 and 2 has removed all contaminants from this upper-band.

Particle identification for ^{20}O followed in a similar fashion. As was the case for ^{18}O , the first condition was applied to the ΔE and E parameters IC_SUM and E_TOT. (For ^{20}O scintillator E1's contribution to E_TOT was ignored.) Scintillator E1 was then constrained with the application of a gate similar to step three in the ^{18}O PID. These

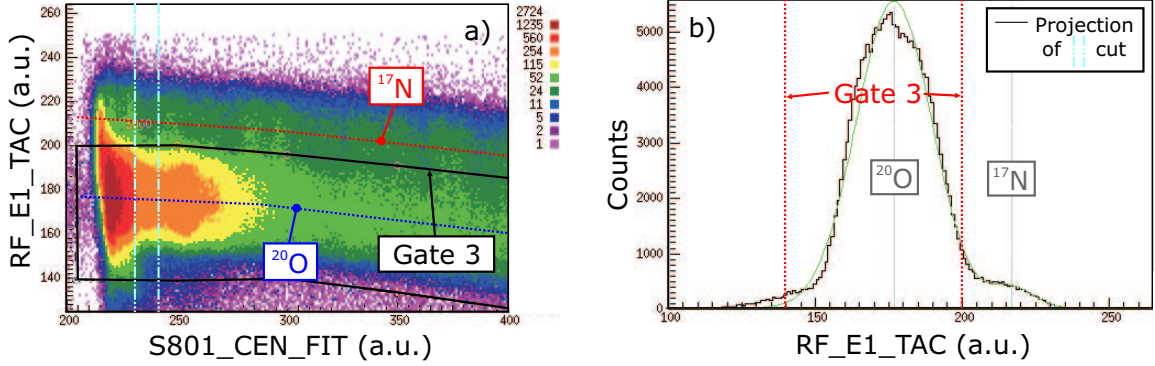


Figure 3.4: a) A 2-D histogram of RF_E1_TAC vs. S801_CEN_FIT which illustrates the final step in the ^{20}O identification process. The contaminant appears as the upper band. b) A projection of the dot-dashed cut in a) onto the T.O.F. axis along with the projection of the final ^{20}O gate. The contaminant is removed.

two conditions, applied together, were successful in the suppression of all reaction fragments. However, the beam contaminant which was mentioned in Chapter 2, ^{17}N , was not fully removed by the application of the first two gates. Therefore, a final constraint was applied to the parameters representing T.O.F. and raw dispersive position at the focus, S801_CEN_FIT (see Fig. 3.4).

3.1.2 CRDC mask calibration

Trajectory reconstruction for the $^{18,20}\text{O}$ beam particles depends on their positions and angles at the focus. Deducing this trajectory information required a calibration of each CRDC detector. To accomplish this, a de-focused beam was sent through the S800 which then illuminated a “mask” positioned in front of each CRDC. A pattern emerged in the resulting x and y data from each detector which mirrored that of the strategically-spaced holes in the mask. The known spacing between the holes of the mask was then used to calibrate each detector. It should be mentioned that because the spacing between cathode pads in the CRDCs is known, and their positions fixed, these detectors are, in a sense, self-calibrated in the dispersive direction. The dispersive mask calibration is therefore redundant, but a nice verification nonetheless.

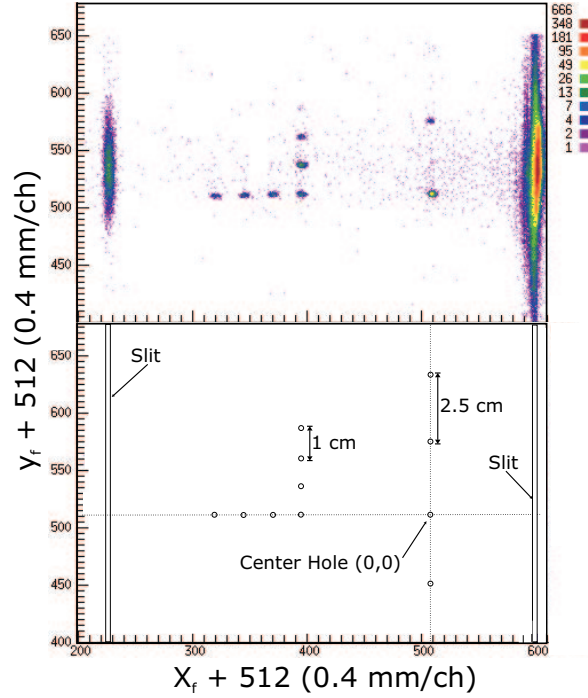


Figure 3.5: Calibrated mask spectra from CRDC1 along with a template of the mask.

3.1.3 Corrections to S800 parameters

TAC corrections

The raw S800 timing parameters displayed shifts, or drifts, over the course of the experiments. To quantitatively monitor these problems, data was grouped in blocks according to run number; in general, one inelastic scattering run encompassed about an hour of uninterrupted acquisition. The mean parameter value over each run was recorded and, in general, treated as an offset for subsequent analysis.

For example, RF_E1_TAC, the raw S800 T.O.F. parameter, deviated by ~ 200 channels or ~ 2.4 ns over the ^{18}O runs and by ~ 250 channels or ~ 3.0 ns over the ^{20}O runs (See Fig. 3.6). A slow drift in the RF signal from the K1200 was suspected as the cause for this problem, as evidenced by a similar problem with MCP timing which is also measured against the cyclotron's RF. As will be explained in Sec. 3.2.2,

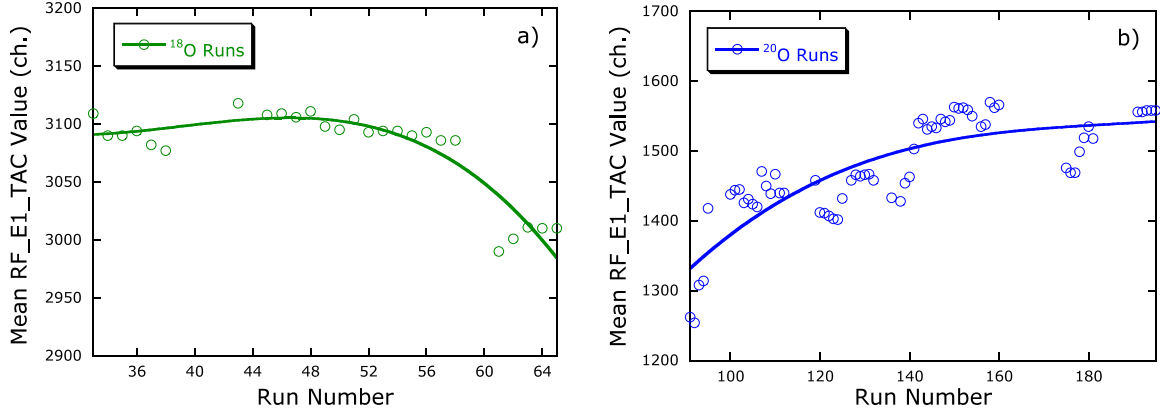


Figure 3.6: The mean value of the S800 raw parameter RF_E1_TAC for ^{18}O (a) and ^{20}O (b) plotted as a function of the run number. The scale on the y-axis is 12.15 ps/ch. The fits are included merely to accentuate the trend.

S800 T.O.F. was subtracted from the raw BaF₂ times to arrive at a parameter which represented γ -ray T.O.F.. Because the flight path for γ -rays from the target to the array was only ~ 0.5 m, a 2–3 ns drift in S800 T.O.F. was significant, and therefore required a correction.

Also significant was a systematic shift in the raw electron drift-time parameter from CRDC2, S802_TAC, shown as the open squares in Fig. 3.7. This problem, which has been observed in previous studies using the S800 (e.g., Ref. 10), can be attributed to a slow improvement of the CRDC fill-gas. Over the course of the experiment, impurities in the CF₄–C₄H₁₀ mix are removed, resulting in a shorter electron drift-time. Run-to-run fluctuations were also observed in both CRDCs, especially between interruptions in inelastic data-taking (the observable gaps in Fig. 3.7), which typically arose from technical problems with beam-delivery or the S800. These fluctuations likely resulted from the magnetic optics of the beam-line or S800 being slightly perturbed after each technical failure, causing the beam’s average position and trajectory to deviate.

As explained earlier, these raw TAC values directly determine the fragment trajectory parameters y_f and ϕ_f . With a gain on the raw CRDC TAC parameters of ~ 1 mm/20 channels, the systematic drift of CRDC2 was a significant, >1 cm effect,

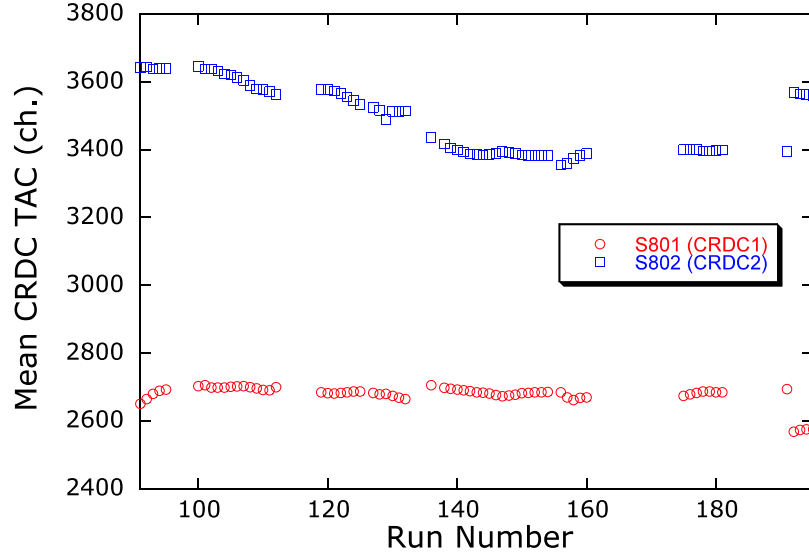


Figure 3.7: The mean value of the raw CRDC drift time parameters plotted as a function of the ^{20}O run number. A systematic shift is observed in CRDC2. Also observed are small fluctuations from run-to-run in both detectors.

while the run-to-run fluctuations in both detectors were on the order of 1 mm. Therefore, the raw TAC parameters from both CRDCs were modified. The mean value over the run was subtracted, so that each CRDC TAC distribution was centered around $y=0$.

Angular corrections

After removing effects related to fluctuations or drifts in raw time parameters, the S800 reconstruction, as explained in Sec. 2.1.1, produced reliable results. Parameters θ_t and ϕ_t , which represented the angular trajectory of the inelastically-scattered projectile as it left the target, were calculated from parameters measured at the focus. Of importance, however, was the fact that the beam, in general, impinged on the target at an angle which slightly deviated from the z -axis (against which the angles θ_t and ϕ_t were measured). Therefore, a calculation of the polar scattering angle, Θ_s , from the dispersive and non-dispersive angles θ_t and ϕ_t , introduced undesirable systematic error. Because knowledge of Θ_s was important for comparisons with the simulation

Table 3.1: The beam’s dispersive and non-dispersive angular offsets.

^{18}O			^{20}O		
Runs	θ_t (mrad.)	ϕ_t (mrad.)	Runs	θ_t (mrad.)	ϕ_t (mrad.)
33–38	-3.8	–	91–95	5.5	-5.6
43–54	-13.6	–	100–112	5.3	-5.7
61–65	-15.1	–	119–125	5.3	-5.8
			127–136	5.3	-5.8
			138–154	5.3	-5.5
			156–160	5.1	-5.7
			175–181	5.1	-5.7
			191–195	4.9	-5.5

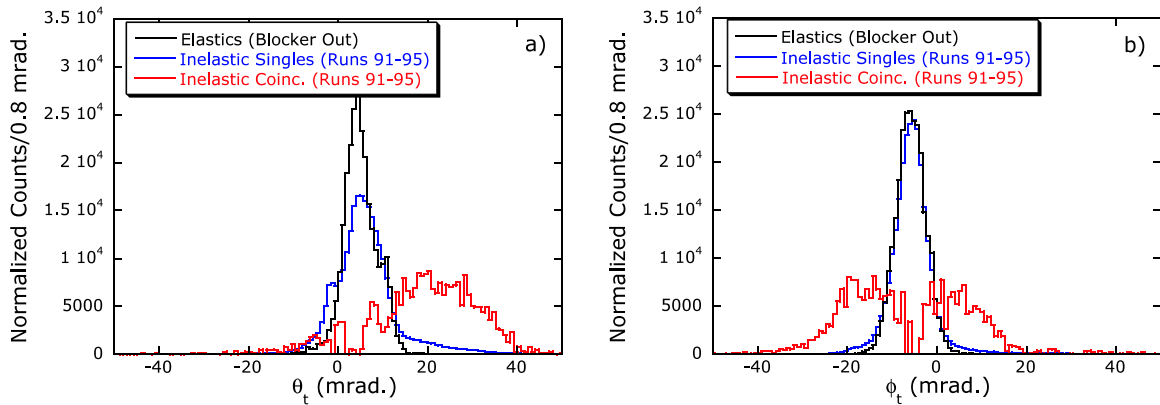


Figure 3.8: Uncorrected ^{20}O θ_t (a) and ϕ_t (b) distributions for runs 91–95, shown with elastic distributions which were recorded immediately before. Notice that the S800 singles events can also be used to monitor the beam. (Normalization is arbitrary.)

(to be described in detail in Chapter 4), a correction was implemented which related θ_t and ϕ_t to the true beam axis.

Table 3.1 lists the dispersive and non-dispersive beam offsets over all inelastic scattering runs for both experiments. For the ^{18}O study, the position of the beam in θ_t and ϕ_t for the elastic scattering runs, recorded before each subset of inelastic scattering runs, was used to determine the offsets. For the case of ^{20}O , however, elastic scattering was monitored less frequently. Thus, the beam offsets for ^{20}O inelastic runs were monitored using S800 singles events, which had distributions that were quite similar to those for elastic scattering. This fact is evidenced by Fig. 3.8, which shows uncorrected dispersive and non-dispersive angular distributions for the subset of ^{20}O

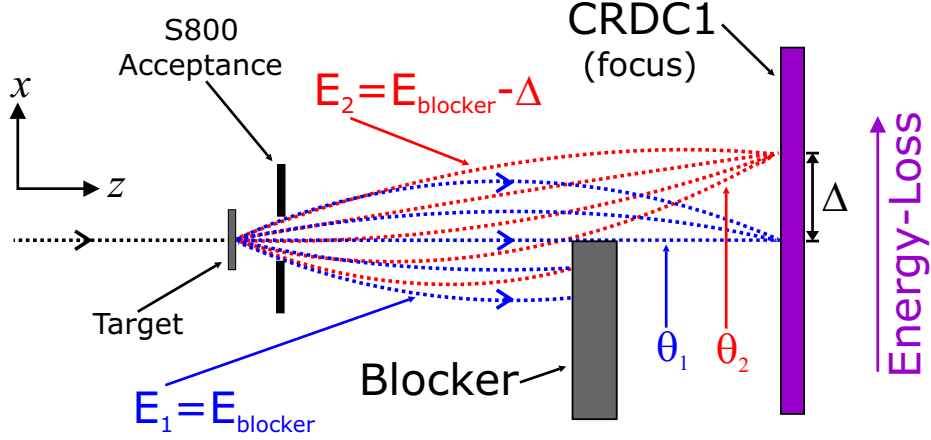


Figure 3.9: A simplified picture to illustrate the effect of the blocker on projectiles reaching the focus. The football-shaped objects represent the envelopes of trajectories in the dispersive plane for the projectiles with energy E_1 and E_2 which are within the S800 acceptance. The blocker cuts into the dispersive trajectory distributions at different angles, θ_1 and θ_2

runs recorded closest to an elastic scattering run.

3.1.4 Effects of the beam blocker on $\theta_{f,t}$

Though vital for the success of the experiment, the presence of the beam blocker in the focal plane nonetheless complicated the resulting angular information obtained. While, in principle, the presence of the blocker should not introduce asymmetry to the non-dispersive angular distributions, $\phi_{f,t}$, the same cannot be said for dispersive angular distributions, $\theta_{f,t}$ (e.g., see Fig. 3.8a). Fig. 3.9 *naively* illustrates the effect of the blocker. From this representation it follows that for the envelope of projectile trajectories which have the same energy-loss, E_1 , at which the blocker is positioned, half of the dispersive angular distribution, or all $\theta < \theta_1$, will be blocked from reaching the focus. Additionally, for trajectories of less-energetic projectiles, represented by the E_2 envelope, the blocker removes less of the distribution.

To minimize non-dispersive asymmetry attributed to use of the blocker, the magnetic field of the S800 was slightly perturbed in an effort to move its focus slightly

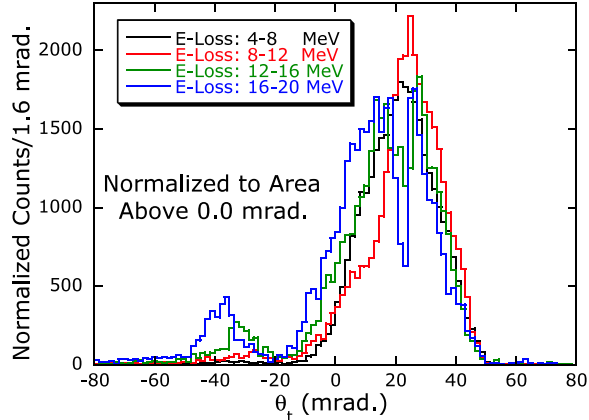


Figure 3.10: ^{18}O dispersive angular distributions, binned by projectile energy-loss. In general, the blocker removes roughly half of the distributions. However, notice the slight increase in counts below 0 mrad. for increasing energy-loss.

upstream so that it coincided with the plane containing the blocker. As can be verified by redrawing Fig. 3.9 with a shifted focus, assuming a blocker of infinitesimal thickness, this process, ideally, would have the effect of completely eliminating the $\theta_{f,t}$ asymmetry. Likely due to a combination of finite blocker thickness and imperfect refocusing, however, asymmetry in the non-dispersive angular distributions persisted. In fact, Fig. 3.10, which shows ^{18}O dispersive angular distributions binned by projectile energy-loss and normalized to the region of positive θ_t , would tend to indicate that the effect demonstrated in Fig. 3.9 is experimentally observed – notice that there are relatively more counts below 0 mrad. for increasing energy-loss.

3.2 γ -ray analysis with the ORNL-TAMU-MSU

BaF₂ Array

3.2.1 Energy calibration

For the experiments, the detectors had been approximately gain-matched by their applied voltages so that they would be capable of digitizing signals from γ -rays up to an energy of ~ 40 MeV. To make reasonable conclusions from the data, the arrays

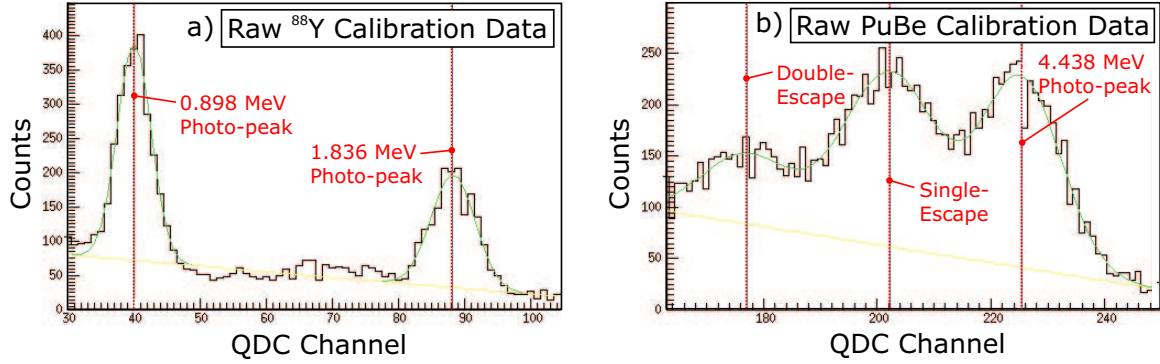


Figure 3.11: Examples of raw ^{88}Y (a) and PuBe (b) calibration data for the same detector. After fitting the spectra in the regions shown, assuming Gaussian-like photo-peaks on top of linear backgrounds, the photo-peak positions are recorded. Note the appearance of the single and double-escape peaks in (b).

had to be more-precisely calibrated in energy. For reasons that will become evident in Sec.3.4.3, it was sufficient to rely on source calibrations using ^{88}Y , which provided two γ -rays with energies of 0.898 and 1.836 MeV, and PuBe, which emits a 4.438 MeV γ -ray.

Examples of raw calibration spectra for a detector which displays particularly good resolution are shown in Fig. 3.11, along with Gaussian photo-peak fits that have been generated assuming linear backgrounds in the regions shown. Two “escape peaks” are visible in Fig. 3.11b because the process of pair-production, (to be discussed in more detail in Sec. 3.2.3), competes with the photo-electric effect in the BaF_2 crystal.

While only one PuBe calibration was performed at the end of the experiments, many ^{88}Y calibrations were performed at regular intervals to monitor time-dependent gain fluctuations in the individual detectors. With the assumption that the relationship between the 4.438 MeV signal-height and that for both ^{88}Y γ -rays be preserved, it was possible to simply extrapolate the 4.438 MeV photo-peak position from the associated ^{88}Y calibration data. A linear regression fit using the two ^{88}Y calibration points and the extrapolated PuBe value then established the precise gain and offset for each detector, as in Fig. 3.12. The general rule for analyzing the S800+ γ -ray coincidence data, then, was to calibrate the arrays with ^{88}Y data gathered nearest in

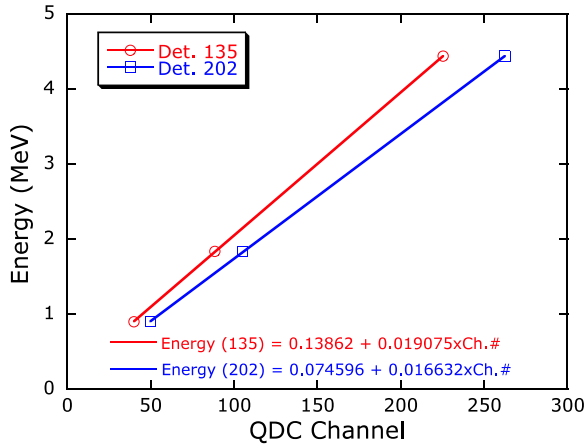


Figure 3.12: Sample calibration fits for detectors 135 and 202. Notice the linear response of the detectors in this energy region.

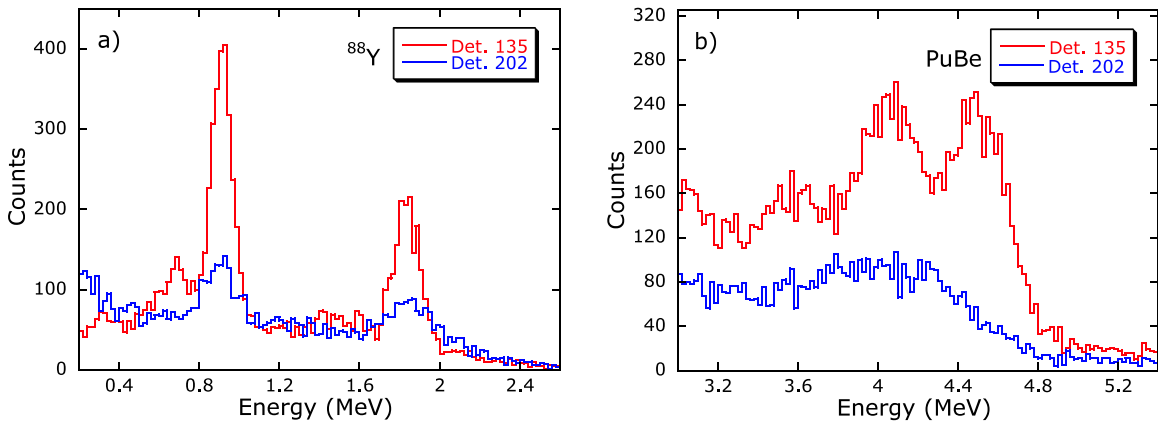


Figure 3.13: ^{88}Y (a) and PuBe (b) calibration data taken simultaneously for detectors 135 and 202, which shows the difference between a detector with good energy resolution and one with poorer resolution.

time to the current inelastic run.

The energy resolution of the detectors in the arrays varied substantially detector-to-detector, as depicted in Fig. 3.13. Detector 135, which has particularly good resolution of $\sim 7.3\%$ FWHM at 4.44 MeV, is shown with data taken simultaneously for detector 202, which displays much poorer resolution. Notice that the escape peaks visible for detector 135 in Fig. 3.13b are not resolved for detector 202.

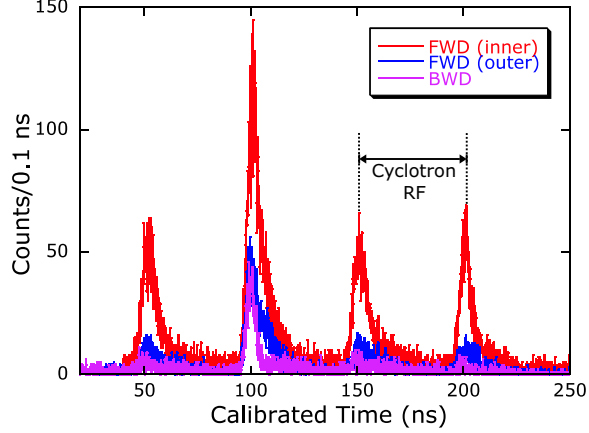


Figure 3.14: ^{18}O BaF₂ time spectra for selected detectors. The peak at 100 ns results from the projectile-correlated events of interest. Overlay-ed on top of this time correlated time peak is a background which displays the periodicity of the cyclotron RF. The detector in the backward (BWD) array sees very little background as compared with the inner detector in the forward (FWD) array.

3.2.2 Background suppression

The individual BaF₂ TDC coincidence gates were such that, on average, peaks from four consecutive beam bursts were visible in the S800+ γ -ray time data. One of these peaks, the most intense, contained the events of interest, namely the projectile-correlated γ -ray events, while the others were the result of neutrons or low-energy γ -rays detected in the array in coincidence with uncorrelated, or random, projectiles arriving at the S800 focus. Because these random projectiles could come from the same or other beam bursts with equal probability, the random feature of the individual time spectra was of periodic structure, mirroring that of the cyclotron's RF. Some sample time spectra are shown in Fig. 3.14 from strategically selected detectors. Notice the inner detector (closer to the beam pipe) of the forward (FWD) array has counted many more background events than either the outer FWD detector or the detector from the backward (BWD) array. Moreover, the periodic structure of the background for the BWD detector has almost disappeared. This is evidence that neutrons were the dominant background contribution, since they would tend to be emitted at forward angles.

T.O.F. analysis

Flight-time constraints could be used to minimize contributions from these random events in the array. A calibration of the individual BaF₂ spectra which made use of the periodic feature of the random background was first performed. The calibration offsets were adjusted to line up the individual projectile-correlated time peaks. As was explained in Sec. 2.2.3, BaF₂ times were measured between S800 master gate, which served as a common start for all detectors, and the individual detector's threshold trigger. Therefore, the raw BaF₂ times were dependent on the projectile's flight time through the S800. Higher-resolution T.O.F. parameters could be constructed by subtracting this S800 flight time from the individual BaF₂ calibrated time parameters. Specifically, an event's RF-to-array flight time, $\text{T.O.F.}_{(\text{RF-Array})}$, could be reconstructed using the following:

$$\text{T.O.F.}_{(\text{RF-Array})} = \text{CBAFT} - a \times \text{RF_E1_TAC} + b .$$

Here CBAFT is the calibrated BaF₂ time parameter, a is a gain-matching constant, and b is some arbitrary offset.

Since the momentum spread of the beam in the case of the ¹⁸O study was narrow, the beam's flight from the K1200 to the target introduced very little additional spreading. Therefore, for the ¹⁸O experiment, the calculated $\text{T.O.F.}_{(\text{RF-Array})}$ essentially differed from the $\text{T.O.F.}_{(\text{Targ.-Array})}$ by only a constant, i.e.,

$$\text{T.O.F.}_{(\text{RF-Array})}^{18\text{O}} \simeq \text{T.O.F.}_{(\text{Targ.-Array})}^{18\text{O}} + \text{Const.}$$

A comparison of the resulting $\text{T.O.F.}_{(\text{RF-Array})}$ data for ¹⁸O and ²⁰O, as in Fig. 3.15, verifies the expected result that the prompt, projectile-correlated γ -ray peak is better-resolved in the primary beam experiment with ¹⁸O. Recall, however, that the multi-

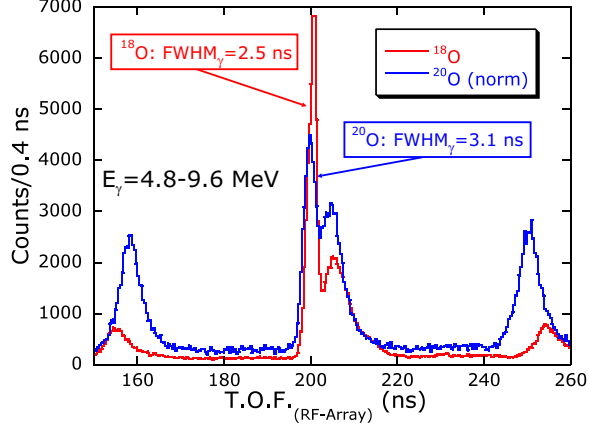


Figure 3.15: A comparison of the calculated $T.O.F._{(RF-Array)}$ parameter for ^{18}O with that for ^{20}O , summed over contributions from all detectors. The ^{20}O data has been normalized to the ^{18}O such that the area under the prompt- γ peaks is roughly equivalent. A γ -ray energy constraint was implemented to minimize the spreading due to LED walk. Notice that the projectile-correlated γ -rays are better resolved in the ^{18}O data.

channel plate timing detectors were introduced into the ^{20}O set-up for precisely this reason.

Better resolved flight-time parameters, $T.O.F._{(MCP_{1,2}-Array)}$ are, in principle, attained by using the relation,

$$T.O.F._{(MCP_{1,2}-Array)} = CBAFT - T_MCP_{1,2} + b ,$$

since $T_MCP_{1,2}$, the individual multi-channel plate timing signal, is measured in reference to the S800 master gate. These parameters measure flight-time that is directly tagged with the beam projectile at the position of the MCP detector. The approximate relation,

$$T.O.F._{(MCP_{1,2}-Array)} \simeq T.O.F._{(Targ.-Array)} + \text{Const.} ,$$

is therefore restored. The closer the individual multi-channel plate detector is located to the target, the better this approximation, since, in reality, the constant which

equates the two T.O.F. parameters is dependent on the individual beam-particle’s velocity.

In practice, however, it was difficult improve, resolution-wise, on the T.O.F._(RF-Array) results obtained for the ²⁰O study. Efficiency losses of ~52% and ~88% in MCP1 and MCP2, respectively, resulted in much poorer statistics for the individual MCP T.O.F. measurements, introducing more inherent error in the prompt- γ alignment process. For reasons that will become clear in Sec. 3.4.3, constraints placed on T.O.F._(RF-Array) were found to be sufficient. Being no longer dependent on the multi-channel plate detectors, a ~100% increase in overall ²⁰O counts was regained, which was beneficial.

Fast vs. slow gating

Use of “Fast vs. slow gating,” which takes advantage of Barium Fluoride’s PSD capabilities (described in Sec. 2.2.2), was also useful for background suppression. γ -rays were separated from neutrons (charged-particles) when detector’s fast QDC signal was plotted against the calibrated slow QDC signal, as shown in Fig. 3.16. The γ -rays appear as the streak found just above that of the neutrons which becomes visible near 10 MeV. It is worthwhile to mention that the neutrons which are discernible have actually undergone collisions with protons in the BaF₂ crystal; it is the moving protons

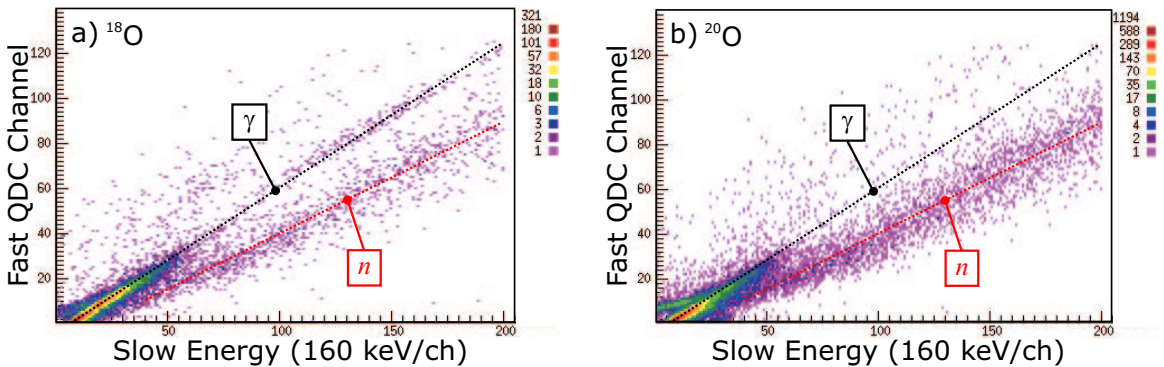


Figure 3.16: A comparison of a fast vs. slow 2-D histograms generated for a particular BaF₂ forward detector using data from the ¹⁸O (a) and ²⁰O (b) study. Neutrons appear below the γ -rays on these plots. A relative increase in neutrons is observed for the case of ²⁰O.

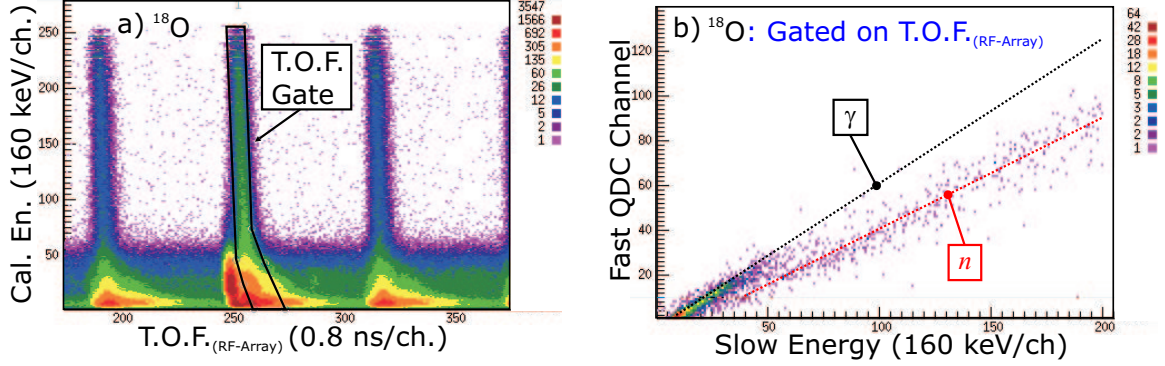


Figure 3.17: A gate placed a 2-D plot of calibrated BaF₂ energy vs. T.O.F._(RF-Array) (a) is used to constrain the ¹⁸O fast vs. slow histogram from Fig. 3.16, which appears as (b) here. It's apparent that the random background is made of mostly neutrons and lower-energy γ -rays.

which interact, creating light pulses. A comparison of a fast vs. slow 2-D histogram generated with ¹⁸O data against that generated with ²⁰O demonstrates, as expected, that more neutrons were present for the secondary beam experiment.

The claim that neutrons and low-energy γ -rays dominated the random background is verified by a comparison of Fig. 3.16a with Fig. 3.17b. The T.O.F._(RF-Array) gate shown in Fig. 3.17a, placed just to the right of the prompt γ -ray peak, has been used as a constraint in generating the fast vs. slow plot in Fig. 3.17b. The streak resulting from neutrons has been enhanced relative to the γ -ray band by application of this gate, while, on average, the γ -rays are of lower energies.

3.2.3 Shower reconstruction

γ -ray events, having been selected by use of T.O.F.-gating in tandem with the application of fast vs. slow gating, were analyzed using shower reconstruction, which is the summing of energy that is simultaneously deposited in neighboring BaF₂ detectors. In general, the process of converting photons to fast electrons, which are ultimately responsible for light production in the BaF₂ crystals, is complex. Essentially three types of interactions compete to produce these fast electrons, namely the

photo-electric effect, Compton scattering, and electron-positron pair production [19].

The photo-electric effect, which typically dominates for photon energies under ~ 1 MeV, is the process by which the photon is absorbed in an atom of the crystal and then replaced by an energetic electron which has been displaced from the atom's K shell. The electron, therefore, carries away the photon's energy minus the K shell binding energy (~ 10 keV) in the form of kinetic energy. Compton scattering dominates in the region of ~ 1 – 10 MeV. This process can be thought of as the scattering of the incident photon from an atomic (essentially free) electron, which then recoils, carrying away a portion of the original photon's energy. The Compton scattering process is represented by

$$E'_\gamma = \frac{E_\gamma}{1 + \frac{E_\gamma}{m_0 c^2} (1 - \cos \theta)}, \quad (3.1)$$

where E_γ and E'_γ are the energies of the incident and outgoing photon, respectively, m_0 is the electron rest energy (0.511 MeV), and θ is the angle of the outgoing photon with respect to the incident photon's direction. Notice that at maximum electron recoil, which occurs at $\theta = \pi$, the photon retains a portion of its initial energy.

The last of the competing processes, pair-production, dominates for higher-energy γ -rays. The incident photon is replaced by an electron-positron pair such that total momentum and energy is conserved. For this to be energetically possible, the incident photon must have an energy of at least 1.02 MeV, or twice the electron rest mass. The positron eventually slows in the crystal and then annihilates with an electron, causing the emission of back-to-back 0.511 MeV photons. Pair production is therefore responsible for "escaped" 0.511 MeV photons, when one or both of these annihilation photons leaves the boundary of the absorbing crystal and is lost. This was the cause of the escape peaks which were visible in Fig. 3.13.

For a given photon which was incident on the array, then, the competition from

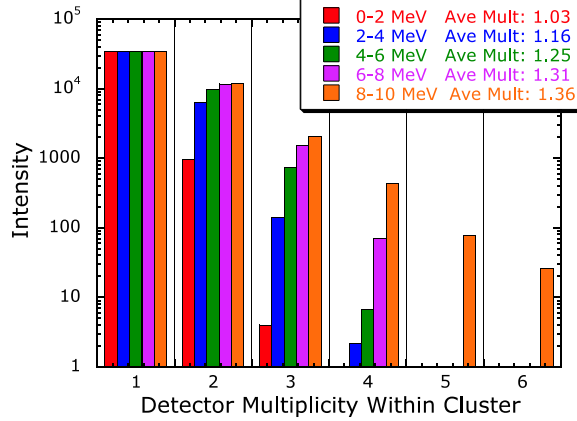


Figure 3.18: The number of detectors participating, or the cluster multiplicity, binned by incident γ -ray energy in steps of 2 MeV for photons provided by the ^{20}O experiment. The data from energy bins above 2 MeV has been normalized to the 0–2 MeV bin for multiplicity=1 events. Average cluster multiplicity increases with incident photon energy.

these photon-to-electron conversion processes caused energy to be deposited in more than one detector simultaneously. A single incident photon, therefore, could result in a cluster, or shower, of neighboring “hits” over which the photon’s energy was distributed. On average, as expected, the number of participating detectors increased with photon energy. This trend is evident in Fig. 3.18, which shows detector multiplicity binned as a function of incident photon energy for sample ^{20}O data.

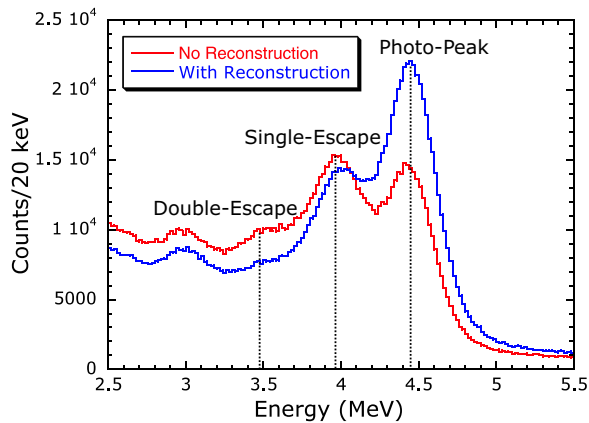


Figure 3.19: Sample PuBe calibration data showing the improvement of the array response when shower reconstruction is employed. Notice that counts have been effectively “put back” into the photo-peak.

Shower reconstruction, on an event-by-event basis, therefore vastly improved the response of the BaF₂ arrays. Its importance is visually demonstrated by Fig. 3.19 which shows sample PuBe energy calibration data that has been expanded in the region near the 4.438 MeV photo-peak and the neighboring escape peaks for data taken with and without multiple-hit energy reconstruction.

3.2.4 Doppler correction

Also important to γ -ray energy reconstruction for these experiments was Doppler correction. Photons which originated from ¹⁸O and ²⁰O nuclear de-excitations were emitted in reference frames which were moving at relativistic velocities ($\beta \simeq 0.4$) with respect to the laboratory coordinate system. The well known Doppler shift equation (e.g., Ref. 16) describes the relationship between the γ -ray energy in the rest (E'_γ) and laboratory (E_γ) frames:

$$E'_\gamma = \gamma E_\gamma (1 - \beta \cos \theta) . \quad (3.2)$$

Above, θ is the angle of the emitted photon with respect the rest-frame's direction in the laboratory frame, and

$$\gamma = \frac{1}{\sqrt{1 - \beta^2}} . \quad (3.3)$$

The inherent segmentation of the array allowed for a determination of the angle θ . For example, the detector within an event cluster recording the largest energy signal, labeled as the “primary” detector, could be taken as the detector in which the incident photon interaction occurred. To a first approximation, the position of the center of the face of the primary detector then gives the interaction point of the incident photon. An assumption is then made that all projectiles initially travel along the beam axis. In principle, improvement on the angle determination is achieved by

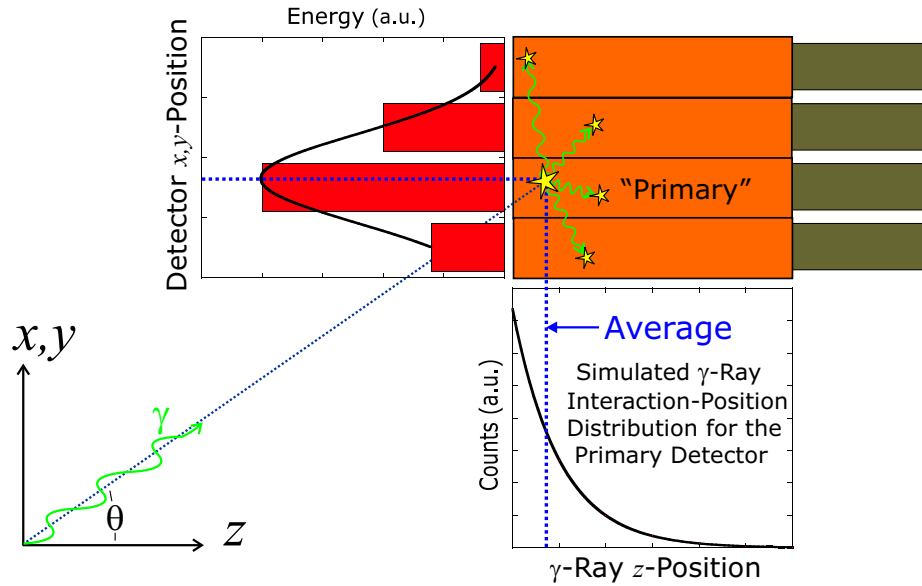


Figure 3.20: A representation which describes how the γ -ray emission angle, θ , was determined event-by-event.

considering the energy distribution for participating detectors within a cluster. As depicted in Fig. 3.20, for the experiments, the interaction position of the incident γ -ray in the plane transverse to the beam-line was actually determined by energy-weighting over participating detectors. As a further improvement, the interaction position along the beam-line was found using the statistical average for the primary detector which had been determined with help from simulation. (The simulation, which was performed using a GEANT [3] environment, will be described in detail in Chapter 4.) Likely due to the low average cluster multiplicity which was observed in these studies (as given in Fig. 3.18), these θ -determination improvements had barely-measurable effects on the resulting Doppler-corrected data.

3.3 Beam rate monitoring with the MCP detectors

Aside from aspects related to projectile-correlated γ -ray timing, an additional impetus for the inclusion of the multi-channel plate (MCP) timing detectors into the ^{20}O experimental set-up was the desire to count the incoming beam projectiles. This information is especially useful for converting experimental γ -ray yields into units of photon scattering cross section, which are more informative in the sense that they are universal. The extraction of a true ^{20}O counting rate from either MCP detector, N_{MCP} , in principle, involves the determination of its counting efficiency, ϵ , since

$$N_{\text{MCP}} = \frac{P \cdot D \cdot n_{\text{MCP}}}{\epsilon}, \quad (3.4)$$

where n_{MCP} is the raw MCP counting rate, P is the purity of the secondary beam and D is the inverse of any down-scaling factor that applies. For this experiment, ϵ could be determined by comparing the S800 (CRDC) counting rate with that of the MCP for target-in, blocker-out sets of data. Unfortunately, only one such target-out (elastic scattering) run was recorded on tape at the beginning of the ^{20}O experiment, thereby allowing for only one determination of the MCP efficiencies. After calculating the run-by-run integrated number of beam particles for each detector, using the method prescribed above, it became immediately obvious that the MCP detectors displayed some unpredictable behavior. Specifically, a comparison of the run totals from each detector, run-by-run, revealed inconsistencies that could only have been caused by large counting efficiency fluctuations in both detectors, unfortunately deeming any counting information from these detectors unreliable.

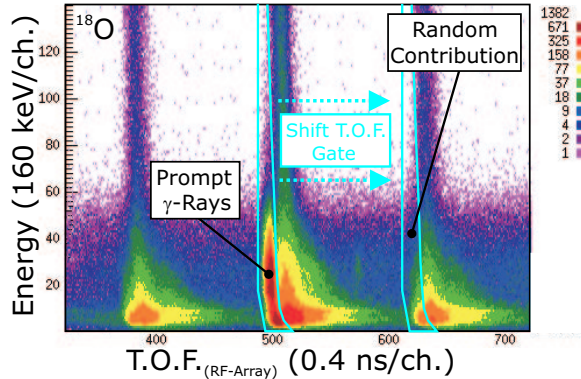


Figure 3.21: T.O.F. vs. energy for ^{18}O data showing the prompt γ -ray gate along with the shifted gate which samples the background.

3.4 Experimental results

3.4.1 Random background removal

As was explained in Sec. 3.2.2, high-resolution T.O.F. parameters were constructed for prompt γ -ray selection, therefore minimizing the random contribution to subsequent BaF_2 analysis. However, by virtue of the BaF_2 coincidence window-length which included several beam bursts, resulting in the periodic structure for the random events, it was possible to sample the random contribution within the prompt- γ gate by simply shifting the T.O.F. gate by one RF period. As an example, Fig. 3.21 shows the placement of the prompt and shifted gates on ^{18}O T.O.F. vs. energy data.

3.4.2 S800– BaF_2 energy correlation

Appropriately, final event selection involved placing simultaneous energy constraints on the S800 and BaF_2 results. It was required that projectile energy-loss, as measured with the S800, be correlated with reconstructed, lab-frame, γ -ray energy. Examples of this selection process are given in Fig. 3.22, which shows data from both the ^{18}O and ^{20}O study (plots (a) and (c), respectively). Projectile energy loss is on the vertical axis while γ -ray energy captured in the forward array is plotted on the horizon-

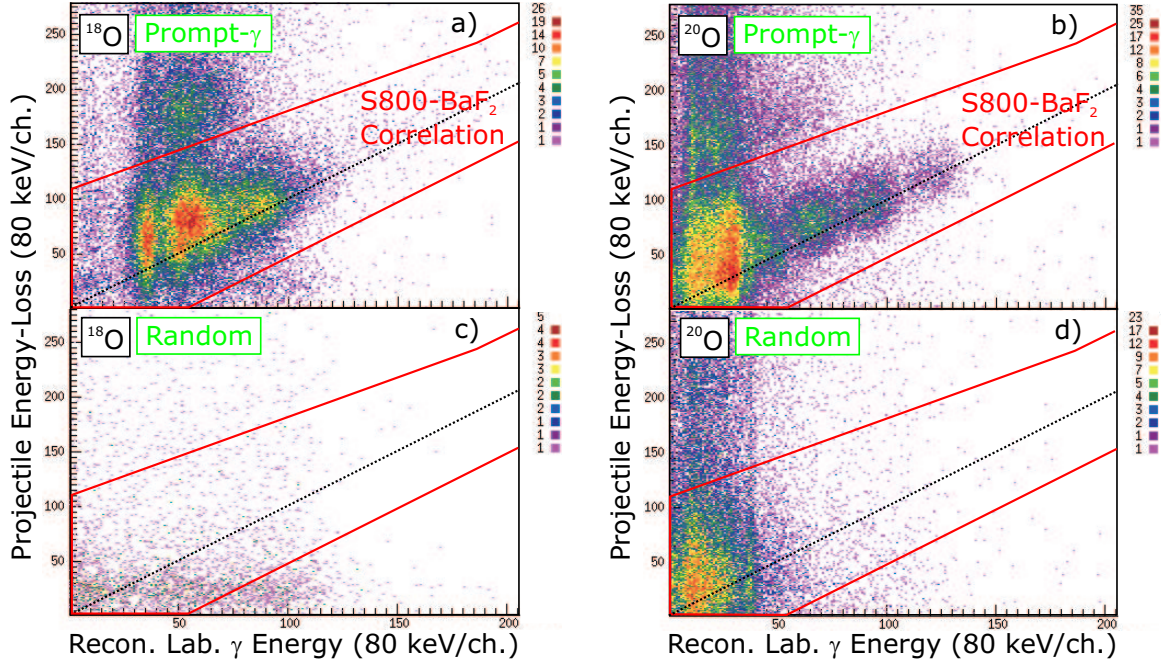


Figure 3.22: Shows the final event selection for the ^{18}O (a) and ^{20}O (b) studies. A gate is drawn on a projectile energy-loss vs. reconstructed, forward, laboratory-frame, γ -ray energy histogram. The same gate is placed on equivalent histograms generated with the shifted time gates, (c) and (d).

tal. Note the enhancement of events appearing along the diagonal, which represents cases where projectile energy-loss is fully-recovered in the array. This final energy constraint was inclusive of events falling left of the diagonal, which resulted specifically from cascade decays whereby the projectile's de-excitation process proceeded through an intermediate state; one (or more) of the resulting γ -rays was not detected. Also included in Fig. 3.22 (plots (c) and (d)) are equivalent spectra which have been generated with shifted T.O.F. gates. These histograms therefore represent the background which has been unavoidably included in (a) and (b). All data included within these energy gates was then projected onto the Doppler-corrected BaF₂ energy axis. Examples are given in Fig. 3.23, plotted on a logarithmic scale. A subtraction of the random-gated spectrum from the prompt- γ -gated spectrum produced the final results for these experiments.

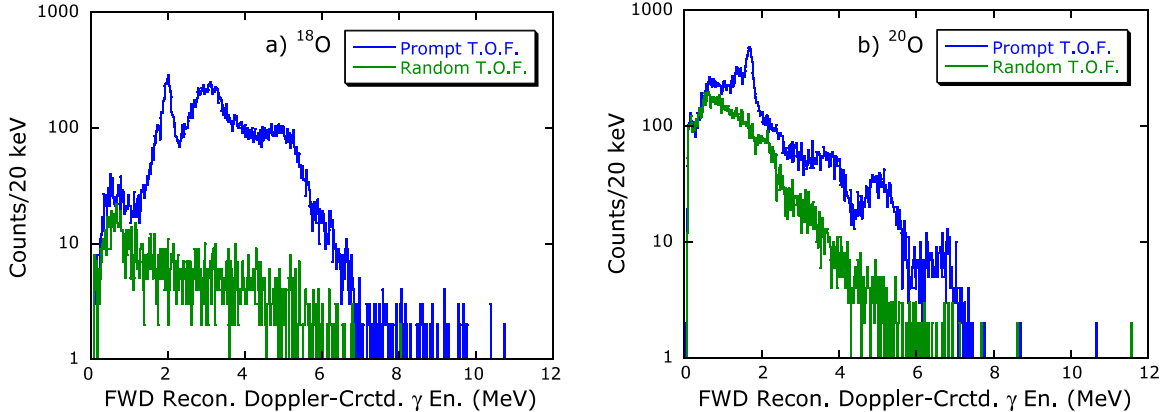


Figure 3.23: Projection of events included within energy gates shown in Fig. 3.22 onto the Doppler-corrected axis for the ^{18}O (a) and ^{20}O (b) experiments.

3.4.3 ^{18}O and ^{20}O strength distributions

The effectiveness of this background removal technique is demonstrated by comparing the final background-subtracted strength distributions with equivalent data generated using less constraining background suppression. Fig. 3.24 shows the final, Doppler-corrected, experimental results for both studies (black) along with data generated entirely without the use of fast vs. slow gating (red) and also with data generated using widened T.O.F. gates (blue). More specifically, the T.O.F. gates used for these blue curves were expanded to encompass the width of an entire beam burst. Impressive is the fact that no difference in the final result is observed when the background suppression techniques are relaxed. This allowed, for example, greater timing flexibility with the ^{20}O experiment, which justified the decision not to rely on the multi-channel plate detectors for higher-resolution timing.

Note the appearance of the pronounced peaks at ~ 2 and ~ 1.7 MeV in the ^{18}O and ^{20}O strength functions, respectively. These peaks resulted from de-excitations from the first-excited 2^+ states, which produce γ -rays of 1.98 MeV for ^{18}O and 1.67 MeV for ^{20}O [34, 35]. Observation of these peaks at the proper location in energy is experimental verification of the Doppler-correction process and of proper identification of the projectiles. Broader structures were observed at energies above the sharp 2^+

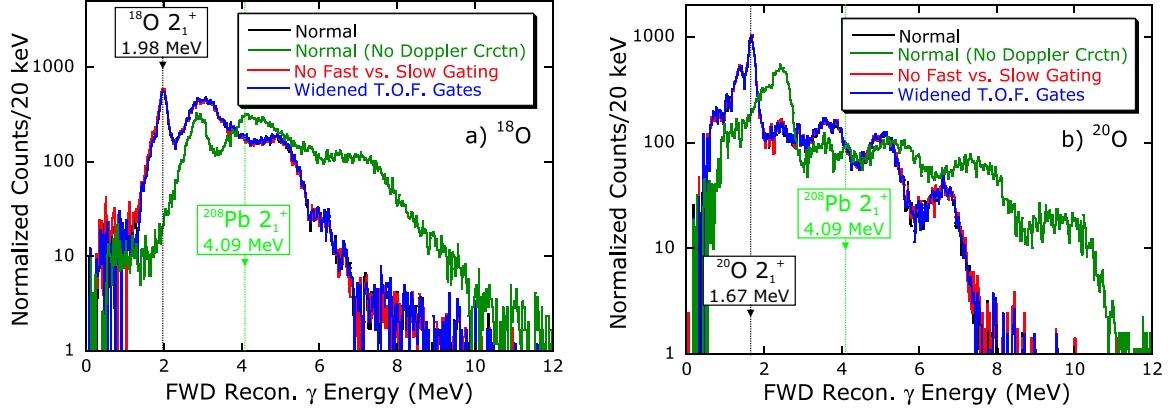


Figure 3.24: Shown in black are the final, Doppler-corrected, experimental strength distributions for ^{18}O (a) and ^{20}O (b), respectively. For comparison, the same results are obtained with no fast vs. slow gating (red) and with widened T.O.F. gates (blue).

states but below the neutron separation energies, S_n (8.044 and 7.608 MeV for ^{18}O and ^{20}O , respectively). These wider peaks were the result of contributions from several, higher-lying, discrete projectile levels in addition to a background contribution from excitations of the first-excited 2^+ in the ^{208}Pb target (4.085 MeV) [23]. The target contribution becomes more evident when looking at the green curves of Fig. 3.24, which are the non-Doppler-corrected distributions, since the target can be considered at rest in the laboratory.

As alluded to in Sec. 1.1, evident in Fig. 3.24 is the fact that essentially no appreciable statistics were gathered for γ -rays of energy greater than S_n for either study. This was the direct result of the cross-section for GDR Virtual Photon Scattering being too low given the available beam currents and energies. In addition, at the time the experiment was proposed, the acceptance of the S800 had been overestimated. (An analysis pertaining to this topic will be the subject of Sec. 5.2). To interpret the experimental results, draw conclusions, and ultimately make comparisons regarding dipole strength in these two nuclei, it was necessary to focus on the region in energy of the discrete transitions, where other virtual excitation-photon multipolarities were contributing. To this end, a Monte Carlo simulation was utilized which included

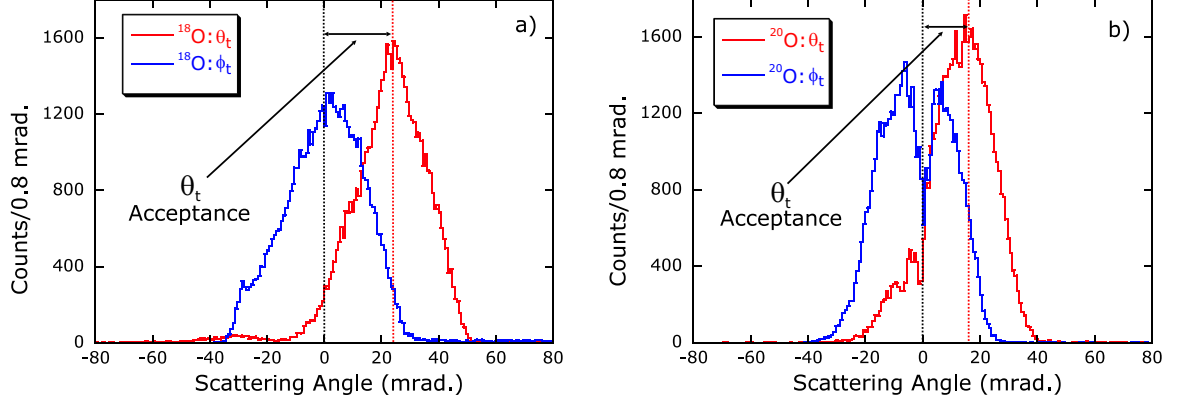


Figure 3.25: Final ^{18}O (a) and ^{20}O (b) angular distributions. The ϕ_t distributions, as expected, are relatively symmetric, while the blocker distorts the θ_t distributions. Approximate acceptance cuts are visible in the θ_t distributions.

Coulomb excitation formalism into the useful environment provided by GEANT [3], which could simulate BaF₂ detector response.

Important information stood to be gained from a more detailed analysis, as the level structure of ^{20}O has not been well explored. As was mentioned in Chapter 1, with the exception of that for transitions from the first-excited state in ^{20}O , no reduced transition probability ($B(E\lambda)$) values, which are critical for Coulomb excitation calculations, have been measured previously [26]. Additionally, knowledge of the level scheme for negative-parity states in ^{20}O is incomplete. Results from the analysis, therefore, emerged after making appropriate adjustments to theoretical predictions for specific states in ^{20}O . Important $B(E\lambda)$ information was obtained for ^{20}O , along with the observation of previously unmeasured 1^- states. All important details of the analysis involving the Monte Carlo simulation of these experiments will be explained in Chapter 4.

3.4.4 ^{18}O and ^{20}O angular distributions

The final experimental angular distributions are shown in Fig. 3.25. The θ_t data shows S800 acceptance cuts at approximately 20 mrad which is $\sim 2/3$ of the expected

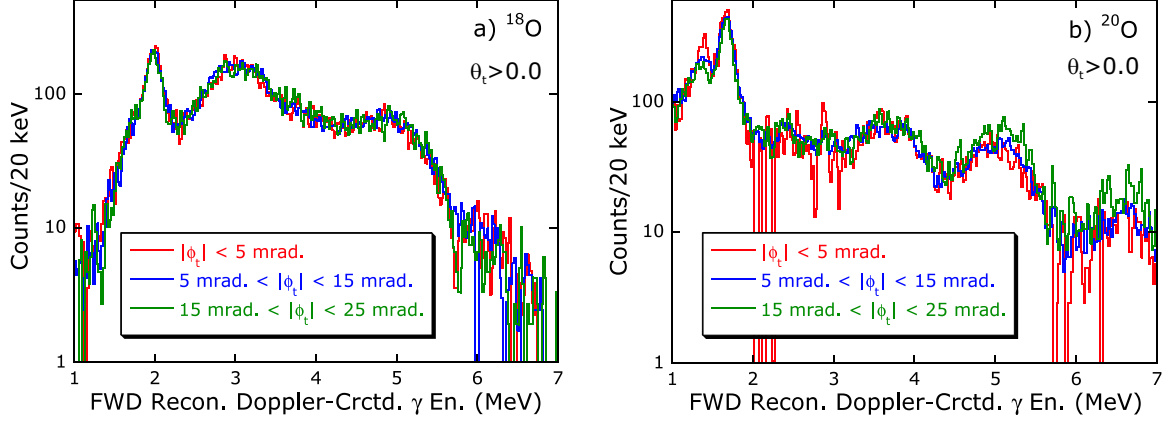


Figure 3.26: Comparison of Doppler-corrected strength distributions obtained after gating on the specified regions in ϕ_t for ^{18}O (a) and ^{20}O (b). The constraint, $\theta_t > 0.0$, was used in generating these histograms. The curves shown in red and green have been normalized to the data represented in blue.

value. The more-limited acceptance observed in the ϕ_t distributions, meanwhile, is a result of the angular constraint from the momentum slits. It should be noted that the non-dispersive distributions, as anticipated, are reasonably symmetric. Unexpected, however, are the differences between these ϕ_t distributions for the two experiments. Specifically, the ^{18}O ϕ_t distribution is single-peaked, while that for ^{20}O exhibits the expected double-peak. (Double-peaking is expected because the differential Coulomb excitation cross sections for all projectile and target states are zero at $\vartheta = 0$.) As will become evident in Chapter 4, the difference can be explained when the overall shape of the S800+blocker acceptance as observed in (θ_t, ϕ_t) space is considered. This 2-dimensional acceptance contour for the case of ^{20}O is more symmetric about $\phi_t = 0$ than it is for the ^{18}O study.

Fig 3.26 shows final strength distributions generated after gating on different regions of the non-dispersive angular distribution for both ^{18}O and ^{20}O . The slight differences which are noticeable (especially for ^{20}O) are due to the differing shapes of the angular distributions for the discrete excitations which are contributing. For example, excitations occurring via absorption of $E1$, $E2$ and $E3$ photons are each described by characteristic angular distributions.

Chapter 4

Interpretation of experimental results

To gain a better understanding of the experimental results for this study, and ultimately extract information regarding dipole strength in the discrete region of ^{20}O , a Monte Carlo simulation was developed and employed. The simulation made use of the intermediate-energy Coulomb excitation formalism discussed in Chapter 1 to incorporate the inelastic excitation processes which occurred in both the projectile and the target. This treatment was adequate since inelastic nuclear processes are negligible given the small acceptance for these experiments ($\sim 1^\circ$ in the lab-frame). γ -ray analysis was performed by the realistic radiation detection code GEANT [3], which was developed at CERN (Geneva, Switzerland). GEANT's capabilities are such that the γ -ray detection materials and geometries which were specific to the current study could be defined rather conveniently. S800 resolution constraints were applied to outgoing projectile angles and energies so that appropriate energy gates and angular acceptance cuts could be placed on the simulated events.

Because all quantities which are relevant to Coulomb excitation and subsequent γ -ray decay (such as spin and energy of states, $B(E\lambda)$ information, and γ ray de-

cay branching) are known for ^{18}O , appropriate adjustments could be made to the simulation upon comparison with the actual ^{18}O experimental results. A confident extension of the simulation to the ^{20}O case, with help from theoretical predictions, could then follow. Using a comparative analysis of simulated against experimental data, quantitative interpretations of the ^{20}O results were possible.

4.1 The simulation

4.1.1 Selection of the excitation channel

As was made evident by the comparison of total excitation cross section information in Sections 1.3 and 1.4, it was essential that target excitations be included into the analysis. The process of assigning an excitation channel in either the projectile (A) or the target (B), event by event, was consistent with the relative probabilities, P_n^A and $P_{n'}^B$ calculated from total cross section information.

$$P_n^A = \frac{\sigma_n^A}{\sum_n \sigma_n^A + \sum_{n'} \sigma_{n'}^B} ; \quad P_{n'}^B = \frac{\sigma_{n'}^B}{\sum_n \sigma_n^A + \sum_{n'} \sigma_{n'}^B} . \quad (4.1)$$

Defined in such a way, the probabilities given above have the convenient property,

$$\sum_n P_n^A + \sum_{n'} P_{n'}^B = 1 . \quad (4.2)$$

In Eq. 4.1 σ_n^A ($\sigma_{n'}^B$) represents the total Coulomb excitation cross section for the n^{th} (n'^{th}) excited state in the projectile (target) obtained by an integration over ϑ of the corresponding differential cross section expression, $d\sigma_n^A/d\vartheta$ ($d\sigma_{n'}^B/d\vartheta$), to some (C.M.-frame) maximum angle, $\vartheta_{n,max}^A$ ($\vartheta_{n',max}^B$). This maximum center-of-mass angle was calculated from a corresponding laboratory-frame angle, which was chosen to be well-beyond the experimental acceptance. In general, the relationship between the

scattering angle in the two frames contains a dependency on the excitation energy (see Appendix A) so that, for example,

$$\vartheta_{i,max}^A = \vartheta_{i,max}^A(E_i^*, \theta_{max}^{lab}) \neq \vartheta_{j,max}^A = \vartheta_{j,max}^A(E_j^*, \theta_{max}^{lab}) .$$

However, the fact that the excitation energies for the states in this study were small in comparison with the kinetic energy of the projectile allows

$$\vartheta_{i,max}^A \simeq \vartheta_{j,max}^A .$$

Therefore, in practice, the integration limits which went into the determination of the total cross section were the same for all states in the projectile and the target.

The differential cross section expressions, $d\sigma_n^A/d\vartheta$ and $d\sigma_n^B/d\vartheta$, themselves were calculated from the expressions provided by Eq. 1.5 since

$$\frac{d\sigma}{d\vartheta} = 2\pi \sin \vartheta \frac{d\sigma}{d\Omega} . \quad (4.3)$$

Computational efficiency was improved by simplifying these calculations so that they were evaluated only for discrete values of ϑ , in steps of 0.1 mrad. Specifically, using the example of projectile excitations, for any given stepwise value of ϑ , the differential Coulomb cross section was calculated by

$$\frac{d\sigma_{n,\lambda}^A}{d\vartheta} = C(\lambda, n) B(E\lambda, 0 \rightarrow n) F(\vartheta, \xi(n), \lambda) , \quad (4.4)$$

where the quantity, F , defined through

$$F(\vartheta, \xi(n), \lambda) = \sin \vartheta \frac{df_{E\lambda}(\vartheta, \xi(n))}{d\Omega} , \quad (4.5)$$

had been tabulated beforehand using MATHEMATICA [36]. Explicit forms for the dif-

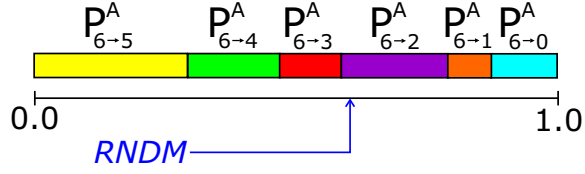


Figure 4.1: Schematic representation of the selection of a particular step in the decay sequence. A random number has been used to select the transition whereby the projectile goes from the 6th to the 2nd excited configurations. This process is repeated until the nucleus reaches the ground state.

ferential cross section functions, $df_{E\lambda}(\vartheta, \xi(n))/d\Omega$, appearing in Eq. 4.5 can be found in Appendix B. Meanwhile, direct comparison with, for example, Eq. 1.1 provides the definition for the multiplying factors:

$$C(\lambda, n) = 2\pi \left(\frac{Z_B \alpha}{\beta} \right)^2 a(n)^{-2\lambda+2} . \quad (4.6)$$

For target excitation, one need only replace Z_B with Z_A in the above expression.

4.1.2 Selection of the de-excitation path

The simulation included known or estimated γ -decay branching information for the contributing states in the projectile and the target. Specifically, for the selection of the decay from state n to a particular, less-energetic state m ($m < n$), a random number was first selected on the limit 0 to 1. This random number was compared against the branching probabilities from this excited configuration, denoted here for the projectile as $P_{n \rightarrow m}^A$, in a way that is schematically represented by Fig. 4.1. Of course, the branching probabilities themselves are defined such that

$$\sum_{m=0}^{n-1} P_{n \rightarrow m}^A = 1 ; \quad \sum_{m'=0}^{n'-1} P_{n' \rightarrow m'}^B = 1 .$$

This process was repeated at each intermediate decay step until the excited-nuclei's specific path back to its ground state was determined.

DO NOT MODIFY THE FORMAT OF THIS FILE!

```

***EXCITATION***
S# E_ex L dfEl dist. file B(EL)
(MeV) (18 chars) e^2*fm^(2L)
-----
1 1.98 2 o18_dfE2_1.98.data 4.65000E+01
2 3.92 2 o18_dfE2_3.92.data 2.00000E+01
3 4.46 1 o18_dfE1_4.46.data 4.00000E-06
4 5.10 3 o18_dfE3_5.10.data 1.12000E+03
5 5.25 2 o18_dfE2_5.25.data 2.98000E+01
6 6.20 1 o18_dfE1_6.20.data 1.90000E-03
-----
***DECAY/BRANCHING*** ORIGINAL ESTIMATES FROM REF: D.R. Tilley (NPA 1995)
C# S# E_ex to# Br. Prob.to# Br. Prob.to# Br. Prob.to# Br. Prob.to# Br. Prob.to# Br. Prob.
(MeV) (1=100%) (1=100%) (1=100%) (1=100%) (1=100%) (1=100%)
-----
1 0 0.00 0 0.000 0 0.000 0 0.000 0 0.000 0 0.000 0 0.000
2 1 1.98 1 1.000 0 0.000 0 0.000 0 0.000 0 0.000 0 0.000
3 0 3.55 2 1.000 0 0.000 0 0.000 0 0.000 0 0.000 0 0.000
4 0 3.63 2 0.997 1 0.003 0 0.000 0 0.000 0 0.000 0 0.000
5 2 3.92 2 0.876 1 0.124 0 0.000 0 0.000 0 0.000 0 0.000
6 3 4.46 4 0.704 2 0.271 5 0.025 0 0.000 0 0.000 0 0.000
7 4 5.10 2 0.761 5 0.176 3 0.063 0 0.000 0 0.000 0 0.000
8 5 5.25 2 0.559 1 0.303 5 0.087 6 0.030 3 0.011 4 0.010
9 0 5.34 2 0.580 6 0.420 0 0.000 0 0.000 0 0.000 0 0.000
10 6 6.20 1 0.887 6 0.041 8 0.036 4 0.025 9 0.011 0 0.000
-----
*ADDITIONAL COMMENTS MAY BE ADDED HERE*

```

Figure 4.2: Sample input file for the ^{18}O simulation which gives all relevant excitation and decay information for the projectile. A similar file serves as input to the code for target excitations.

The information which the simulation code used to select both the excitation channel and de-excitation path was incorporated into two input files, one containing information for the projectile, and the other giving target information. A sample input file is included in Fig. 4.2 which shows the ease with which necessary changes could be made to any excitation or de-excitation input field.

4.1.3 Projectile scattering

On an event-by-event basis, after selecting the excitation channel based on total excitation cross section information and the de-excitation cascade using γ -decay branching information, it was necessary to assign the projectile center-of-mass scattering angles, $\vartheta = \theta_{A',cm}$ and $\phi_{A',cm}$. Since the differential cross section expressions are independent of the azimuth, $\phi_{A',cm}$, this angle was chosen randomly over the range $(0 \rightarrow 2\pi)$. For the selection of ϑ , the so-called Monte Carlo rejection method was utilized, which

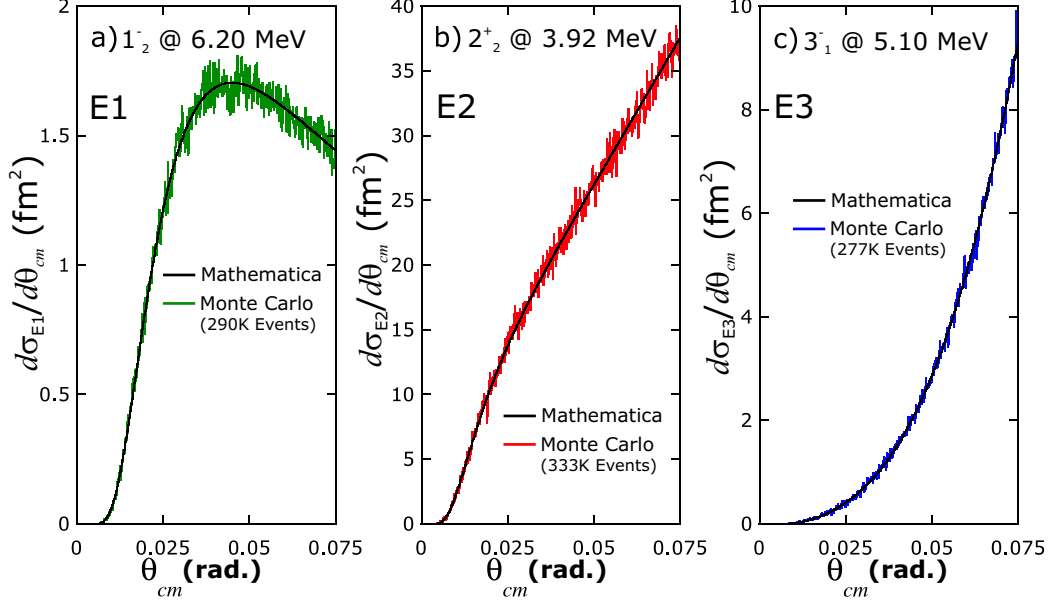


Figure 4.3: Comparison of normalized Monte Carlo-generated ^{18}O angular distribution with the corresponding differential cross section function, $d\sigma_{E\lambda}(\vartheta, \xi)/d\vartheta$, as generated using MATHEMATICA for the: a) 1_2^- state b) 2_2^+ state c) 3_1^- state.

involved a simple prescription. Two random numbers were chosen: The first represented the abscissa, x_{ran} , which falls somewhere in the domain, $x_{min} \leq x_{ran} \leq x_{max}$, over which the probability function being generated, $P(x)$ (in this case the differential cross section), was defined. The second random number y_{ran} took on values between 0 and y_{max} , where y_{max} is the maximum value of the probability function over its limits. A simple comparison of y_{ran} against $P(x_{ran})$ followed. The event, characterized by the physical observable x_{ran} , was *generated* if and only if $y_{ran} \leq P(x_{ran})$.

Possessing limited knowledge of the differential cross section for a given excitation channel, as it was tabulated only at discrete values of ϑ , it was necessary to use a cubic spline interpolation to evaluate, approximately, the cross section distributions for any random value of ϑ from 0 to $\vartheta_{n,max}^A \simeq \vartheta_{n',max}^B = \vartheta_{max}$. This interpolation method, by design, created approximate differential cross section functions within the intervals which were smooth in the first derivative and continuous in the second derivative. Details on the subject of spline interpolation formalism can be found in Ref. 25. Particular examples of generated angular distributions are shown in Fig. 4.3

for three particular states in ^{18}O . For comparison, the actual differential cross section functions generated with MATHEMATICA also appear in this figure.

Having determined the spherical scattering angles for the projectile in the center-of-mass, a straightforward application of equation Eq. A.15 allowed for a calculation of $\theta_{A',lab}$. Meanwhile, $\phi_{A',lab}$ was found with greater ease – because the azimuthal angle is determined by projectile motion which is transverse to the direction of the C.M. motion, it follows that

$$\phi_{A',cm} = \phi_{A',lab} .$$

4.1.4 γ -ray decay

Finding the lab-frame momenta for emitted γ -rays

For simplification, the assumption that the process of γ -ray decay was isotropic in the spherical emission angles θ_γ and ϕ_γ was adopted for both projectile and target de-excitations. (In reality, each γ -ray decay is associated with its own multipole-specific angular distribution – see, e.g., Ref. 1.) For each decay, this was facilitated using a set of random numbers, $0 \leq RAN_\gamma^{1,2} \leq 1$, such that

$$\phi_\gamma = 2 \pi RAN_\gamma^1 ; \quad \theta_\gamma = \arccos(2 RAN_\gamma^2 - 1) . \quad (4.7)$$

For the specific case of projectile γ -ray decay, an isotropic treatment demanded that these angles be chosen in the frame where the projectile was at rest. Justified by the assumption that the target was stationary, the emission angles for target decay, meanwhile, were measured directly in the laboratory coordinate system.

Because GEANT event-generation required knowledge of the momenta of the emitted γ -rays in the laboratory frame, target decay events needed no further analysis. However, the case of projectile decay was more complex since the emission occurred

from a moving frame. It was necessary to first relate the chosen emission angles in the projectile rest frame, $\theta_{\gamma,proj.}$ and $\phi_{\gamma,proj.}$, to the corresponding angles in the non-moving frame, $\theta'_{\gamma,lab}$ and $\phi'_{\gamma,lab}$. For θ this was accomplished using Eq. A.15 with the subscript substitutions, $A' \rightarrow \gamma$ and $cm \rightarrow proj.$, and using the fact, $\beta_{\gamma,proj.} = 1$, which allows

$$\tan(\theta'_{\gamma,lab}) = \frac{\sin(\theta_{\gamma,proj.})}{\gamma (\cos(\theta_{\gamma,proj.}) + \beta)}. \quad (4.8)$$

Meanwhile, the azimuthal relation is simply

$$\phi'_{\gamma,lab} = \phi_{\gamma,proj.}. \quad (4.9)$$

The remaining factor β (and γ) in Eq. 4.8 refers to the velocity of the outgoing projectile in the lab, $\beta_{A',lab}$, which can, for example, be calculated using an adapted form of the last expression given in Eq. A.14,

$$\gamma_{A',lab} = \gamma_{cm} \left[\beta_{cm} \cos(\theta_{A',cm}) \sqrt{\gamma_{A',cm}^2 - 1} + \gamma_{A',cm} \right], \quad (4.10)$$

along with

$$\beta_{A',lab} = \sqrt{1 - \gamma_{A',lab}^{-2}}.$$

In Eq. 4.10, β_{cm} refers to the velocity of the target+projectile C.M. frame in the laboratory, which is given by Eq. A.10. The relativistic factor appearing in Eq. 4.10, $\gamma_{A',cm}$, is calculated from knowledge of the excitation energy in both the projectile and target (See Eq. A.17).

The fact that the projectile itself moves in the laboratory with a momentum that is not oriented purely along the the beam (z) axis means that the γ -ray emission angles

given by Eqs. 4.8 and 4.9, $\theta'_{\gamma,lab}$ and $\phi'_{\gamma,lab}$, are not the same as the emission angles with respect to the lab axes, defined here as $\theta_{\gamma,lab}$ and $\phi_{\gamma,lab}$. A rotation, \mathbf{R} , which utilized knowledge of $\theta_{A',lab}$ and $\phi_{A',lab}$ was required to find the direction, $(\theta_{\gamma,lab}, \phi_{\gamma,lab})$.

$$\mathbf{R} = \Lambda_{z'}(\kappa)\Lambda_y(\alpha) ; \quad \alpha = 2\pi - \theta_{A',lab} ; \quad \kappa = 2\pi - \phi_{A',lab} . \quad (4.11)$$

Specifically, we have (e.g., Ref. 4)

$$\Lambda_y(\alpha) = \begin{pmatrix} \cos \alpha & 0 & -\sin \alpha \\ 0 & 1 & 0 \\ \sin \alpha & 0 & \cos \alpha \end{pmatrix} , \quad (4.12)$$

and

$$\Lambda_{z'}(\kappa) = \begin{pmatrix} \cos \kappa & \sin \kappa & 0 \\ -\sin \kappa & \cos \kappa & 0 \\ 0 & 0 & 1 \end{pmatrix} . \quad (4.13)$$

Hence,

$$\begin{pmatrix} x'' \\ y'' \\ z'' \end{pmatrix} = \mathbf{R} \begin{pmatrix} x \\ y \\ z \end{pmatrix} = \begin{pmatrix} \cos \kappa(x \cos \alpha - z \sin \alpha) + y \sin \kappa \\ -\sin \kappa(x \cos \alpha - z \sin \alpha) + y \cos \kappa \\ (x \sin \alpha + z \cos \alpha) \end{pmatrix} . \quad (4.14)$$

Above, the unprimed (Cartesian) unit vector refers to the (spherical) direction, $(\theta'_{\gamma,lab}, \phi'_{\gamma,lab})$, while the double-primed unit vector points in the desired direction, $(\theta_{\gamma,lab}, \phi_{\gamma,lab})$.

$\phi_{\gamma,lab}$). i.e.,

$$\begin{pmatrix} x \\ y \\ z \end{pmatrix} \rightarrow (\theta'_{\gamma,lab}, \phi'_{\gamma,lab}) ; \quad \begin{pmatrix} x'' \\ y'' \\ z'' \end{pmatrix} \rightarrow (\theta_{\gamma,lab}, \phi_{\gamma,lab}) .$$

Projectile recoil

As will be verified in a later discussion involving the simulation of S800 response (Sec. 4.2.1), the inclusion of projectile recoil was critical for the reproduction of certain aspects of the experimental results. For each decay, the projectile's laboratory-frame momentum was adjusted by the laboratory-frame momentum of the emitted γ -ray, $\vec{p}_{\gamma,lab}$, (found using the previously-described analysis) such that total momentum and energy was conserved during the process, e.g.,

$$\vec{p}'_{A',lab} = \vec{p}_{A',lab} - \vec{p}_{\gamma,lab} ; \quad m'_{A'} = m_{A'} - E_{\gamma}^* . \quad (4.15)$$

Above, E_{γ}^* is the excitation energy lost due to emission of the γ -ray. Neglecting a very small difference due to 4-momentum conservation, this excitation energy is equivalent to the energy of the γ -ray in the projectile rest frame, i.e.,

$$E_{\gamma,proj.} \simeq E_{\gamma}^* .$$

4.1.5 Simulating BaF₂ detector response

GEANT uses well-known information about γ -ray interactions in matter to determine energy deposition in *active* volumes, which, for this simulation, were hexagonal BaF₂ crystals. Using a hierarchal structure of volumes, both active and inactive (detector supports, beam-pipe structures, etc.), the pertinent geometrical setup was defined with GEANT's convenient initialization routines. For simplification, the center of the

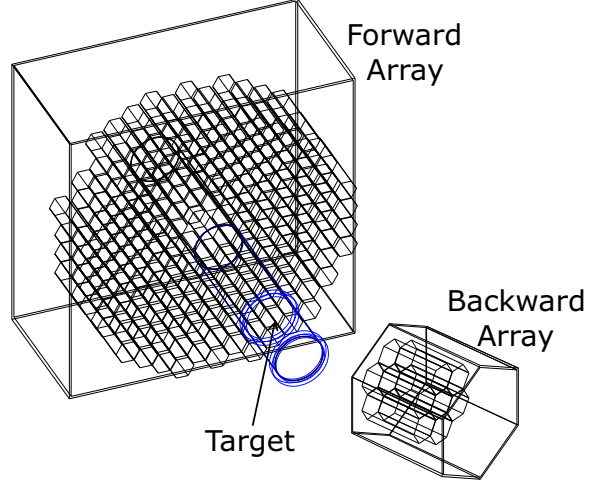


Figure 4.4: The geometrical setup of this experiment drawn using GEANT. It was sufficient to define only a portion of the existing support structures.

mother (laboratory) volume, in which all subordinate volumes were positioned, coincided exactly with the target position. Fig. 4.4 shows the geometrical setup for the simulation as drawn by GEANT. As can be seen in this figure, only a portion of the beam-pipe structures were actually included, as it was discovered that their presence had negligible effects on the simulated results. As an illustration of GEANT capabilities, simulated particle tracks are shown in Fig. 4.5 which have resulted from twenty ^{18}O nuclear excitations as seen upstream from the target (the backward array has been hidden).

Creating realistic energy signals

In order to emulate realistic BaF₂ detector response, it was necessary to fold the total energy deposition information which GEANT provided for each simulated detector, event by event, with the experimental BaF₂ resolution, characterized by (FWHM) width, Δ_{FWHM} , which has the approximate functional dependence:

$$\Delta_{\text{FWHM}}(E_{\text{dep.}}) \simeq E_{\text{dep.}} \left(A + \frac{B}{\sqrt{E_{\text{dep.}}}} \right). \quad (4.16)$$

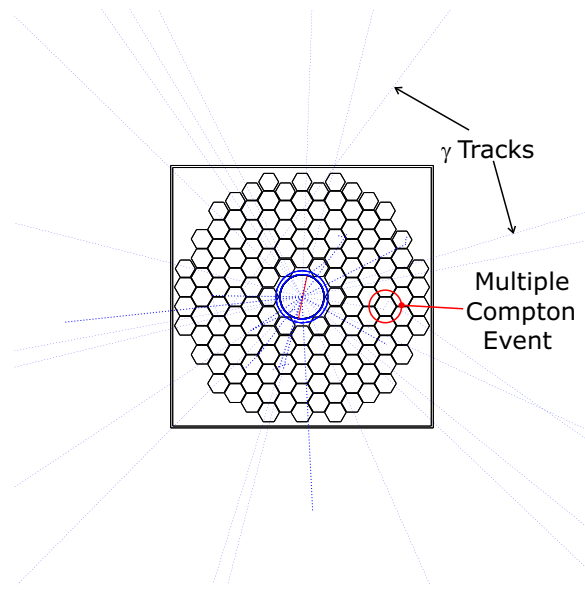


Figure 4.5: Sample events generated from twenty ^{18}O excitations as shown by the resulting particle trajectories. γ -ray tracks, for example, appear as dotted blue lines. Secondary processes have occurred.

Above, A and B are constants which were determined from a fit to experimental data. Fig. 4.6 shows such a fit for data points provided by sample ^{88}Y and the PuBe calibration sets. The Δ_{FWHM} information was obtained by fitting the photo-peaks from the calibration spectra which were generated by summing contributions from all detectors.

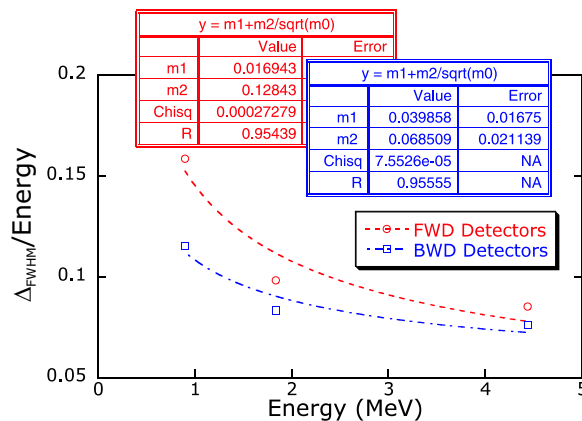


Figure 4.6: BaF_2 resolution fit for a determination of the constants in Eq. 4.16.

Application of energy thresholds

Another consideration for the simulation was the application of energy threshold constraints to simulated BaF₂ signals. As discussed in Sec. 2.2.3, only those events where at least one detector recorded a signal larger than T_h (the high threshold) were accepted by the acquisition. Additionally, for a given detector within an event, charge integration only occurred for signals larger than T_l , the low threshold. Including threshold effects into the simulation involved “setting” a unique set of threshold values for each detector, such that the average of these threshold values over all detectors were free parameters, $T_l^{\text{Ave.}}$ and $T_h^{\text{Ave.}}$, which were adjusted upon comparison with experimental data. The width of the distribution of low threshold values was also an adjustable parameter. The width of the T_h distribution, however, was scaled proportionately with the low threshold distribution, as the choice of the low threshold for a given detector, T_l^n , automatically determined its T_h^n setting. Specifically, it was assumed that for a given detector the two threshold cuts should be related by,

$$T_h^n = \left(\frac{T_h^{\text{Ave.}}}{T_l^{\text{Ave.}}} \right) T_l^n .$$

This relationship is justified by the fact that the fast-light response (or gain) is linear with incident γ -ray energy. Recall, it was the detector’s fast component which triggered the discriminators.

A comparison of simulated versus actual calibration data is presented in Fig 4.7 for ⁸⁸Y (a) and PuBe (b), which includes the summed contributions from individual detectors of the forward array. For both plots, the simulated data has been normalized to the area under the most energetic photo-peak of the actual data. The background included in the simulated data in all cases is linear. As was standard for recording all calibration data, the high threshold was set to the same value as the low threshold. Notice the discrepancy of the simulated data at low energies if threshold settings of

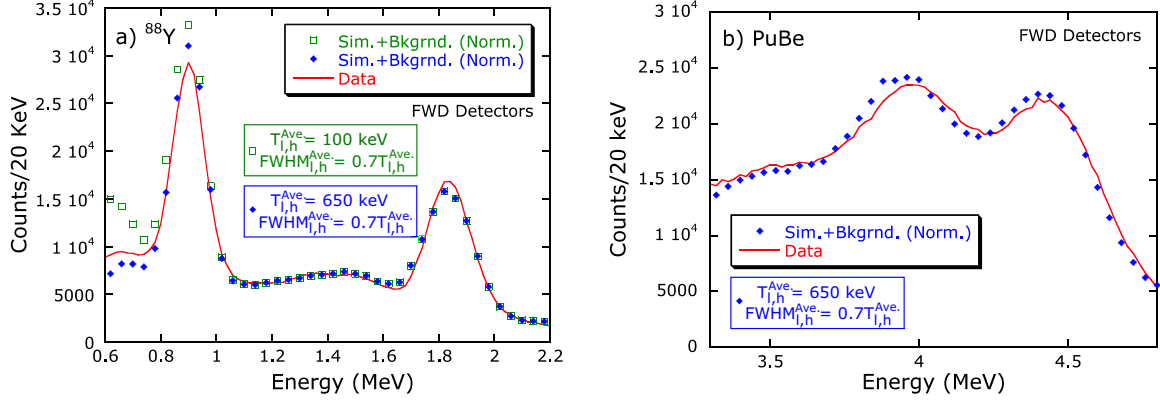


Figure 4.7: A comparison of simulated against actual calibration data for ^{88}Y (a) and PuBe (b). The background included with the simulated results is linear. a) The simulation using 100 keV threshold values is not consistent with experimental results at low energies. Better overall agreement is achieved using threshold settings of 650 keV.

100 keV are used. Much better agreement was achieved with average threshold values of 650 keV.

Preliminary comparisons of simulated results with experimental $^{18,20}\text{O}$ data revealed that the inclusion of an additional energy-smearing effect was necessary for reproduction of the BaF_2 response. This was especially true for the ^{18}O comparison. As was explained in Sec. 3.2.1, the analysis of the experimental BaF_2 data involved a *dynamic* energy calibration whereby the set of calibration coefficients used for a given detector depended on the run number for the data set being analyzed. The fact that photo-multiplier tube gains were drifting continuously throughout the experiment (due to temperature fluctuations, for example) rather than “jumping” abruptly from one calibration to the next effectively resulted in degradation of the experimental BaF_2 energy resolution when making comparisons of simulated against experimental data.

The importance of this effect could be established quantitatively for a subset of the detectors (which had sufficiently low T_h settings) by observing the position of the peak resulting from de-excitations from the first-excited 2^+ state. For ^{18}O data, this investigation showed that the energy calibration for the (subset of the) detectors

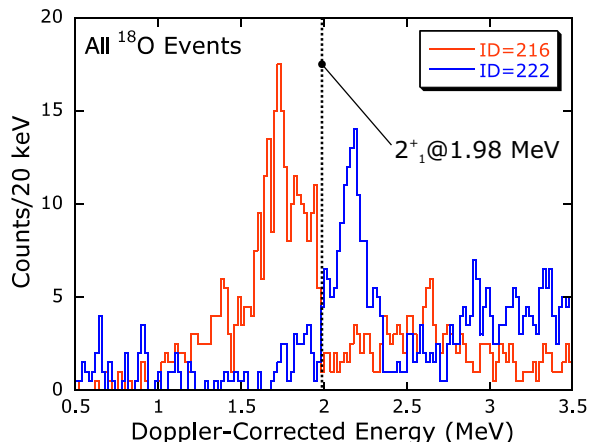


Figure 4.8: Doppler-corrected, ^{18}O BaF₂ energy spectra for two extreme examples of calibration drifting. The 2_1^+ peak is off by over 9% in both cases. A calibration correction was performed to remove this drifting in detectors which displayed this 2_1^+ peak. To account for the remaining detectors which could not be corrected, an additional energy-smearing factor was folded into the simulated BaF₂ response.

displayed an overall spread (σ) of $\sim 4.5\%$, while the same investigation for ^{20}O revealed a less dramatic drift of $\sim 1.5\%$. This difference is explained when one considers that only one BaF₂ energy calibration was performed at the end of the ^{18}O experiment while five subsequent energy calibrations were taken throughout the course of the ^{20}O experiment. It is not surprising that significant gain-drifting occurred during those first ~ 13 hours of the ^{18}O study.

Fig. 4.8 illustrates this calibration drifting for two particularly extreme ^{18}O cases. The proper position of the 2_1^+ peak is marked by the dotted black line. The calibration in both cases is off by over 9%. It was possible to improve the experimental BaF₂ response by adjusting the calibration coefficients for detectors which displayed this problem. However, given the fact that most detectors had high threshold settings which suppressed detection of γ -rays of this energy, these calibration corrections were performed for only $\sim 35\%$ and $\sim 44\%$ of the detectors for the ^{18}O and ^{20}O experiment, respectively. Hence, for the simulation it was assumed that the remaining detectors of the array behaved in a similar fashion as the subset which had been sampled and corrected.

4.1.6 Simulating S800 response

A simplified approach was taken to account for the S800 response within the simulation. Possessing experimental knowledge of relevant projectile observables at the target position, it was not necessary to *propagate* the simulated projectiles through the S800 using the direct map (as in the reconstruction formalism mentioned in Sec. 2.1.1). Working within a dispersive and non-dispersive fragment trajectory description, measured S800 resolution and acceptance limitations were therefore applied directly to the corresponding simulated projectile parameters.

S800+blocker acceptance

Inclusion of the blocker was essential for later comparisons with simulated results. Its introduction was facilitated by first applying an energy cut to simulated events. Specifically, only those projectiles which recorded an energy-loss, ΔE_A , which was greater than some cutoff, $E_{\text{Blckr.}}$, were accepted as events for further analysis, i.e.,

$$\Delta E_A = E_{A,\text{lab}} - E_{A',\text{lab}} \geq E_{\text{Blckr.}} \quad (4.17)$$

Because the blocker also affected the angular distributions (see Sec. 3.1.4), includ-

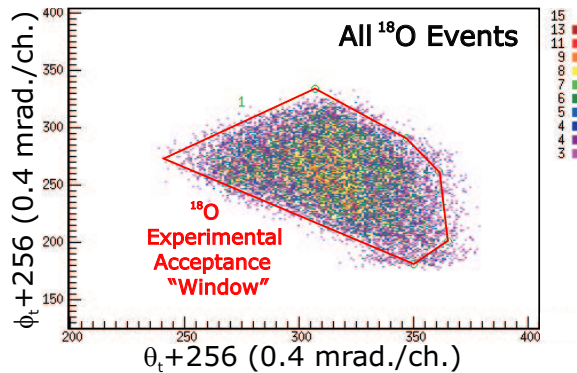


Figure 4.9: The observed acceptance “window” for ^{18}O , as shown in (θ_t, ϕ_t) space. The gate shown here was used to constrain simulated ^{18}O events, assuming 100% transmission for events falling inside.

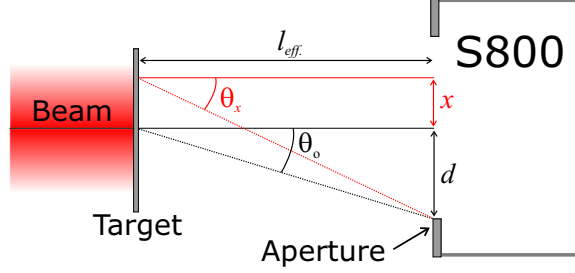


Figure 4.10: A simplified illustration which defines the parameters relevant to Eq. 4.18. For a projectile with a given interaction position, x , from the central axis of the S800, the angular acceptance is effectively changed from θ_o to θ_x . The difference between these two angles scales as x/l_{eff} , where l_{eff} is the effective distance from the target to the *aperture*.

ing only this energy constraint on the simulated data was inadequate. Reproduction of the observed angular distributions required that the acceptance of the entire apparatus (S800+blocker) be somehow included. Rather than attempt to understand and then incorporate each complicated facet of the acceptance (e.g., projectile scattering from the entrance slits and/or within the S800, blocker effects), the overall experimental acceptance for each study was, instead, *mapped* by drawing a free-form gate on a 2-D histogram of θ_t vs. ϕ_t data, as shown in Fig. 4.9. For the simulation, the assumption was made that projectile transmission for events meeting this simultaneous θ_t and ϕ_t criterion was 100%.

Assuming that the gate shown in Fig 4.9 defines a *pseudo* S800 entrance window or aperture, the experimental beam spot size was incorporated into the simulation by slightly perturbing the position of this acceptance window in θ_t and ϕ_t , event-by-event (while keeping its area constant). Fig. 4.10 shows (naively) the effect that finite spot size has on the S800 acceptance. The parameter which scales the importance of this perturbation is the effective distance from the target to the entrance aperture, l_{eff} , since

$$\theta_x \simeq \theta_o + \frac{x}{l_{eff}} . \quad (4.18)$$

Eq. 4.18 is derived directly from the relation,

$$\tan \theta_x = \frac{x + d}{l_{eff.}} \simeq \theta_x ,$$

along with,

$$\tan \theta_o = \frac{d}{l_{eff.}} \simeq \theta_o ,$$

where the small angle approximation has been utilized. The beam spot size, ~ 5 mm FWHM, was estimated by observing ^{18}O and ^{20}O y_t distributions for elastic scattering runs. Assuming an effective target to aperture length of approximately 300 cm, the acceptance perturbation is on the order of 2 mrad. In reality the geometry of the so-called acceptance window was also dependent on projectile kinetic energy, as the refocusing of the projectiles onto the blocker was not completely successful (see Sec.3.1.4). However, given the small energy-loss for projectiles in this study, it was sufficient to assume that only the projectile's position at the target modified the S800 acceptance event-by-event.

Energy resolution

The energy spreading for experimentally observed projectiles was the result of three contributing factors, namely, intrinsic dispersion in the beam, energy straggling in the ^{208}Pb target, and finite resolving power of the focal plane detectors. For the simulation, it was adequate to assume that the incoming projectiles were mono-energetic and then account for these energy-smearing effects by modifying the outgoing projectile energies accordingly. To quantify the spreading experimentally, the elastically scattered (beam) energy distribution was analyzed, as shown in Fig 4.11. As expected, due to a greater intrinsic energy spread of incoming beam particles, the distribution for ^{20}O had a larger width (σ) than that for ^{18}O .

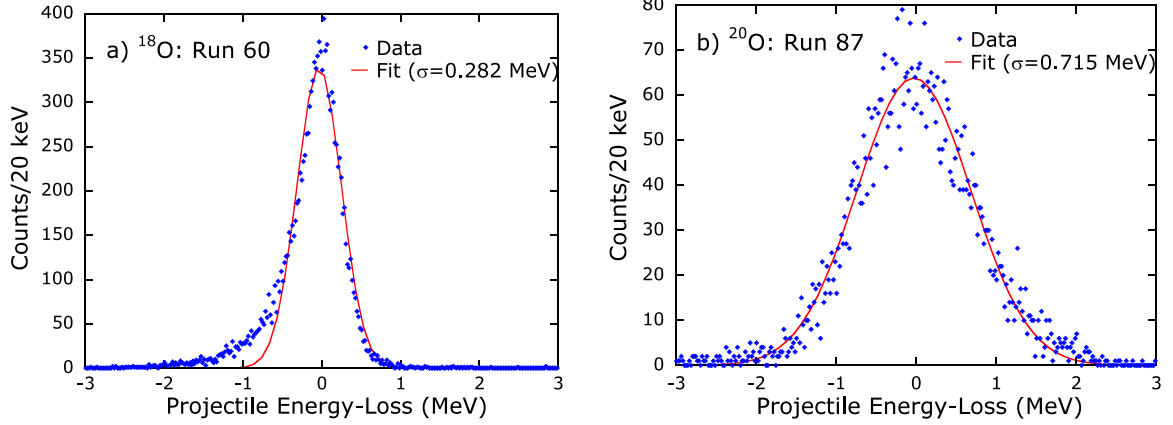


Figure 4.11: Elastically scattered beam (blocker out) energy distribution for ^{18}O (a) and ^{20}O (b) projectiles as measured by the S800. Intrinsic energy dispersion, target straggling, and finite detector resolution all contribute to the spreading which is observed. ^{20}O , as expected, has a wider intrinsic energy spread than primary beam, ^{18}O .

Angular resolution

The final angular distributions for projectiles were similarly affected by intrinsic momentum dispersion, angular straggling in the target, and CRDC resolution. To realistically incorporate these factors into the simulation, an angular spread ($\sigma_{\theta,in}$, $\sigma_{\phi,in}$) which was consistent experimentally with combined contributions from the intrinsic beam spread and angular straggling in the target was included for incoming projectiles. Spreading due to finite detector resolution, labeled $\sigma_{\theta,res}$ and $\sigma_{\phi,res}$ for the dispersive and non-dispersive angles, was used to modify outgoing projectile distributions.

The determination of the spreading widths $\sigma_{\theta,in}$ and $\sigma_{\phi,in}$, like the determination of the energy spreading width (Fig 4.11) involved observing the elastic dispersive and non-dispersive, target-position angular distributions. Unfortunately, folded into these elastic distributions was the spreading width due to CRDC detectors themselves:

$$\sigma_{\theta,el} = \sqrt{\sigma_{\theta,in}^2 + \sigma_{\theta,res}^2} ; \quad \sigma_{\phi,el} = \sqrt{\sigma_{\phi,in}^2 + \sigma_{\phi,res}^2} . \quad (4.19)$$

Fortunately, the two contributions to elastic spreading could be separately determined by making use of target-out mask calibrations.

For the dispersive direction, we have

$$\sigma_{\theta, res} \simeq \sqrt{\left(\frac{d\theta}{dx_1}\sigma_{x_1}\right)^2 + \left(\frac{d\theta}{dx_2}\sigma_{x_2}\right)^2}, \quad (4.20)$$

where x_1 and x_2 are the dispersive coordinates as measured in CRDC1 and CRDC2. The scaling factors in Eq. 4.20, $d\theta/dx_1$ and $d\theta/dx_2$, are found directly from the expression which determines the scattering angle:

$$\theta = \arctan\left(\frac{x_2 - x_1}{l}\right), \quad (4.21)$$

where l is the distance between the CRDC detectors, or 1073 mm. Therefore,

$$\frac{d\theta}{dx_2} = -\frac{d\theta}{dx_1} = [l(1 + \tan^2 \theta)]^{-1} \simeq [l(1 + \theta^2)]^{-1}, \quad (4.22)$$

where the small angle approximation has been used in the last step. The analysis was simplified by assuming that CRDC1 and CRDC2 have similar resolving power, i.e.,

$$\sigma_{x_1} \simeq \sigma_{x_2}$$

Hence,

$$\sigma_{\theta, res}(\theta = 0) \simeq \frac{\sqrt{2}\sigma_{x_1}}{l} \quad (4.23)$$

The uncertainty in the dispersive position, σ_{x_1} , was itself determined from the experimental mask calibration. Specifically, a gate was placed on the central portion of CRDC2 to select straight-line fragment trajectories through CRDC1, over which the mask had been placed. The observed spot size (of width σ_{mask, x_1}) in the resulting

CRDC1 position spectrum was the result of intrinsic detector resolution folded with the size of the aperture (σ_{hole}). Hence,

$$\sigma_{mask,x_1} = \sqrt{\sigma_{x_1}^2 + \sigma_{hole}^2} , \quad (4.24)$$

which, rewritten, becomes

$$\sigma_{x_1}^2 = \sigma_{mask,x_1}^2 - \sigma_{hole}^2 . \quad (4.25)$$

Realistically, the contribution from the hole is that of a step function which spans the hole-diameter, Δx ($\Delta x = 1.57$ mm). Comparing a Gaussian to a step function of the same area, it can be found that the width, σ_{hole} , is related to the hole diameter by

$$\sigma_{hole} \simeq 0.39\Delta x .$$

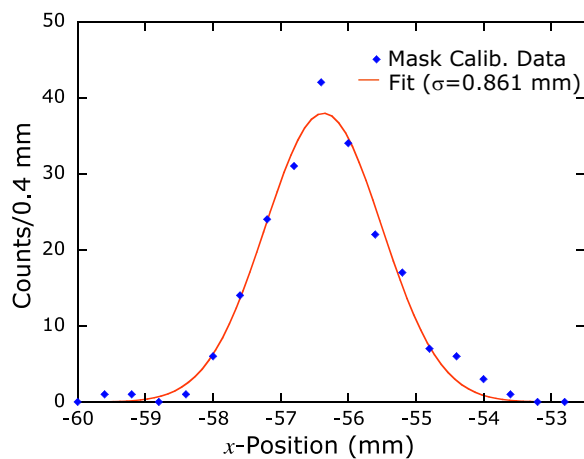


Figure 4.12: Sample data from the CRDC1 mask calibration which has been gated on the central region of CRDC2 to select straight-line trajectories. The fit for this particular mask hole gives $\sigma_{mask,x_1} = 0.861$ mm.

Thus, Eq. 4.25 simplifies to

$$\sigma_{x_1}^2 \simeq \sigma_{mask,x_1}^2 - (0.39\Delta x)^2. \quad (4.26)$$

Fig. 4.12 shows an example of the fitting process using data from the CRDC1 mask calibration. The plot shown has been expanded about a peak which results from one of the 1.57 mm holes in the mask. Several of these peak widths were averaged to find that $\sigma_{mask,x_1} = 0.83$ mm. Inserting this result into Eq. 4.26 gives the experimental dispersive position resolution, $\sigma_{x_1} \simeq \sigma_{x_2} = 0.56$ mm, which is consistent with the designed value for these detectors. The corresponding dispersive angular resolution of the S800, $\sigma_{\theta,res}$ (given by Eq. 4.23), was therefore $\simeq 0.74$ mrad.

Exactly the same formalism can be applied for finding the non-dispersive width, $\sigma_{\phi,res}$. A more simplified approach, however, which was sufficient for the simulation, came from comparing the average width from the dispersive mask calibration (e.g., Fig. 4.12) with that from the non-dispersive mask calibration; the resolution of the S800 in the non-dispersive direction was found directly from a simple scaling argument:

$$\sigma_{y_1} \simeq \left(\frac{\sigma_{mask,y_1}}{\sigma_{mask,x_1}} \right) \sigma_{x_1}.$$

From the non-dispersive CRDC1 calibration, it was determined that $\sigma_{mask,y_1} = 0.47$ mm. From the expression above, again assuming that the resolving power of the CRDCs was roughly equivalent, we have $\sigma_{y_1} \simeq \sigma_{y_2} \simeq 0.32$ mm. Hence, the experimental uncertainty in the non-dispersive angular determination, $\sigma_{\phi,res}$, was $\simeq 0.42$ mrad.

Fig 4.13 shows dispersive and non-dispersive scattering angle distributions from elastically scattered beam projectiles for both studies. A Gaussian fit to these distributions gave the widths, $\sigma_{\theta,el}$ and $\sigma_{\phi,el}$. Use of Eq. 4.19, possessing knowledge of $\sigma_{\theta,res}$ and $\sigma_{\phi,res}$, allowed for the determination of the incoming beam angular spreads, $\sigma_{\theta,in}$

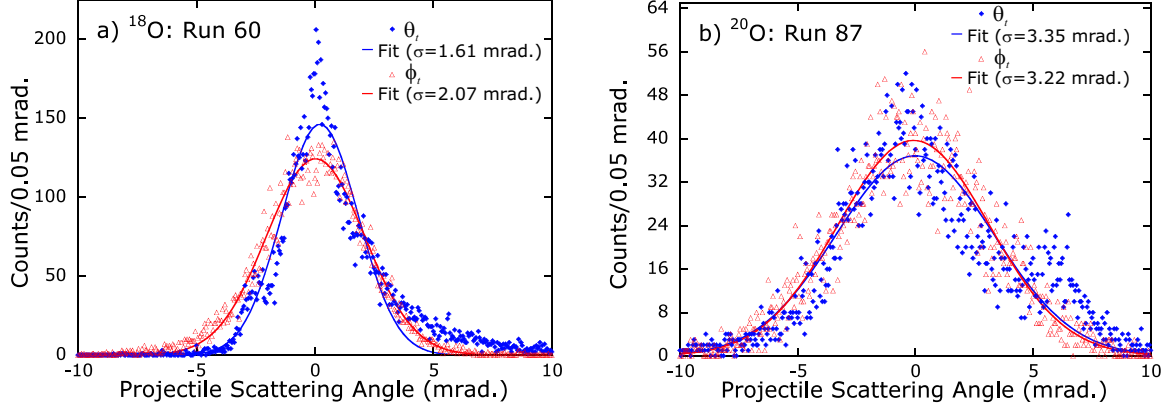


Figure 4.13: Angular distributions for elastically scattered (blocker out) ^{18}O (a) and ^{20}O (b) projectiles as measured by the S800. The fits give the widths, $\sigma_{\theta,el}$ and $\sigma_{\phi,el}$, which can be used in Eq. 4.19 to determine $\sigma_{\theta,in}$ and $\sigma_{\phi,in}$.

Table 4.1: Angular widths used to modify the incoming and outgoing projectile distributions in the simulation. All values are in mrad.

Beam	$\sigma_{\theta,in}$	$\sigma_{\phi,in}$	$\sigma_{\theta,res}$	$\sigma_{\phi,res}$
^{18}O	1.43	2.03	0.74	0.42
^{20}O	3.27	3.19	0.74	0.42

and $\sigma_{\phi,in}$, which were used to modify the incoming projectile angles in the simulation.

Table 4.1 summarizes the pertinent angular information which was utilized for the simulation.

4.1.7 Limitations of the simulation and related comments

The limitations of the simulation come not from its inherent design, but are instead attributed to an experimental limitation. It was not possible to incorporate raw experimental cross section (and therefore $B(E\lambda)$) information for discrete transitions into the simulation. Obviously critical for these cross section determinations is a quantitative comparison of the appropriate experimental γ -ray yield to the total number of incoming projectiles. Unfortunately, for these studies, no incoming beam monitor existed. A beam rate estimate based on the S800 singles rate, for example, was not possible due to the presence of the beam blocker. For the ^{20}O study, the capability for

beam rate monitoring would have existed had it not been for the efficiency instability of the multi-channel plate timing detectors (recall the discussion in Sec. 3.3).

As the reader can verify from a review of, for example, Eq. 4.4, it is the $B(E\lambda)$ value for a particular discrete excitation which ultimately determines the excitation probability for this state within the simulation. For the case of ^{18}O , the simulation was constrained in the sense that all pertinent $B(E\lambda)$ information has been previously measured. Therefore, essentially two free parameters were left for ^{18}O simulations, namely the average high-threshold (T_h) setting and the blocker positioning. (The average low-threshold setting, T_l , had been approximately established from the simulations of γ -ray source data presented earlier.) The best achievable strength function agreement was found by first adjusting only these two simulation fields. Because the overall normalization of the simulated ^{18}O strength curve was fairly well established by the collection of known $B(E\lambda)$ information, it was expected that slightly adjusted $B(E\lambda)$ and branching information could be extracted from subsequent simulations which had attempted to improve the overall strength function agreement.

The situation was rather different for the case of ^{20}O . As has been mentioned, only the $B(E2)$ strength for its first excited state has been measured. Because this state is found at 1.67 MeV (~ 2.5 MeV in the lab), contributions from this state were dramatically affected by both blocker positioning and the average T_h setting. In this sense, the overall simulated strength function normalization was inherently more ambiguous. However, as will become more evident in Sec. 4.3.3, it was the target *background* which facilitated the extraction of $B(E\lambda)$ information from the ^{20}O experimental results. Specifically, contributions from the target 2_1^+ level, being unaffected by blocker positioning, and much less affected by the high-threshold setting than the 2_1^+ state in ^{20}O , provided the overall normalization, effectively constraining the $B(E\lambda)$ strengths for higher-lying projectile levels.

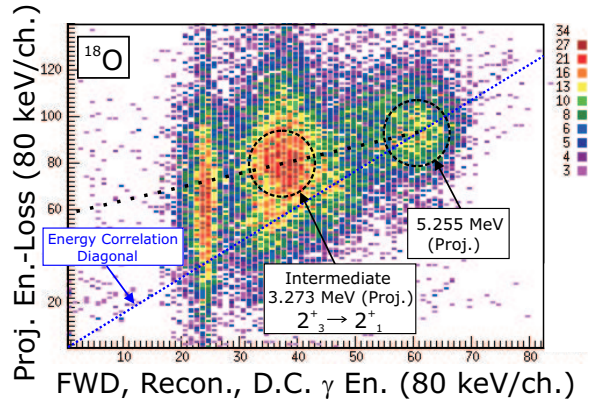


Figure 4.14: A plot of projectile energy-loss vs. total, forward, reconstructed, Doppler-corrected γ -ray energy for ^{18}O . Notice the pronounced *off-diagonal* enhancement which appears at a γ -ray energy of ~ 3.2 MeV.

4.2 ^{18}O results

4.2.1 Projectile energy-loss vs. total γ -ray energy

The simulation proved to be an invaluable asset with regard to understanding the more elusive aspects of the experimental results. Especially complicated, for example, were the 2-D histograms generated by plotting a projectile's energy loss against the total reconstructed, Doppler-corrected (or lab-frame) γ -ray energy captured simultaneously in the forward BaF_2 array. Such a plot with ^{18}O experimental results is shown in Fig. 4.14. As explained earlier in Sec. 3.4.2 the pronounced diagonal enhancement appearing in this figure results from events whereby the projectile's excitation energy has been recovered as γ -ray radiation in the forward array. (For this particular example, the diagonal enhancement has a slope which is greater than one since Doppler-corrected energy, not lab-frame energy, is plotted on the x -axis.) Anything falling below and to the right of this *diagonal* is energetically forbidden, while events above and to the left result from multi-step γ -decays in which one (or more) of the γ -rays was not detected. This correct interpretation opened more challenging questions, though; the physics which is manifested in the sub-structure observed in Fig. 4.14 is less trivial.

For example, notice the pronounced *off-diagonal* enhancement which is highlighted in Fig. 4.14. Projected onto the Doppler-corrected, γ -ray energy axis, these events are found near 3.2 MeV. One could deduce from the large relative cross section for transitions to the 5.255 MeV (see Sec. 1.3) along with the strong decay branch from this state through the first-excited state at 1.98 MeV ($\sim 56\%$) that one should see an abundance of γ -rays at ~ 3.2 MeV. What was not expected a priori, however, was the fact that this enhancement was not characterized by the same projectile energy-loss as those events which recorded a total γ -ray energy of ~ 5.2 MeV. Resolution to this apparent contradiction, which was first revealed by the simulation, comes after considering the systematic bias introduced by the γ -ray detection setup. Because of its solid angle coverage, the forward BaF₂ array was relatively less efficient in its ability to detect γ -rays which had been emitted at backward angles in the projectile rest-frame; for these events, the projectile receives an energetic “kick” from its recoil against the γ -ray. Specifically, the (*off-diagonal*) enhancement found at a γ -ray energy of ~ 3.2 MeV was correlated with a smaller projectile-energy loss than the (*on-diagonal*) structure at ~ 5.2 MeV because it resulted from a missing 1.98 MeV γ -ray – all else being equal, the array had a detection deficiency for projectiles receiving an energetic (positive- z) boost from that missing γ -ray.

Fig. 4.15, which plots the same quantities shown in Fig. 4.14, strategically illustrates an evolution in the simulation’s level of sophistication. For simplification, the blocker has not been incorporated. Fig. 4.15a has been generated without including projectile- γ -ray recoil. Furthermore, perfect detector resolving power has been assumed. Notice the horizontal lines which result from excitations to each particular level in ¹⁸O that have been highlighted by orange dotted lines. Sub-structures observed within these horizontal enhancements result from multi-step decay events for which at least one γ -ray has eluded detection. Enhancements resulting from the two contributing target states are also shown – an indication that the physics is simply

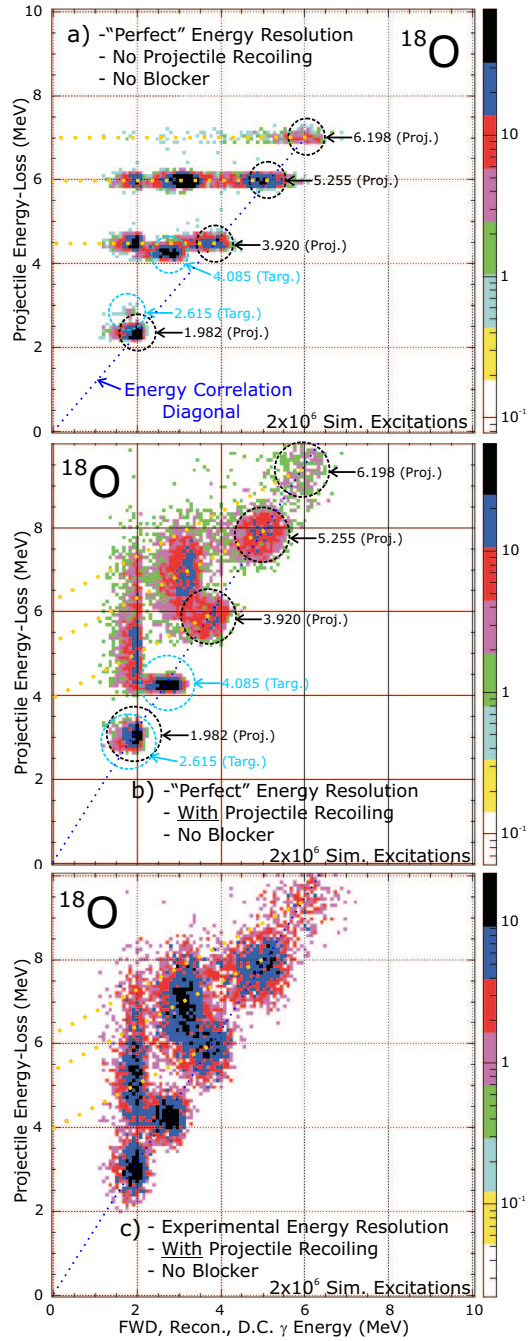


Figure 4.15: An evolution plot of projectile energy-loss vs. total reconstructed, Doppler-corrected γ -ray energy for simulated ^{18}O data, generated with an increasing level of sophistication. a) The recoil of the projectile from the emitted γ -rays has been neglected. Ideal detector resolution has also been assumed for both the S800 and the BaF₂ arrays. b) Projectile recoil has been included. c) Projectile recoil and experimental detector resolution have been included. The blocker has been placed at 0.0 MeV projectile energy-loss in all cases.

wrong for this case is that the target states do not fall on the energy correlation diagonal, shown as the dotted blue line. Fig. 4.15b shows the equivalent histogram generated after the inclusion of projectile recoil from emitted γ -rays into the simulation. A *diagonalization* of the multi-step decay lines is observed when comparing Fig. 4.15b with Fig. 4.15a. Additionally, the slope of the energy correlation diagonal is seen to increase, and it now properly encompasses the target states. Fig. 4.15c incorporates the experimental detector resolution for both the S800 and the BaF₂ detectors.

Direct comparison of Fig. 4.15c with the experimental equivalent (Fig. 4.14) provides confidence, though an S800 energy resolution discrepancy remains. Specifically, the experimental S800 projectile energy-loss measurement is plagued with significantly poorer resolution than that of the simulation. It is assumed that this observed difference is a manifestation of the S800 reconstruction process. This is logically justified by the fact that the simulation, by construction, has included no additional smearing due to trajectory reconstruction; any discrepancy observed *must* therefore

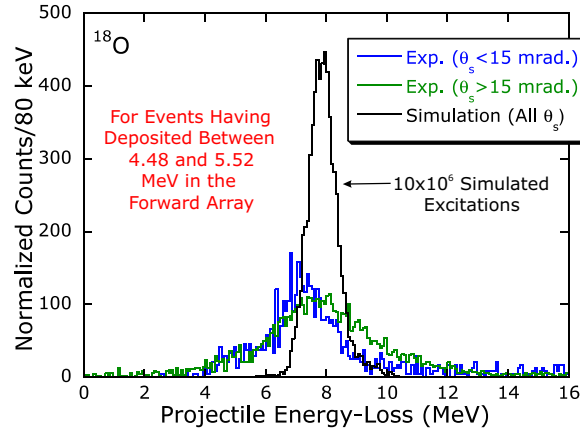


Figure 4.16: Projectile energy-loss for ^{18}O events in which the forward array has recorded between 4.48 and 5.52 MeV, which selects essentially only excitations of the 2_3^+ . The experimental data has been subdivided with a constraint on the projectile's spherical scattering angle, Θ_s . Note that the experimental S800 energy resolution is worse for larger scattering angles. The simulation, shown in black, includes no smearing effects due to the reconstruction process, causing the resolution discrepancy observed here.

be attributed to this process.

For the present discussion it is constructive to examine Fig. 4.16, which shows experimentally-measured projectile energy-loss distributions gated on (spherical) scattering angle, Θ_s , for events having deposited between 4.48 and 5.52 MeV (Doppler-corrected) in the forward array. This energy constraint essentially selects only those events whereby the 5.25 MeV projectile state has been excited. Also included in this figure is the simulated result, which, by comparison, reveals that the projectile energy resolution discrepancy is more dramatic for larger projectile scattering angles. Due to imperfections in the magnetic field mapping, the S800 reconstruction precision is known to suffer for more-extreme projectile trajectories [7]. In principle the experimental energy resolution could be modestly improved by performing the S800 reconstruction calculations to higher order (>2). Still, with the current study, obtaining higher-precision S800 energy measurements would in no way improve the experimental results, as they are derived from complimentary BaF₂ information.

4.2.2 ¹⁸O strength distributions

Shown in Fig. 4.17a is the final experimental ¹⁸O strength distribution (red data points) along with simulated data (black solid line) which was generated using known $B(E\lambda)$ and branching information as input [22,31,35]. The experimental results have been normalized to the simulated data in the region where the target 4.085 MeV state is the dominant contribution (between 2.5 and 2.9 MeV). The simulation reproduces the experimental data reasonably well, though there exist discrepancies which seem to be tied to excitations to the third-excited 2⁺ state at 5.255 MeV. For example, a small decrease in the $B(E2) \uparrow$ value for the 5.255 MeV combined with an increase in the branching ratio from this state to the first-excited 2⁺ configuration at 1.982 MeV will improve the comparison. For additional improvement, the $B(E2) \uparrow$ to the second-excited 2⁺ at 3.920 MeV might also be increased. Fig. 4.17b shows the individual

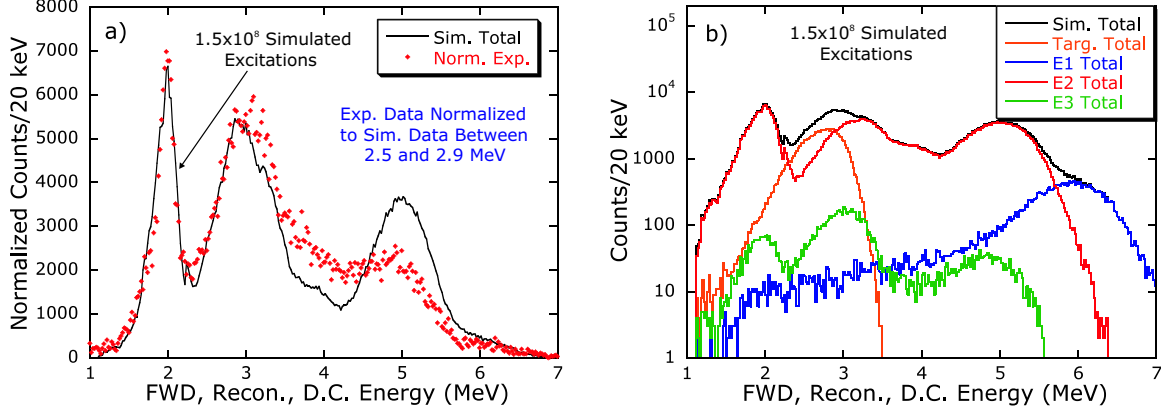


Figure 4.17: a) Final experimental ^{18}O strength distribution (data points) shown with simulated data (solid line) generated using known $B(E\lambda)$ and branching information as input [22, 31, 35]. The experimental data has been normalized to the simulated results in the region where target contributions dominate (between 2.5 and 2.9 MeV). b) The individual components which contribute to the total simulated strength distribution. Notice that $E2$ excitations completely dominate over the other multipolarities. The target background is significant.

components which contribute to the total simulated strength distribution. This histogram demonstrates the fact that $E2$ excitations completely dominate the excitation function for ^{18}O in this energy region. The target background is clearly not a negligible component. As an illustration of the capabilities of the simulation, in light of the above discussion regarding better agreement with experimental data, Fig. 4.18a shows a simulated ^{18}O strength distribution generated using slightly adjusted $B(E\lambda)$ and branching information as input. Fig. 4.19 outlines the specific changes that were made to previously established quantities. While better agreement in the targeted regions has been established, a discrepancy at γ -ray energies of ~ 4.3 MeV lingers. An adjustment which would *fill-in* the simulated spectrum in this energy region involves, for example, increasing the $B(E1) \uparrow$ value for the first-excited 1^- state at 4.456 MeV by approximately three orders of magnitude above the upper limit established in Ref. 22 (see Fig. 1.2). Alternatively, one could introduce a previously unobserved [35] decay branch from the second-excited 1^- state at 6.198 MeV to the first-excited 2^+ state at 1.982 MeV. Unfortunately, due to the ambiguities that are associated with the simu-

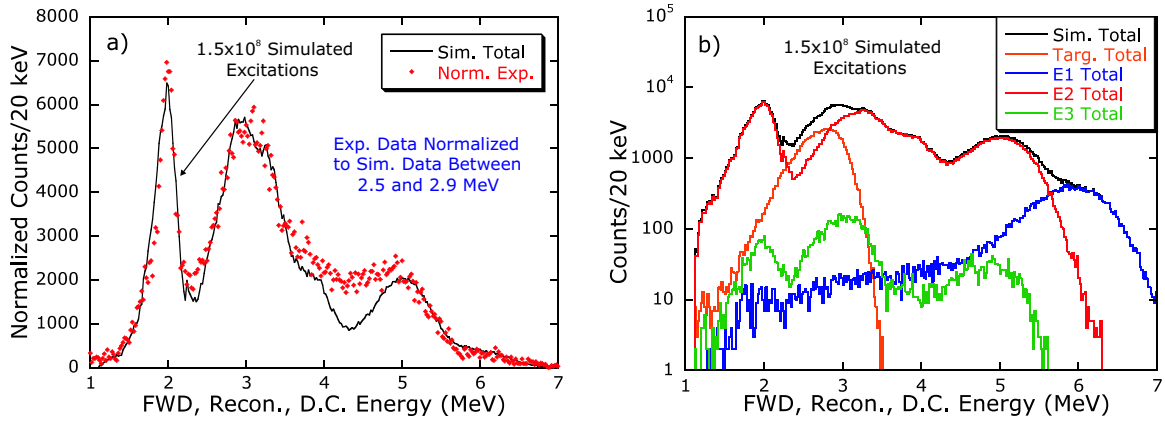


Figure 4.18: a) Final experimental ^{18}O strength distribution (data points) shown with simulated data (solid line) generated using slightly adjusted $B(E\lambda)$ and branching information as input (see Fig. 4.19). As with the previous comparison, the experimental data has been normalized to the simulated results in the region where target contributions dominate. An improvement in overall agreement between simulated and experimental data is obtained. b) The individual components which contribute to the total simulated strength distribution.

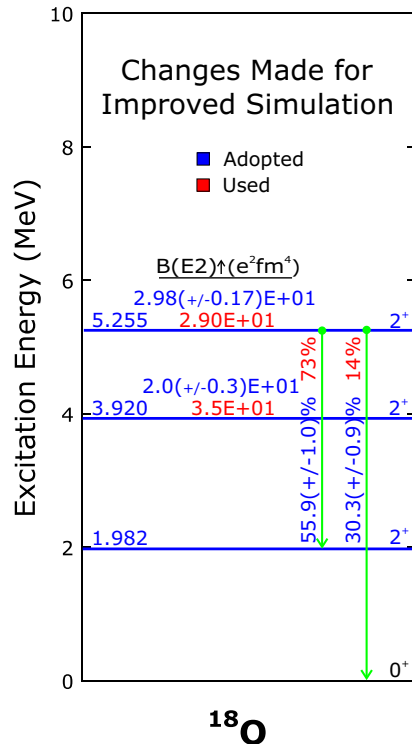


Figure 4.19: The specific changes that were made to previously established ^{18}O experimental quantities in generating Fig. 4.18. Known values are given in dark blue while changed values appear in red.

lated blocker position and high-threshold setting, no recommendations regarding the accuracy or status of ^{18}O information can be confidently offered. What is important to take from these comparisons is the fact that every feature of the experimental ^{18}O strength distributions has been reproduced, i.e., all the individual components have been accounted for.

4.2.3 Angular distributions

The ^{18}O dispersive (θ_t) and non-dispersive (ϕ_t) angular distributions obtained from the “improved” version of the simulation (Fig. 4.18) are displayed as the solid lines in Fig. 4.20 along with the final experimental distributions which appear as the data points. While the agreement observed in this comparison is less than ideal due to the complex nature of the S800 acceptance, further inspection reveals that exact acceptance reproduction is unimportant insofar as the results of this comparative analysis are concerned. Indeed, Fig. 4.21 shows a simulated ^{18}O strength distribution which was obtained after increasing the area of the acceptance “window” in (θ_t , ϕ_t) (see Sec. 4.1.6) by a factor of 2. Also included in this figure, for comparison, are the simulated results from Fig. 4.18. The data, as before, has been normalized to the

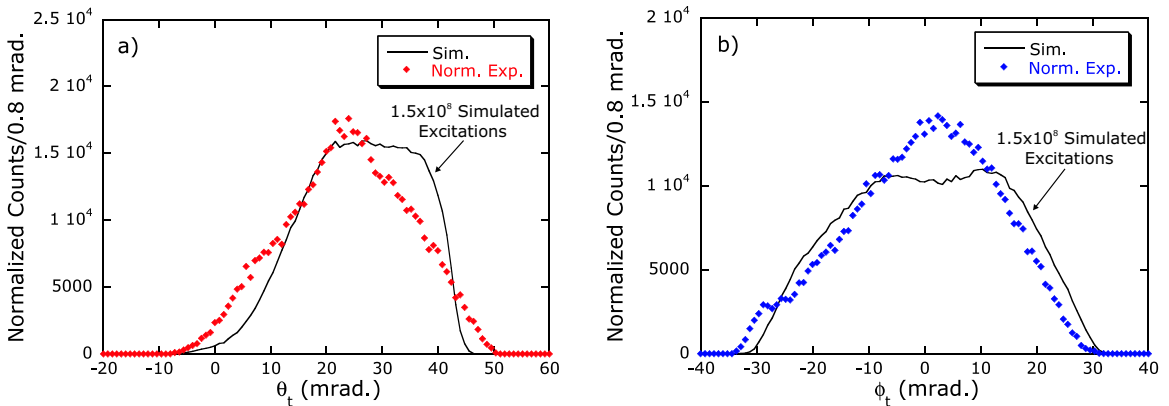


Figure 4.20: The final ^{18}O θ_t (a) and ϕ_t (b) experimental angular distributions (data points) shown against the results obtained from the “improved” simulation (solid lines). The experimental data has been normalized to the simulated results. Due to the complexity of the S800 acceptance, the agreement observed is less than ideal.

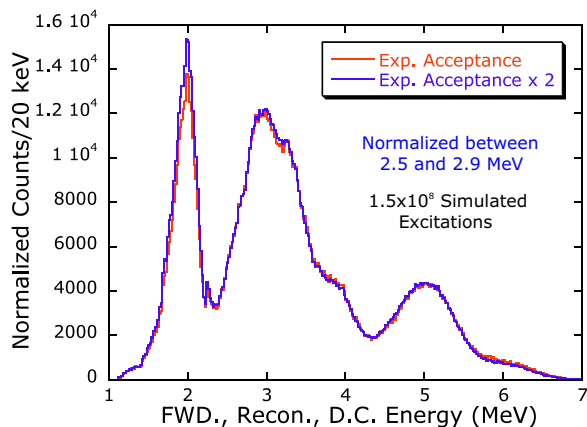


Figure 4.21: A comparison of the simulated ^{18}O strength function from Fig. 4.18 with that obtained after increasing the area of the acceptance “window” by a factor of two. The former data set has been normalized to the newer in the region between 2.5 and 2.9 MeV. Notice that only slight differences can be seen.

region between 2.5 and 2.9 MeV. Notice that only a small change is perceivable in the overall strength distribution.

4.3 Extension to ^{20}O

4.3.1 Initial interpretations

Recall the ^{20}O experimental strength distribution presented in Chapter 3, which displayed two broad peaks between 5 and 7 MeV. The enhancements which are responsible for these peaks are highlighted in Fig. 4.22, which is a familiar plot of projectile energy-loss against total γ -ray energy. We interpret these structures as resulting from $E1$ projectile excitations. Specifically, two ^{20}O 1^- states are observed at ~ 5.2 and ~ 6.7 MeV. The fact that these structures fall directly on the energy correlation diagonal is irrefutable evidence that these configurations were excited directly. Indeed, the interpretation that these excitations are 1^- states is the only conclusion which is consistent with the theoretical shell model predictions. For instance, virtual excitation of the known 2^+ state at 5.234 MeV (see Fig. 1.4) with a strength that is consistent

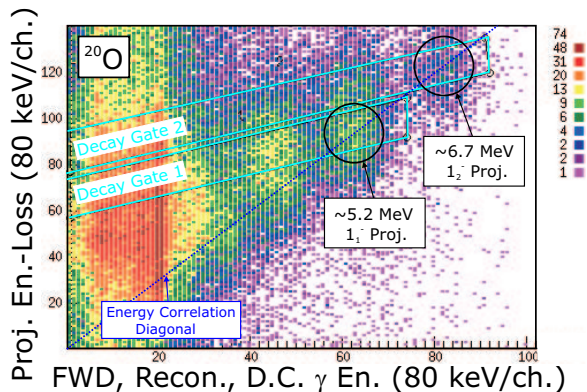


Figure 4.22: Projectile energy-loss vs. total, forward, reconstructed, Doppler-corrected γ -ray energy for ^{20}O . Two projectile states at 5.2 and 6.7 MeV are observed. Gates which have been drawn along the multi-step decay paths are highlighted.

with the results of this study would require that the predicted $B(E2)$ be over four orders of magnitude too low. The same logic applies to excitations of the (tentatively assigned) 3^- state at 5.614 MeV; in this case the theoretical $B(E3)$ would have to be increased by roughly two orders of magnitude.

4.3.2 γ -decay branching estimates

As discussed in Chapter 1, with the exception of decays from the second-excited 2^+ state, no γ -decay branching has previously been established. It was entirely useful, therefore, to extract any of this information which was warranted by the current results. This goal established, first approximations for γ -decay branchings were taken from complementary information in ^{18}O and/or from mean lifetime (τ) estimates based on theoretical $B(E\lambda)$ information. This information was then scrutinized against any experimental evidence which was available.

The current discussion will, of course, benefit from particular examples. In light of the interpretations in the previous section, of particular interest for the analysis was decay information for these new 1^- states. An investigation of analogous levels in ^{18}O reveals that the 1_1^- state decays via two significant channels, namely the 2_1^+ state ($\sim 30\%$) and the 0_1^+ state ($\sim 70\%$), while the 1_2^- state decays with high probability

(~90%) directly to the ground state [35] – i.e., decays which proceed via the emission of $E1$ photons dominate, as expected. For the extension to the unknown case ^{20}O , mean lifetime calculations, assuming pure $E1$ decay for these 1^- states, performed using theoretical predictions for the $B(E1) \downarrow$ values, are undoubtedly useful.

Before proceeding, a short digression for a review of nuclear decay formalism as it applies to this particular case is beneficial. The decay probability per unit time for a particular nuclear configuration through decay channel n , denoted γ_n , is inversely related to the mean lifetime, τ_n [15]. i.e.,

$$\gamma_n = \frac{1}{\tau_n} . \quad (4.27)$$

Assuming the decay probabilities for every possible channel are determined, the absolute branching ratios, $Br.^n$, likewise are known, since

$$Br.^n = \frac{\gamma_n}{\gamma_{\text{tot}}} , \quad \text{with,} \quad \gamma_{\text{tot.}} = \sum_{n=1}^{\# \text{ chnls}} \gamma_n . \quad (4.28)$$

For the case of $E1$ γ -ray decay, the mean lifetimes are determined from the energy of the emitted photon, $E_{\gamma,n}$, and the reduced transition probability, $B(E1; n) \downarrow$, which contains the nuclear information for the involved states. Specifically,

$$\tau_n \text{ [fsec.]} \simeq \frac{0.629}{E_{\gamma,n}^3 B(E1; n) \downarrow} , \quad (4.29)$$

where, above, the reduced transition probability has been expressed in units of $e^2 \cdot \text{fm}^2$ and $E_{\gamma,n}$ in MeV.

Table 4.2 summarizes $E1$ decay branching for the first two excited 1^- states calculated with the formalism described above from the theoretical level scheme presented in Fig. 1.4. For each decay path, the energy and spin-parity of the final state along with the $B(E1) \downarrow$ value for the transition are specified, along with the resulting mean

Table 4.2: $E1$ branching from the first two excited 1^- states calculated from the predicted level scheme presented in Fig. 1.4.

E_i (MeV)	$J_{n,i}^\pi$	E_f (MeV)	$J_{n,f}^\pi$	E_γ (MeV)	$B(E1) \downarrow$ ($e^2 \text{ fm}^2$)	τ (fsec.)	$Br.$ (%)
5.1	1_1^-	0.0	0_0^+	5.1	1.4E-03	3.3E+00	77
5.1	1_1^-	5.0	0_1^+	0.1	2.1E-03	2.9E+05	~ 0
5.1	1_1^-	2.0	2_1^+	3.1	2.0E-03	1.1E+01	23
5.1	1_1^-	4.2	2_2^+	0.9	1.2E-03	7.2E+02	~ 0
6.2	1_2^-	0.0	0_0^+	6.2	1.0E-03	2.6E+00	66
6.2	1_2^-	5.0	0_1^+	1.2	2.5E-03	1.5E+02	1
6.2	1_2^-	2.0	2_1^+	4.2	1.3E-03	6.5E+00	26
6.2	1_2^-	4.2	2_2^+	2.0	3.2E-04	2.5E+01	7

lifetime. This calculated branching information can serve as a guide when interpreting the experimental evidence obtained after application of the free-form gates (“decay gates” 1 and 2) which are defined on Fig. 4.22. The projections of these gates onto the γ -ray energy axis are shown in Fig. 4.23. Unfortunately, with the experimental S800 resolution obtained, these cuts not mutually exclusive, e.g., some strength resulting from excitations to the 1_1^- state is inadvertently included in the decay cut for 1_2^- excitations.

An examination of Fig. 4.23a arguably reveals the signature of each of the expected

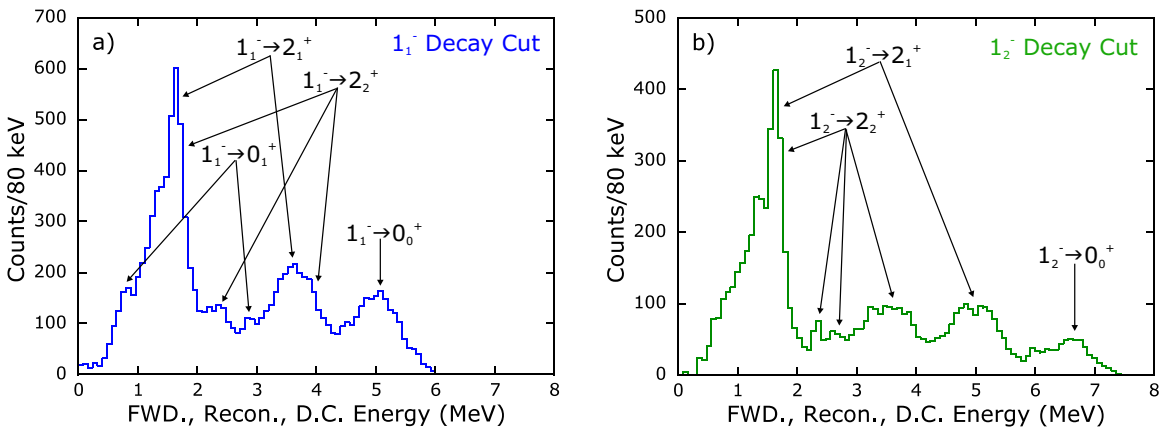


Figure 4.23: a) Projection of “decay gate 1” from Fig. 4.22 onto the γ -ray energy axis. Included mostly within this cut is strength which results from excitation of the 1_1^- state. b) The same for “decay gate 2,” therefore selecting excitation of the 1_2^- state. Evidence for various decay modes is highlighted for both excitation channels.

decay branches for the first-excited 1^- state. For instance, the peak at ~ 3.7 MeV likely contains components from both the 2_2^+ (4.072 MeV) and decays through the 2_1^+ (~ 3.6 MeV). Evidence also exists for decays via the first-excited 0^+ at 4.456 MeV. Decays which proceed through this state generally involve the emission of three simultaneous γ -rays, as, in most cases, the 0_1^+ state itself will decay sequentially through the first-excited 2^+ configuration. Assuming the 1_1^- state exists at 5.2 MeV we have the following for the energies of these three photons: 0.74, 2.79, and 1.67 MeV – the energy of the first photon in this set is adjustable in the sense that it depends on the actual energy of the 1_1^- state. Including the small but observable peaks at roughly 900 keV and 2.8 MeV, evidence exists for all three of the γ -rays for decays through the 0_1^+ . Additionally, the appearance of a 900 keV low-energy photon (rather than 740 keV) is a first indication that the 1_1^- state might actually be located above 5.3 MeV.

Moving on to a similar investigation of Fig. 4.23b, again, strong evidence of decays proceeding through both of the first two excited 2^+ states is visible. The fact that the peak near 2.4 MeV ($2_2^+ \rightarrow 2_1^+$ remnant) is sharper in this case suggests that decays through the 2_2^+ might be more important for this excitation channel. Assuming the 1_2^- state is found at roughly 6.7 MeV, decays through the 0_1^+ state would necessarily emit a ~ 2.24 MeV photon, which, in this case, is at an energy above the average T_h setting. Given the absence of an intense peak in this energy region, no decisive evidence exists for decays through the 0_1^+ . This conclusion is consistent with the evidence provided by analogous ^{18}O states, as only its 1_1^- state decays through the 0_1^+ state with significant probability.

What has not been mentioned in the analysis of either spectrum in Fig. 4.23 is the unmistakable structure at ~ 1.35 MeV. The analysis has revealed that this bump is actually an escape peak for 1.674 MeV transitions. It appears at about 320 keV below the 1.674 MeV peak, rather than 511 keV below, because this is a Doppler-corrected

spectrum. The fact that an escape peak is visible in this case and not for 2_1^+ decays in ^{18}O is a manifestation of the T_h settings, which, on average, were significantly higher for the ^{18}O experiment.

4.3.3 ^{20}O strength distribution and results

A comparison of the ^{20}O experimental strength distribution with a simulated equivalent is presented in Fig. 4.24a. With this comparison rather impressive agreement has been established in the region above 3 MeV. To facilitate this, the first two excited 1^- states were positioned at 5.35 and 6.85 MeV, which places them slightly higher than the initial prediction from Sec. 4.3.1. The positioning of the 1_1^- , indeed, is entirely consistent with the interpretation based on the branching analysis in the previous section which placed the state above 5.3 MeV from the observation of low-energy γ -rays at ~ 900 keV. Shown in Fig. 4.24b, meanwhile, on a logarithmic scale, are the individual components which contribute to the simulated strength distribution. Most significant is the fact that $E1$ excitations, as expected, are dominating, which is especially true

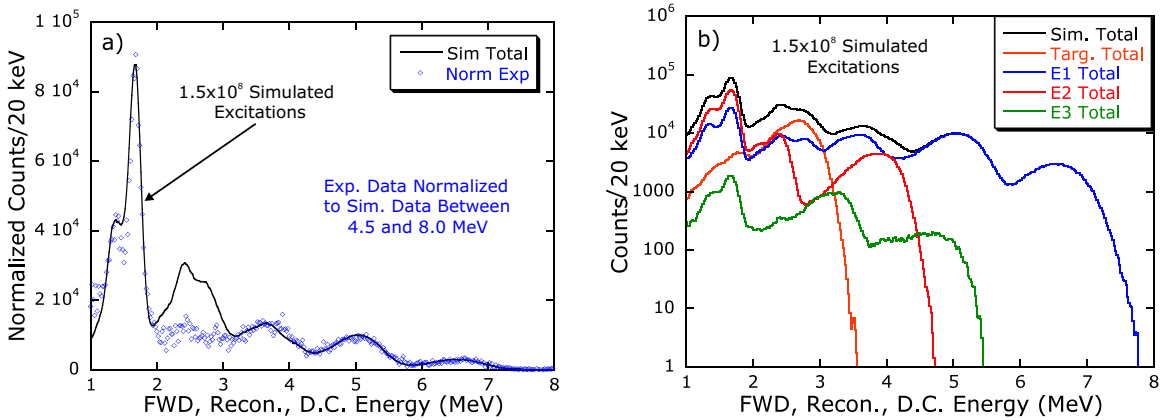


Figure 4.24: a) Final experimental ^{20}O strength distribution (data points) shown with simulated data (solid line) generated using estimated branching information along with appropriately adjusted $B(E\lambda)$ values. The experimental data has been normalized to the simulated results in the region between 4.5 and 8 MeV. b) The individual components which contribute to the total simulated strength distribution. Notice that $E1$ excitations are now the dominant contribution.

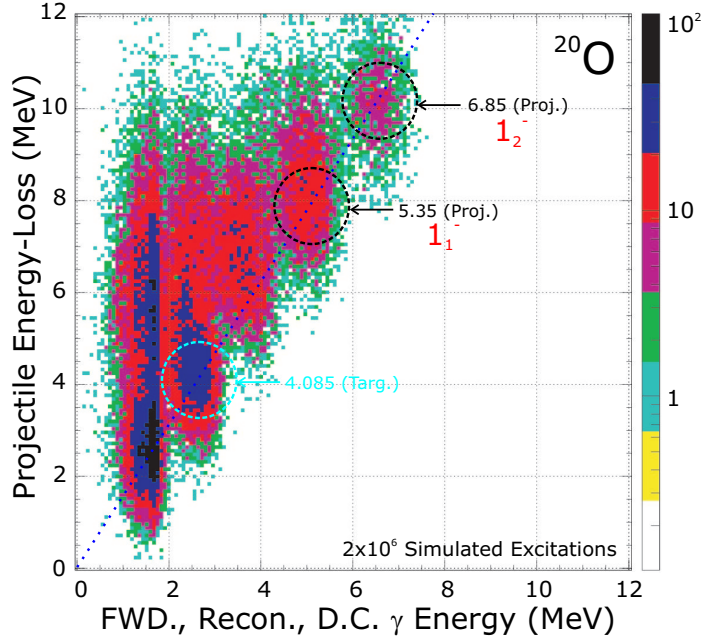


Figure 4.25: Projectile energy-loss vs. forward, reconstructed, Doppler-corrected γ -ray energy for simulated ^{20}O events. Comparison with the experimental equivalent, Fig. 4.22, provides confidence that the results of the ^{20}O experiment have been properly interpreted.

above 4 MeV. A comparison of Fig. 4.22 with Fig 4.25, which is the simulated version of projectile energy-loss vs. total, forward, Doppler-corrected γ -ray energy, further emphasizes that the simulation has achieved remarkable agreement. Moreover, it is apparent from this comparison that nothing significant has been overlooked in the interpretation of the experimental results.

The production of this simulated result presented in Fig. 4.24 has utilized the ^{20}O level scheme which is given in Table 4.3 along with the branching presented in Table 4.4. The measured value of the $B(E2)$ for the 2_1^+ state has been used, while the $B(E2)$ for the 2_2^+ is consistent with the theoretical prediction for this state of $7.8 e^2 \text{fm}^4$. Notice that the simulation has incorporated a 3^- level at 5.0 MeV. Recall, the experimental ^{20}O level scheme includes two states with undetermined and unconfirmed spin-parity at 5.002 and 5.614 MeV, respectively. For the simulation, it was simply *assumed* that the 5.002 MeV is the 3^- state which corresponds to the

Table 4.3: The projectile and target level schemes utilized in the production of the simulated results presented in Fig. 4.24. The known experimental value of the $B(E2)$ for the 2_1^+ state in ^{20}O has been used [26], along with that of the $B(E3)$ for the 3_1^- state in ^{208}Pb [31]. The $B(E2)$ value for the 2_1^+ state in ^{208}Pb has been adjusted within the reported experimental limit [26].

Projectile: ^{20}O		
E_x (MeV)	J_n^π	$B(E\lambda) \uparrow (e^2 \text{fm}^{2\lambda})$
1.67	2_1^+	2.80E+01
4.07	2_2^+	9.00E+00
5.00	3_1^-	1.60E+03
5.23	2_3^+	7.00E-04
5.35	1_1^-	1.35E-02
6.85	1_2^-	1.10E-02
Target: ^{208}Pb		
E_x (MeV)	J_n^π	$B(E\lambda) \uparrow (e^2 \text{fm}^{2\lambda})$
2.61	3_1^-	6.11E+05
4.09	2_1^+	2.60E+03

Table 4.4: All ^{20}O branching used for the simulated results presented in Fig. 4.24. Only the branching from the 2_2^+ state has been previously established [34].

E_i (MeV)	$J_{n,i}^\pi$	E_f (MeV)	$J_{n,f}^\pi$	E_γ (MeV)	$Br.$ (%)
1.67	2_1^+	0.00	0_0^+	1.67	100
3.57	4_1^+	1.67	2_1^+	1.90	100
4.07	2_2^+	1.67	2_1^+	2.40	74
4.07	2_2^+	0.00	0_0^+	4.07	26
4.46	0_1^+	1.67	2_1^+	2.79	100
5.00	3_1^-	4.07	2_2^+	0.93	18
5.00	3_1^-	3.57	4_1^+	1.43	6
5.00	3_1^-	1.67	2_1^+	3.33	76
5.23	2_3^+	4.07	2_2^+	1.16	10
5.23	2_3^+	1.67	2_1^+	3.56	60
5.23	2_3^+	0.00	0_0^+	5.23	30
5.35	1_1^-	4.46	0_1^+	0.89	22
5.35	1_1^-	4.07	2_2^+	1.28	10
5.35	1_1^-	1.67	2_1^+	3.68	38
5.35	1_1^-	0.00	0_0^+	5.35	30
6.85	1_2^-	4.07	2_2^+	2.78	28
6.85	1_2^-	1.67	2_1^+	5.18	40
6.85	1_2^-	0.00	0_0^+	6.85	32

predicted level at 5.0 MeV, though no experimental evidence exists for this assignment. Given the expected insignificance of $E3$ excitations from the predicted $B(E3)$ value for the theoretical 3^- state, the specific placement of this level essentially has no effect on the results. Hence, this ambiguity is of no concern.

What has not yet been discussed concerning Fig. 4.24 is a significant discrepancy between the simulation and the experimental results from roughly 2 to 3 MeV. For the simulation (as can be seen in Fig. 4.24b), this is the region where γ -rays from the first-excited $2+$ state in the target and the 2_2^+ level in the projectile are the dominant contributions. Reproduction of the escape-peak at ~ 1.35 MeV along with a 1.67 MeV peak intensity which remains consistent with the measured $B(E2)$ for 2_1^+ requires that the average T_h setting used in the ^{20}O simulation be lowered substantially from 3.8 MeV (the value used for ^{18}O simulations) to roughly 1.5 MeV. It is precisely this lowering of the average T_h settings, however, which facilitates the emergence of the observed discrepancy. Keeping the average T_h threshold at a low setting, much better agreement between 2 and 3 MeV can be established by simultaneously increasing the $B(E1)$ values for the 1^- projectile levels while decreasing their 2_2^+ decay branching, effectively reducing the relative intensity of the discrepancy.

An illustration of this point is provided by Fig 4.26, which is a familiar plot of simulated data which has been generated using precisely this strategy. The reader can verify that much better agreement with the experimental result in the targeted region has been established. Table 4.5 specifies the $B(E\lambda)$ information which has been incorporated into the simulation to produce these results. Note, especially, that the $B(E1)$ strength for the 1^- states has been increased substantially. For example, the $B(E1)$ for the 1_1^- has been boosted by a factor of more than 14 over B. A. Brown's prediction. Two *new* discrepancies have emerged in this process, namely, the simulation now under-produces γ -rays from de-excitations of the 2_1^+ and 2_2^+ levels. Out of an attempt to resolve the latter issue, the $B(E2)$ for the 2_2^+ was increased by a factor of

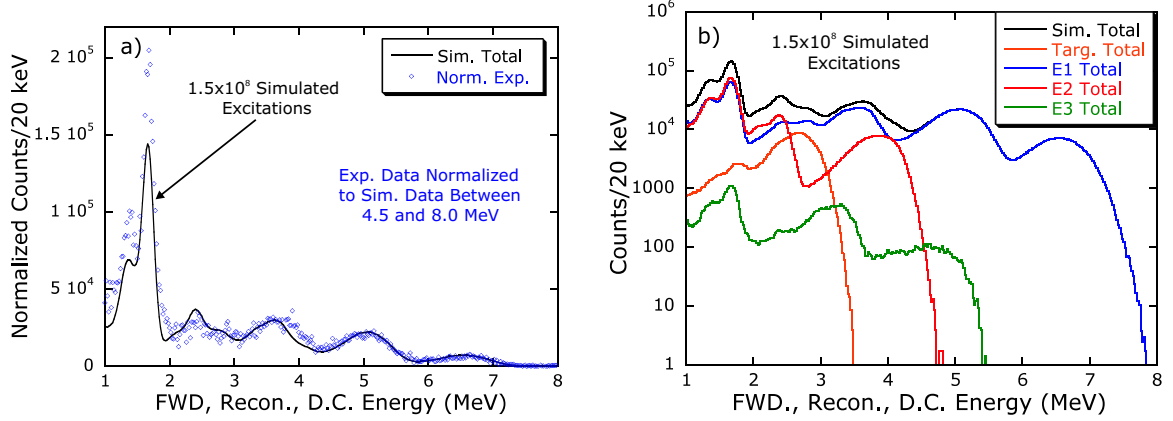


Figure 4.26: a) Final experimental ^{20}O strength distribution (data points) shown with simulated data (solid line) generated using, for example, substantially increased $B(E1)$ values for each of the 1^- states. The experimental data has been normalized to the simulated results in the region between 4.5 and 8 MeV. Much better agreement has been established in the targeted region. b) The individual components which contribute to the total simulated strength distribution.

nearly four, to $30 e^2 \text{fm}^4$. Further improvement of the discrepancy at ~ 4 MeV could be gained by additional increases of the $B(E2)$ for the 2_2^+ state. However, this would come at the expense of an increased overabundance of 2.4 MeV γ -rays – recall, the 2_2^+ configuration decays with high probability through the 2_1^+ state. The only strategy for simultaneously improving both of these new discrepancies involves lowering the $B(E2)$ strength for the 2_2^+ closer to its predicted value while *further*-increasing the $B(E1)$ values for the 1^- states. A relative boost of 2_1^+ and 2_2^+ γ -decays could then be provided by funneling more of the 1^- decay probability through each of these 2^+ levels, at the expense of the direct ground state decay channel.

Given this, the $B(E1)$ strengths presented in Table 4.5 can be interpreted as experimental lower limits. While these $B(E1)$ strengths are, in general, higher than the shell model predictions for levels below 6.9 MeV, they are not unreasonable. For example, calculations performed by H. Sagawa and T. Suzuki (using the WB10 residual interaction) predict the existence of two 1^- levels between 6.7 and 7.5 MeV with $B(E1)$ strengths of 0.014 and 0.024 $e^2 \text{fm}^2$ [32]; alternatively, an integration of their calculated dipole strength curve (which is presented as Fig. 5.1 in Chapter 5)

Table 4.5: The projectile and target level schemes utilized in the production of the improved ^{20}O simulated results presented in Fig. 4.26. The $B(E2)$ strength for the 2_1^+ state in ^{20}O has been increased within the established limit [26], while that of the 2_2^+ state is a factor of nearly four above the prediction. Note, the $B(E1)$ strength has been substantially increased.

Projectile: ^{20}O		
E_x (MeV)	J_n^π	$B(E\lambda) \uparrow (e^2 \text{fm}^{2\lambda})$
1.67	2_1^+	3.00E+01
4.07	2_2^+	3.00E+01
5.00	3_1^-	1.60E+03
5.23	2_3^+	7.00E-04
5.35	1_1^-	6.20E-02
6.85	1_2^-	3.50E-02
Target: ^{208}Pb		
E_x (MeV)	J_n^π	$B(E\lambda) \uparrow (e^2 \text{fm}^{2\lambda})$
2.61	3_1^-	6.11E+05
4.09	2_1^+	2.60E+03

Table 4.6: ^{20}O 1^- branching used for the improved simulated results presented in Fig. 4.26. Branching for all other states is the same as presented in Table 4.4.

E_i (MeV)	$J_{n,i}^\pi$	E_f (MeV)	$J_{n,f}^\pi$	E_γ (MeV)	$Br.$ (%)
5.35	1_1^-	4.46	0_1^+	0.89	19
5.35	1_1^-	4.07	2_2^+	1.28	5
5.35	1_1^-	1.67	2_1^+	3.68	46
5.35	1_1^-	0.00	0_0^+	5.35	30
6.85	1_2^-	4.07	2_2^+	2.78	10
6.85	1_2^-	1.67	2_1^+	5.18	39
6.85	1_2^-	0.00	0_0^+	6.85	51

from 4 to 8 MeV, the region that encompasses the two established 1^- states, results in $\sim 0.09 e^2 \text{fm}^2$. Also, complementary WBP shell model calculations by B. A. Brown (which have been the basis for previous comparisons within this thesis) predict the existence of a ~ 7.7 MeV state with a larger $B(E1)$ strength of $0.075 e^2 \text{fm}^2$ [9].

The specific 1^- γ -decay branching which was incorporated into the simulation to produce the results presented in Fig. 4.26 is given in Table 4.6. All other branching used for this improved simulation is identical to that presented in Table 4.4. As has been mentioned, the decay ratios for the 2_2^+ state are the only ones which have been

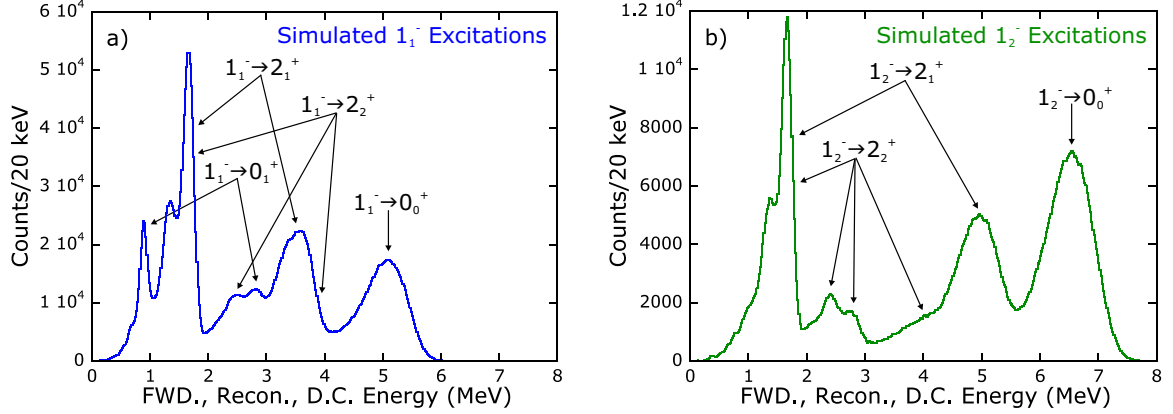


Figure 4.27: The simulated strength curves resulting from excitations to the 1_1^- (a) and 1_2^- (b) states. Peaks resulting from various decay paths are highlighted. Note the similarities with Fig. 4.23.

previously established [34]. For both the improved ^{20}O simulation, and the former presented as Fig. 4.24, educated guesses have been made for the branching from 0_1^+ , 3_1^- , and 2_3^+ states based mostly on comparison with the known ^{18}O level structure [35]. Again, given the fact that excitations to the 3_1^- and 2_3^+ states are unimportant, however, the uncertainty associated with this guessing bears no weight on the results. As has been demonstrated in previous discussion, the branching for the two 1^- states was established from theoretical predictions, ^{18}O information, and from “trial and error” comparison against experimental evidence, the latter method ultimately bearing the most weight. Precisely because of this method by which the 1^- branching has been determined, it is extremely difficult to establish the associated uncertainty. A conservative estimate, though, can come out of a comparison of the 1^- branching presented in Table 4.4 with that in Table 4.6, e.g., no individual decay branch differs by more than 20 (in units of absolute percentage).

Confidence in the obtained 1^- branching information is gained from a comparison of Fig. 4.27, which shows the (improved) simulated strength curves resulting from excitations to the 1_1^- (a) and 1_2^- (b) states, against the experimental equivalent presented earlier (Fig. 4.23). Unlike the experimental 1^- decay spectra (which contained contamination due to inadequate S800 energy resolution) the simulated spectra are

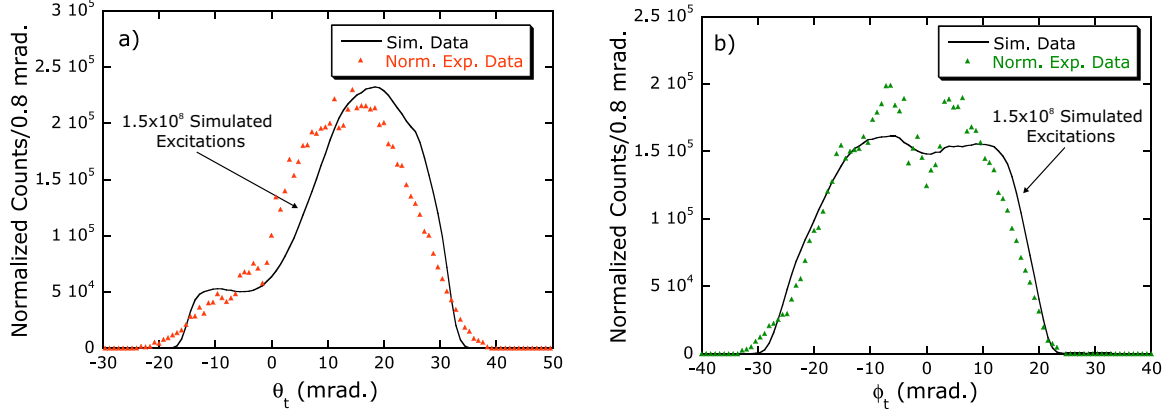


Figure 4.28: The final ^{20}O θ_t (a) and ϕ_t (b) experimental angular distributions (data points) shown against the results obtained from the improved simulation (solid lines). The experimental data has been normalized to the simulated results.

generated with a software cut which excludes contributions from all other excitations. The differences observed between Fig. 4.27 and Fig. 4.23 can therefore be attributed to a combination of γ -decay branching uncertainty and contamination in the experimental curves. The important conclusion from this comparison is that no transitions (peaks) in the experimental decay spectra are unaccounted for, i.e., all important 1^- decay branches have been incorporated into the simulation.

For completeness it is necessary to show the angular distributions obtained with the simulation against those which were experimentally observed. As was the case with the ^{18}O comparison, Fig. 4.28 demonstrates that while the microscopic agreement is not so impressive, the overall acceptance has been adequately reproduced. Moreover, the simulation has reproduced the double-peak structure observed in the experimental ϕ_t data. As was first explained in Chapter 3, the distribution is double-peaked for the case of ^{20}O , rather than single-peaked as in the ^{18}O experiment, because of the differences in the shape of the acceptance “window.”

Chapter 5

Closing remarks

5.1 Experimental conclusions

Two successive Coulomb excitation experiments were performed at the NSCL in order to investigate low-lying isovector GDR strength in ^{18}O and ^{20}O . While no conclusions could be reached regarding $E1$ strength above the neutron separation energy for either nucleus, it was possible to analyze the γ -ray transitions resulting from excitation of the discrete states. Monte Carlo simulations written within a GEANT environment, used for direct comparisons with the experimental results, were invaluable with regard to interpreting the experimental data. The analysis showed that $E2$ excitations dominated the observed strength function for ^{18}O while $E1$ excitations became more important for the case of ^{20}O , as predicted by theory.

Two previously unmeasured ^{20}O 1^- states were observed at 5.35 and 6.85 MeV. These energies are in good agreement with, for example, B. A. Brown's shell model predictions that place excited 1^- levels at 5.1, 6.2 and 7.2 MeV [9] (see Table 5.1). γ -decay branching from these 1^- states has been established to within $\sim 20\%$. Along with direct ground state branches, both 1^- states decay through the 2_1^+ state. Evidence also exists for 1^- γ -decays through the 2_2^+ configuration, this branch probably being

Table 5.1: ^{20}O shell model predictions for 1^- levels from B. A. Brown [9] and also from H. Sagawa and T. Suzuki [27, 32].

^{20}O shell model predictions					
B.A. Brown (WBP)			H. Sagawa and T. Suzuki (WB10)		
J_n^π	E (MeV)	$B(E1) \uparrow (e^2 \text{ fm}^2)$	J_n^π	E (MeV)	$B(E1) \uparrow (e^2 \text{ fm}^2)$
1_1^-	5.1	4.3E-03	1_1^-	4.1	3.7E-04
1_2^-	6.2	3.1E-03	1_2^-	5.5	2.5E-03
1_3^-	7.2	2.6E-03	1_3^-	6.1	8.9E-03
1_4^-	7.7	7.6E-02	1_4^-	6.8	1.4E-02
			1_5^-	7.5	2.4E-02

more important for the 6.85 MeV state. Specific to the 1^- state at 6.85 MeV was the observation of a decay branch through the 0^+ level at 4.456 MeV. In addition to having established the energies and approximate γ -decay branchings from these two excited 1^- configurations, approximate $B(E1) \uparrow$ lower limits have been extracted from the results. Specifically, $B(E1; 0.00 \rightarrow 5.35) \uparrow \geq 0.062 e^2 \text{ fm}^2$, while $B(E1; 0.00 \rightarrow 6.85) \uparrow \geq 0.035 e^2 \text{ fm}^2$. As can be verified from a comparison with Table 5.1, these values are, in general, somewhat higher than predictions for 1^- levels.

To investigate the mechanism which results in larger $B(E1)$ values for these 1^- levels in ^{20}O it may be useful to compare ^{18}O strengths and the current ^{20}O results (in Weisskopf units) with known $B(E1)$ strengths for discrete levels in complementary 2 and 4-valence-neutron systems such as $^{42,44}\text{Ca}$ and/or $^{58,60}\text{Ni}$. Unfortunately, due to the experimental challenges associated with much higher level densities in this mass region, not much experimental information is currently available for these nuclei. For example, only one 1^- level has been established in ^{42}Ca (3.885 MeV) [30] while none are established in ^{44}Ca [11]. No $B(E1)$ information is currently known for either calcium isotope. 1^- levels have been established in ^{58}Ni (at 5.903 and 6.024 MeV, having $B(E1)$ strengths of 0.0070 and 0.0015 W.u.) from (e, e') and (γ, γ') studies [8]. Unfortunately, no such information currently exists for the more relevant 4-neutron skin configuration, ^{60}Ni [2].

5.2 Future virtual photon scattering studies with ^{20}O at the NSCL

Shown in Fig. 5.1 is an ^{20}O dipole strength prediction which has been calculated assuming $1\hbar\omega$ excitations in the $(0p-1s0d-1p0f)$ shell model space with a WB10 residual interaction. While the current study has been unable to verify these predictions regarding strength above the neutron binding threshold, the results summarized in Sec. 5.1 provide confidence that a follow-up study using a similar experimental set-up will be successful. For example, the measured intensity of de-excitations from the 6.85 MeV level in the current study allows for a reliable estimation of counting rates for higher-energy γ -rays. Fig. 5.2a) plots expected γ -ray intensities per 1 MeV bin, normalized to the intensity of 6.85 MeV de-excitations. This figure has been generated from Coulomb excitation calculations which have utilized the $B(E1)$ information in Fig. 5.1 along with the shell model prediction for the $B(E1) \uparrow$ value for the second-excited 1^- state ($0.0031 e^2 \text{fm}^2$) [9], assuming, conservatively, that neutron decays are 1000 times more probable than γ -ray decays above S_n . Separate intensity curves have been generated for total laboratory frame acceptances of 20, 40, and 60 mrad. It should be mentioned that the incorporation of the current experimental findings,

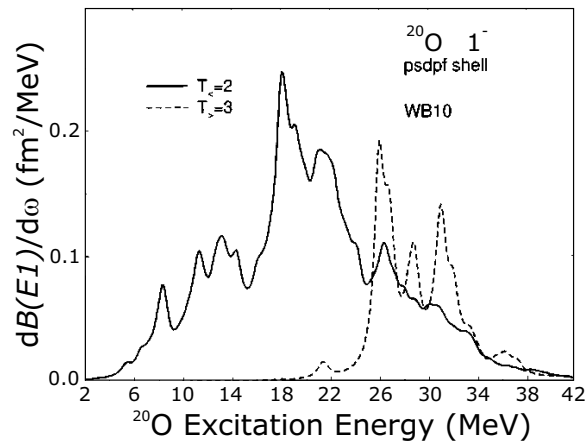


Figure 5.1: ^{20}O $E1$ excitation function, $dB(E1)/d\omega$, calculated with $1\hbar\omega$ excitations in the $(0p-1s0d-1p0f)$ model space using a WB10 interaction (taken from Ref. 27).

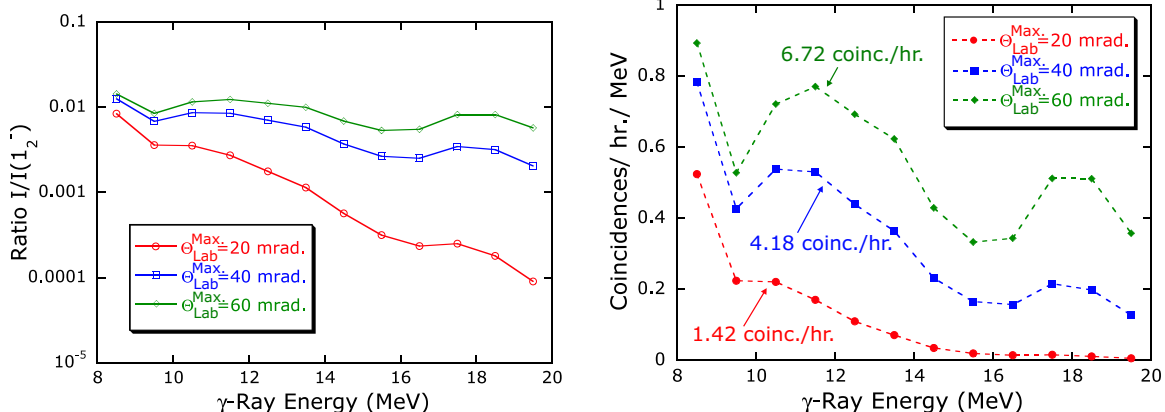


Figure 5.2: Predictions for intensities of γ -rays between 8 and 20 MeV based on Coulomb excitation calculations which have used theoretical information presented as Fig. 5.1 along with the $B(E1)$ prediction for the 1_2^- state. Curves have been generated for laboratory-frame acceptances of 20, 40, and 60 mrad. a) The y -axis has been normalized to the intensity of γ -rays resulting from de-excitation of the 6.85 MeV level. b) The experimental counting rate for 6.85 MeV excitations has been used to re-express the intensity calculations in more informative units. – these intensities are valid for a ^{20}O beam intensity of $\sim 5 \times 10^5$.

namely that the $B(E1)$ for this 1^- level is likely a factor of ~ 10 above the prediction of $0.0031 e^2 \text{ fm}^2$, would shift the intensity predictions in Fig. 5.2a) a corresponding factor of 10 downwards. This factor is regained, however, if we assume that neutron decays are 100 (rather than 1000) times more likely.

Based on the experimental observation of approximately 7500 6.85 MeV decays within a total run time of ~ 120 hours, with the assumption that the counting efficiency of the array is flat in the energy region shown, one can translate the y -axis of Fig. 5.2a) to units of coincidences per hour per γ -ray MeV. (The energy of the *emitted*, rather than *detected*, γ -ray is what is specified by this conversion). The result of this re-scaling process is given in Fig. 5.2b). The total integrated count rates per hour are ~ 1.4 , 4.2, and 6.7 for the 20, 40 and 60 mrad acceptance curves, respectively. The reader may recall from the ^{20}O angular distributions (e.g., Fig. 4.28) that the achieved S800 acceptance was ~ 20 mrad. This acceptance value, however, does not incorporate the fact that the blocker removed approximately half of the θ_t distribution which

eliminated $\sim 25\%$ of the projectile scattering cone, effectively reducing the count rate by $\sim 25\%$. Hence, the integrated count rate for γ -rays between 8 and 20 MeV which is predicted by Fig. 5.2b) for the current study becomes approximately 1 per hour, which provides an explanation as to why the experiment was not successful at probing the strength function in this energy region.

As one can see clearly from the relationship between the curves in Fig. 5.2, a modest improvement in the experimental acceptance would markedly improve the counting rates for γ -rays from the targeted energy region. This is a direct manifestation of the fact that the $E1$ Coulomb excitation probability distribution (as a function of laboratory-frame scattering angle) peaks between roughly 20 and 60 mrad. For a follow-up study using essentially the same set-up (with the re-positioned target) the GDR-region coincidence counting rate would likely benefit from operating the S800 at, say, 1.7° . In addition to reducing the counting/acceptance losses due to the blocker, this spectrometer placement would strategically sample the peak (rather than the incline) of $E1$ probability distribution function. These strides made in the counting rate due to S800 positioning are meek, however, when compared with the improvement in ^{20}O beam intensity which has been made available by the recent coupled cyclotron upgrade at the NSCL. For example, according to the CCF/A1900 production rate code LISE [33], the predicted beam intensity for 100 MeV/u ^{20}O (assuming a ^{22}Ne primary beam on a ^9Be production target) is $\sim 1 \times 10^7$ which is an impressive factor of 20 times that which was available for the current study. These combined improvements boost the expected counting rate for γ -rays between 8 and 20 MeV to ~ 100 per hour, which is indeed an exciting prospect.

Appendix A

Reaction kinematics

This appendix will delve into the realm of relativistic two-body kinematics. Relations which are pertinent to the current study will be derived from standard momentum and energy conservation principles. For simplification of all expressions, the replacement $c \rightarrow 1$ will be made, or, equivalently, we will work in a scheme with implied units for momentum and mass, $[p]$ and $[m]$, of $[E]/c$ and $[E]/c^2$, respectively. The physical process we will examine involves a collision in the laboratory of particle A, with mass m_A and momentum p_A , with particle B, of mass m_B , which is initially at rest, as represented in Fig. A.1. As is typically the case, symbols referring to quantities after the collision will be denoted with a prime. The particles are scattered in the reaction plane to laboratory angles $\theta_{A'}$ and $\theta_{B'}$ with respect to the direction of \vec{p}_A . Particles A' and B' carry away momenta $\vec{p}_{A'}$ and $\vec{p}_{B'}$, respectively. The possibility for an inelastic process occurring is introduced by the simple substitutions,

$$\begin{aligned} m_{A'} &\rightarrow m_A + E_{A'}^* \\ m_{B'} &\rightarrow m_B + E_{B'}^* , \end{aligned} \tag{A.1}$$

where $E_{A'}^*$ and $E_{B'}^*$ are the excitation energies of the particles after the collision.

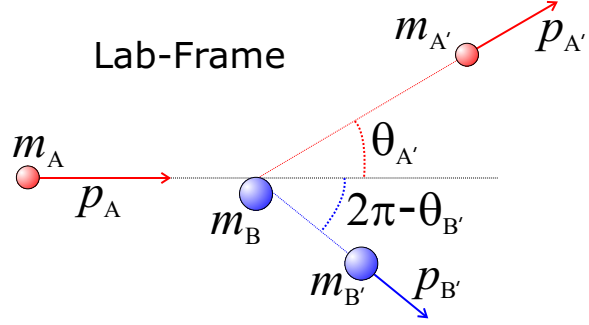


Figure A.1: Scattering of particles A and B in the laboratory frame. Particle B is at rest initially.

A.1 Review of Lorentz transformations

Before proceeding further into the dynamics of the collision using a relativistic treatment, it will be useful to review the basics of Lorentz transformations. Formally, we will work in Minkowski space, in which a particle's 4-momentum is represented as

$$\mathbf{p} = \begin{pmatrix} p_1 \\ p_2 \\ p_3 \\ p_4 \end{pmatrix} = \begin{pmatrix} \vec{p} \\ iE \end{pmatrix}. \quad (\text{A.2})$$

This discussion will benefit from a particular example, where we relate a particle's 4-momentum in a moving frame, denoted \mathbf{p}' , to that in a frame which is at rest, \mathbf{p} . For simplicity we will assume that the motion of the primed frame is along the z-axis of the stationary frame. The relationship is:

$$\mathbf{p}' = \Lambda \mathbf{p}, \quad (\text{A.3})$$

where Λ , the Lorentz transformation matrix, has the form [13]

$$\Lambda = \begin{pmatrix} 1 & 0 & 0 & 0 \\ 0 & 1 & 0 & 0 \\ 0 & 0 & \gamma & i\gamma\beta \\ 0 & 0 & -i\gamma\beta & \gamma \end{pmatrix}. \quad (\text{A.4})$$

To apply this for a simple case, assume the particle is at rest in the moving frame, i.e.,

$$\mathbf{p}' = \begin{pmatrix} 0 \\ 0 \\ 0 \\ im \end{pmatrix}.$$

The 4-momentum of this particle in the stationary frame can be calculated using the inverse relationship

$$\mathbf{p} = \Lambda^{-1}\mathbf{p}', \quad (\text{A.5})$$

where the inverse transformation, Λ^{-1} , is related to the direct transformation by

$$\Lambda^{-1} = \Lambda_{\beta \rightarrow -\beta}.$$

Therefore,

$$\Lambda^{-1} = \begin{pmatrix} 1 & 0 & 0 & 0 \\ 0 & 1 & 0 & 0 \\ 0 & 0 & \gamma & -i\gamma\beta \\ 0 & 0 & i\gamma\beta & \gamma \end{pmatrix}. \quad (\text{A.6})$$

Hence,

$$\mathbf{p} = \begin{pmatrix} 0 \\ 0 \\ \gamma\beta m \\ i\gamma m \end{pmatrix}.$$

But, on the other hand, since the particle is at rest in the boosted frame, this implies

$$\mathbf{p} = \begin{pmatrix} 0 \\ 0 \\ p \\ iE \end{pmatrix}$$

since the motion of the boosted frame is entirely along the z-axis.

Equating the two 4-vector expressions for \mathbf{p} we find

$$\begin{aligned} p &= \gamma\beta m \\ E &= \gamma m, \end{aligned} \quad (\text{A.7})$$

which are the well known relations for a particle of mass m which moves with velocity β . Lorentz invariance demands that the contraction of the 4-momentum in any frame

be equivalent, so that

$$\mathbf{p} \cdot \mathbf{p} = p^2 - E^2 = \mathbf{p}' \cdot \mathbf{p}' = -m^2 .$$

Which gives us the famous relation,

$$E^2 = p^2 + m^2 . \tag{A.8}$$

A.2 Two-body collision dynamics

Of specific interest to this study is the derivation of an expression which will relate the center-of-mass scattering angle, $\theta_{A',cm}$, to that in the laboratory frame $\theta_{A',lab}$. This is necessary since one of the tasks which the simulation needed to perform was a calculation of $\theta_{A',lab}$ given $\theta_{A',cm}$, $E_{A,lab}$, and the excitation energy (energies) of particle(s) A' (and B'). A derivation of a useful expression for the total energy in the center-of-mass is first required. Taking advantage of Lorentz invariance of the inner product of the total 4-momentum before the collision in each frame we have

$$\mathbf{P}_{cm} \cdot \mathbf{P}_{cm} = \mathbf{P}_{lab} \cdot \mathbf{P}_{lab} .$$

Since the total momentum in the C.M. system is by definition zero, the above relation becomes

$$E_{cm}^2 = E_{lab}^2 - p_{lab}^2 .$$

But,

$$E_{lab} = E_{A,lab} + E_{B,lab} ; E_{B,lab} = m_B .$$

Hence,

$$E_{cm}^2 = E_{A,lab}^2 + 2E_{A,lab} m_B + m_B^2 - p_{lab}^2 .$$

Substituting

$$p_{lab}^2 = p_{A,lab}^2 = E_{A,lab}^2 - m_A^2 ,$$

we come to the useful result,

$$E_{cm}^2 = 2E_{A,lab} m_B + m_A^2 + m_B^2 . \quad (\text{A.9})$$

Equation A.9 will be utilized at a later stage in the derivations. Of immediate importance is knowledge of the velocity of the center-of-mass frame in the laboratory, $\beta_{cm} \rightarrow \beta$. The Lorentz transformation gives it directly, since

$$p_{3,cm} = 0 = \Lambda_{33} p_{3,lab} + \Lambda_{34} p_{4,lab} = \gamma(p_{A,lab} - \beta E_{lab}) .$$

Rearranging, with $E_{lab} = E_{A,lab} + m_B$, we find

$$\beta = \beta_{cm} = \frac{p_{A,lab}}{E_{A,lab} + m_B} . \quad (\text{A.10})$$

We will now work with quantities after the collision to derive the useful relationship between the scattering angles of particle A' in the laboratory and center-of-mass frames. The 4-momentum of particle A' can be expressed as

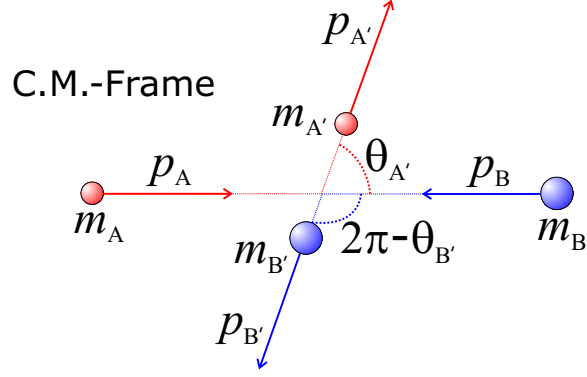


Figure A.2: Scattering of particles A and B as viewed in the center-of-mass frame.

$$\mathbf{p}_{A',lab} = \begin{pmatrix} p_{A',lab} \sin(\theta_{A',lab}) \\ 0 \\ p_{A',lab} \cos(\theta_{A',lab}) \\ iE_{A',lab} \end{pmatrix} \quad (\text{A.11})$$

in the laboratory frame, and as

$$\mathbf{p}_{A',cm} = \begin{pmatrix} p_{A',cm} \sin(\theta_{A',cm}) \\ 0 \\ p_{A',cm} \cos(\theta_{A',cm}) \\ iE_{A',cm} \end{pmatrix} \quad (\text{A.12})$$

in the center-of-mass frame. The two are related by a Lorentz transformation, e.g.,

$$\mathbf{p}_{A',lab} = \Lambda^{-1} \mathbf{p}_{A',cm} .$$

Thus,

$$\mathbf{p}_{A',lab} = \begin{pmatrix} p_{A',cm} \sin(\theta_{A',cm}) \\ 0 \\ \gamma \{ p_{A',cm} \cos(\theta_{A',cm}) + \beta E_{A',cm} \} \\ i \gamma \{ \beta p_{A',cm} \cos(\theta_{A',cm}) + E_{A',cm} \} \end{pmatrix}. \quad (\text{A.13})$$

Comparison of Eq. A.11 and Eq. A.13 provides three useful relations, namely,

$$\begin{aligned} p_{A',lab} \sin(\theta_{A',lab}) &= p_{A',cm} \sin(\theta_{A',cm}) \\ p_{A',lab} \cos(\theta_{A',lab}) &= \gamma \{ p_{A',cm} \cos(\theta_{A',cm}) + \beta E_{A',cm} \} \\ E_{A',lab} &= \gamma \{ \beta p_{A',cm} \cos(\theta_{A',cm}) + E_{A',cm} \}. \end{aligned} \quad (\text{A.14})$$

Division of the first two yields

$$\tan(\theta_{A',lab}) = \frac{\sin(\theta_{A',cm})}{\gamma \left(\cos(\theta_{A',cm}) + \frac{\beta E_{A',cm}}{p_{A',cm}} \right)},$$

or,

$$\tan(\theta_{A',lab}) = \frac{\sin(\theta_{A',cm})}{\gamma \left(\cos(\theta_{A',cm}) + \frac{\beta}{\beta_{A',cm}} \right)}. \quad (\text{A.15})$$

This nice result is dependent on $\beta_{A',cm}$, the velocity of particle A' in the C.M. frame, which is a quantity that we would like to express in terms of those we already know. We expect a priori that $\beta_{A',cm}$ has no angular dependence since total momentum in this frame is always zero. We will begin by writing down an expression for the total momentum in the center-of-mass after the collision:

$$E_{cm} = E_{A',cm} + E_{B',cm} = \gamma_{A',cm} m_{A'} + \sqrt{p_{B',cm}^2 + m_{B'}^2}.$$

But since $p_{B',cm}^2 = p_{A',cm}^2$, this becomes,

$$\begin{aligned}
E_{cm} &= \gamma_{A',cm} m_{A'} + \sqrt{p_{A',cm}^2 + m_{B'}^2} \\
&= \gamma_{A',cm} m_{A'} + \sqrt{\gamma_{A',cm}^2 m_{A'}^2 - m_{A'}^2 + m_{B'}^2} \\
&= \gamma_{A',cm} m_{A'} + \sqrt{m_{A'}^2(\gamma_{A',cm}^2 - 1) + m_{B'}^2} .
\end{aligned} \tag{A.16}$$

This result, which is quadratic in $\gamma_{A',cm}$, can be easily solved for $\gamma_{A',cm}$. The solution is

$$\gamma_{A',cm} = \frac{m_{A'}^2 - m_{B'}^2 + E_{cm}^2}{2m_{A'}E_{cm}} , \tag{A.17}$$

which directly gives $\beta_{A',cm}$ since,

$$\beta_{A',cm} = \sqrt{1 - \gamma_{A',cm}^{-2}} . \tag{A.18}$$

From Eq. A.17 it becomes clear why Eq. A.9, which was derived from quantities before the collision, is particularly useful. Substitution of the solution for $\beta_{A',cm}$ into the expression for $\theta_{A',lab}$, Eq. A.15, provides us with the desired relationship which depends only on $\theta_{A',cm}$, $E_{A,lab}$, and the excitation energies of the participating particles.

Appendix B

Intermediate-energy Coulomb excitation

This appendix will provide some useful mathematical formalism which is applicable to the process of intermediate energy Coulomb excitation. “Intermediate” refers to projectile kinetic energies of tens to a few hundred MeV/u. The approach which will be outlined here is semi-classical since a classical Rutherford trajectory is assumed for the projectile, while the interaction between the projectile and target is treated quantum-mechanically using first-order perturbation theory.

B.1 The excitation cross section

The differential cross section for Coulomb excitation can be expressed as [1]

$$\frac{d\sigma}{d\Omega} = \left(\frac{d\sigma}{d\Omega} \right)_{\text{Ruth.}} P_{i \rightarrow f} , \quad (\text{B.1})$$

where the classical Rutherford cross section relation is given by

$$\left(\frac{d\sigma}{d\Omega} \right)_{\text{Ruth.}} = \frac{a^2}{4 \sin^4 \left(\frac{\vartheta}{2} \right)} . \quad (\text{B.2})$$

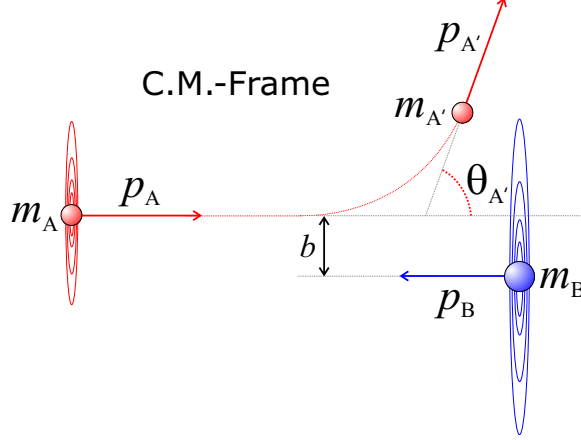


Figure B.1: Coulomb excitation of the projectile (A) as it scatters from the Coulomb field of the target (B), depicted in the center-of-mass frame. A virtual photon has been absorbed in the process.

In Eq. B.2 the angle ϑ is the projectile scattering angle in the center-of-mass, $\vartheta = \theta_{A',cm}$, while a is defined as half the distance of closest approach:

$$a = \frac{b}{2} = \frac{Z_A Z_B e^2}{\mu v^2}. \quad (\text{B.3})$$

Above, Z_A and Z_B are the atomic numbers for the projectile and target, respectively, while v is the relative velocity of the projectile and target. (Since the target is at rest initially, $v = v_A$.) The parameter μ represents the reduced mass of the projectile + target system, $\mu \equiv m_A m_B / (m_A + m_B)$. It should be mentioned that excitation of the projectile or the target is dealt with in an equivalent manner. For the remainder of this discussion, however, we will assume projectile excitation; all expressions to follow are valid for target excitation with a simple exchange, $Z_A \leftrightarrow Z_B$.

The excitation process is understood as resulting from interactions of the projectile with the time-dependent electromagnetic field, $V(\mathbf{r}(t))$, which sweeps over the projectile as it passes the target. From first-order perturbation theory we have

$$P_{i \rightarrow f} = |a_{i \rightarrow f}|^2, \quad \text{where} \quad a_{i \rightarrow f} = \frac{1}{i\hbar} \int_{-\infty}^{\infty} \langle f | V(\mathbf{r}(t)) | i \rangle e^{i(E_f - E_i)t/\hbar} dt \quad (\text{B.4})$$

is the amplitude of the process which takes the projectile from state i into state f . The electromagnetic interaction, $V(\mathbf{r}(t))$, includes contributions from both electric and magnetic multipoles. For this study it was sufficient to consider only electric contributions ($\lambda = 1 - 3$). As outlined in Ref. 1, the electric amplitude can be written as

$$a_{i \rightarrow f} = \frac{4\pi Z_B e}{i\hbar} \sum_{\lambda, \mu} \frac{1}{2\lambda + 1} \langle I_i M_i | \mathcal{M}(E\lambda, \mu) | I_f M_f \rangle^* S_{E\lambda\mu} . \quad (\text{B.5})$$

Defined in such a way, the nuclear properties enter the amplitude only through the electric multipole matrix elements, $\langle I_i M_i | \mathcal{M}(E\lambda, \mu) | I_f M_f \rangle^*$, while the kinematics of the collision are contained solely in the orbital integrals, $S_{E\lambda\mu}$, which are given by

$$S_{E\lambda\mu} = \int_{-\infty}^{\infty} \frac{Y_{\lambda\mu}[\theta(t), \phi(t)]}{r(t)^{\lambda+1}} e^{i(E_f - E_i)t/\hbar} dt . \quad (\text{B.6})$$

To further isolate the nuclear properties, the multiple matrix elements themselves are expressed as a product of a Wigner 3-j symbol, which is the contribution from angular momentum geometry, and a reduced matrix element, e.g.,

$$\langle I_i M_i | \mathcal{M}(E\lambda, \mu) | I_f M_f \rangle = (-1)^{I_i - M_i} \begin{pmatrix} I_i & \lambda & I_f \\ -M_i & \mu & M_f \end{pmatrix} \langle I_i || \mathcal{M}(E\lambda) || I_f \rangle . \quad (\text{B.7})$$

The complex orbital integrals, $S_{E\lambda\mu}$, can be re-expressed as

$$S_{E\lambda\mu} = \frac{1}{a^{\lambda\nu}} \frac{(\lambda - 1)!}{(2\lambda - 1)!!} \sqrt{\frac{2\lambda + 1}{\pi}} R_{\lambda\mu}(\vartheta, \xi) \quad (\text{B.8})$$

where ξ is defined as the adiabaticity parameter:

$$\xi = \frac{a}{v} \frac{E_f - E_i}{\hbar} . \quad (\text{B.9})$$

Qualitatively speaking, the adiabaticity parameter can be thought of as the ratio of the collision time (or amount of time the projectile spends within the target field) and the characteristic nuclear period associated with the small change in energy, $E_i \rightarrow E_f$. This quantity must be comparable or less than unity for the transition $|i\rangle \rightarrow |f\rangle$ to occur – for larger values of ξ the nucleus will follow the perturbation due to the potential adiabatically [1]. Given an incident beam energy, ξ therefore provides an upper limit on the energy which the participating nuclei can absorb during any virtual excitation process.

The form of the new orbital integrals, $R_{\lambda\mu}(\vartheta, \xi)$, which appear in Eq. B.8 is introduced through the relation:

$$\begin{aligned} R_\lambda^2(\vartheta, \xi) &= \sum_{\mu} |R_{\lambda\mu}(\vartheta, \xi)|^2 \\ &= \left| \frac{(2\lambda - 1)!!}{(\lambda - 1)!} \right|^2 \frac{\pi}{2\lambda + 1} \sum_{\mu} |Y_{\lambda\mu}(\pi/2, 0) I_{\lambda\mu}(\vartheta, \xi)|^2 . \end{aligned} \quad (\text{B.10})$$

The $I_{\lambda\mu}(\vartheta, \xi)$ functions appearing in Eq. B.10 are defined in Ref. 1 as the Coulomb excitation functions, which have the form

$$I_{\lambda\mu}(\vartheta, \xi) = \int_{-\infty}^{\infty} \frac{(\varepsilon + \cosh w + i\sqrt{\varepsilon^2 - 1} \sinh w)^\mu}{(1 + \varepsilon \cosh w)^{\lambda + \mu}} e^{i\xi(\varepsilon \sinh w + w)} dw , \quad (\text{B.11})$$

where λ and μ are integer values, with $\lambda \geq 0$. The variable ε used above represents the eccentricity of the hyperbolic orbit, which is purely a function of the scattering angle ϑ .

$$\varepsilon = \frac{1}{\sin\left(\frac{\vartheta}{2}\right)} . \quad (\text{B.12})$$

It is worthy to note that, defined as such, the $I_{\lambda\mu}(\vartheta, \xi)$ functions are real, i.e.,

$$I_{\lambda\mu}(\vartheta, \xi) = I_{\lambda\mu}^*(\vartheta, \xi) .$$

As will be discussed in Section B.3, the $I_{\lambda\mu}(\vartheta, \xi)$ functions can be calculated numerically using MATHEMATICA [36] for all values of ϑ and ξ . Such numerical solutions are rather computationally intensive. The approximation

$$I_{\lambda\mu}(\vartheta, \xi) \simeq \frac{(-1)^{(\lambda-\mu)/2}}{\varepsilon} \left(\frac{\xi}{2\varepsilon}\right)^{(\lambda-1)/2} \Gamma\left(\frac{-\lambda + \mu + 1}{2}\right) e^{-\pi\xi/2} W_{-\frac{\mu}{2}-\frac{\lambda}{2}}(2\xi\varepsilon), \quad (\text{B.13})$$

which holds for small scattering angles, ϑ , was especially useful for the current study since the scattering angles of $^{18,20}\text{O}$ were limited to a small forward cone. The $W_{-\frac{\mu}{2}-\frac{\lambda}{2}}(2\xi\varepsilon)$ quantities in Eq. B.13 are Whittaker functions, which are related to confluent hypergeometric functions, $U(a, c; z)$ [4]. Specifically,

$$W_{lm}(x) = e^{-x/2} x^{m+1/2} U(m-l+1/2, 2m+1; x). \quad (\text{B.14})$$

Rewriting the expression for the differential Coulomb excitation cross section (Eq. B.1) while making use of the definitions in Equations B.8, B.10, and B.11, along with the expression for the contribution from nuclear properties, Eq. B.7, we have

$$\frac{d\sigma_{E\lambda}}{d\Omega} = \left(\frac{Z_B e}{\hbar v}\right)^2 a^{-2\lambda+2} B(E\lambda, I_i \rightarrow I_f) \frac{df_{E\lambda}(\vartheta, \xi)}{d\Omega}. \quad (\text{B.15})$$

Above, we have used the definition for the so-called differential cross section functions,

$$\frac{df_{E\lambda}(\vartheta, \xi)}{d\Omega} = 4\pi \left| \frac{(\lambda-1)!}{(2\lambda+1)!!} \right|^2 R_\lambda^2(\vartheta, \xi) \sin^{-4}\left(\frac{\vartheta}{2}\right), \quad (\text{B.16})$$

along with the expression for the reduced transition probability:

$$\begin{aligned} B(E\lambda, I_i \rightarrow I_f) &= \frac{1}{2I_f + 1} |\langle I_i || \mathcal{M}(E\lambda) || I_f \rangle|^2 \\ &= \frac{1}{2I_i + 1} |\langle I_f || \mathcal{M}(E\lambda) || I_i \rangle|^2. \end{aligned} \quad (\text{B.17})$$

B.2 Quantum mechanical corrections

Up to this point the classical portion of this Coulomb excitation treatment has neglected projectile energy-loss due to inelastic processes. One might expect that better solutions for the Coulomb cross section might be found by replacing v with some average velocity of the projectile over its trajectory. In fact, following the logic introduced in Ref. 1, which makes use of quantum mechanical symmetry arguments, it is realized that an improvement to this semi-classical approach is achieved if one uses “symmetrized” expressions for a and ξ . By these arguments, the (relative) velocity, v , in the expressions for a and ξ (Equations B.3 and B.9, respectively) should be replaced by the average velocity of the projectile before and after the collision, i.e., $v \rightarrow v_{sym} = (v_A + v_{A'})/2$, so that

$$\begin{aligned}
 a \rightarrow a_{sym} &= \frac{Z_A Z_B e^2}{\mu v_{sym}^2} \\
 &= \frac{Z_A Z_B e^2}{\mu v_A v_{A'}} \\
 \xi \rightarrow \xi_{sym} &= \left(\frac{a_{sym}}{v_{sym}} \right) \frac{E_f - E_i}{\hbar} \\
 &= \frac{Z_A Z_B e^2}{\hbar} \left(\frac{1}{v_{A'}} - \frac{1}{v_A} \right). \tag{B.18}
 \end{aligned}$$

Hence, we arrive at the corrected version of the Coulomb excitation cross section,

$$\frac{d\sigma_{E\lambda}}{d\Omega} \rightarrow \left(\frac{d\sigma_{E\lambda}}{d\Omega} \right)_{sym} = \left(\frac{Z_B e}{\hbar v} \right)^2 a_{sym}^{-2\lambda+2} B(E\lambda, I_i \rightarrow I_f) \frac{df_{E\lambda}(\vartheta, \xi_{sym})}{d\Omega}. \tag{B.19}$$

B.3 Differential cross section functions

As mentioned in Sec. B.1, of specific importance to this study were contributions to the virtual photon flux from three electric multipoles, namely $E1$, $E2$, and $E3$. Therefore, discussion for the remainder of this appendix will focus on a more detailed derivation

of the differential cross section functions, $df_{E\lambda}(\vartheta, \xi)/d\Omega$, for the three pertinent values of λ . Notice that the arguments of the spherical harmonics ($Y_{\lambda\mu}(\theta, \phi)$) appearing in Eq. B.10 are constants. Specifically, $\theta = \pi/2$ and $\phi = 0$. Given the property of these functions that the product of μ and the argument ϕ determines the complex contribution, with all $\phi = 0$, we have the special situation where

$$Y_{\lambda\mu} = Y_{\lambda\mu}^* ,$$

i.e., all $Y_{\lambda\mu}$ coefficients in Eq. B.10 are real. Therefore, given the reflection properties of the spherical harmonics, this implies

$$Y_{\lambda-\mu} = (-1)^\mu Y_{\lambda\mu}^* = (-1)^\mu Y_{\lambda\mu} .$$

Hence,

$$Y_{\lambda-\mu}^2 = Y_{\lambda\mu}^2 .$$

Meanwhile, the fact that the argument θ takes on the value $\pi/2$ for all (λ, μ) gives us

$$Y_{10} = Y_{2\pm 1} = Y_{30} = Y_{3\pm 2} = 0 .$$

Using the specific values for the remaining $Y_{\lambda\mu}$ coefficients, along with the fact that all $I_{\lambda\mu}(\vartheta, \xi)$ are real, we arrive at the following expressions for the differential cross section functions:

$$\begin{aligned}
\frac{df_{E1}(\vartheta, \xi)}{d\Omega} &= \left(\frac{1}{27}\right) \frac{4\pi^2}{\sin^4(\frac{\vartheta}{2})} \left(\frac{3}{8\pi}\right) \{I_{1-1}^2(\vartheta, \xi) + I_{11}^2(\vartheta, \xi)\} \\
\frac{df_{E2}(\vartheta, \xi)}{d\Omega} &= \left(\frac{1}{125}\right) \frac{4\pi^2}{\sin^4(\frac{\vartheta}{2})} \left[\left(\frac{15}{32\pi}\right) \{I_{2-2}^2(\vartheta, \xi) + I_{22}^2(\vartheta, \xi)\} + \left(\frac{5}{16\pi}\right) I_{20}^2(\vartheta, \xi) \right] \\
\frac{df_{E3}(\vartheta, \xi)}{d\Omega} &= \left(\frac{1}{343}\right) \frac{4\pi^2}{\sin^4(\frac{\vartheta}{2})} \times \\
&\quad \left[\left(\frac{35}{64\pi}\right) \{I_{3-3}^2(\vartheta, \xi) + I_{33}^2(\vartheta, \xi)\} + \left(\frac{21}{64\pi}\right) \{I_{3-1}^2(\vartheta, \xi) + I_{31}^2(\vartheta, \xi)\} \right].
\end{aligned}
\tag{B.20}$$

MATHEMATICA [36] was used to generate both the exact versions of Eq. B.20 (solid curves), which were calculated using numerical solutions for the $I_{\lambda\mu}(\vartheta, \xi)$ functions (given by Eq. B.11), and the (small-angle) approximate curves (dashed), which used

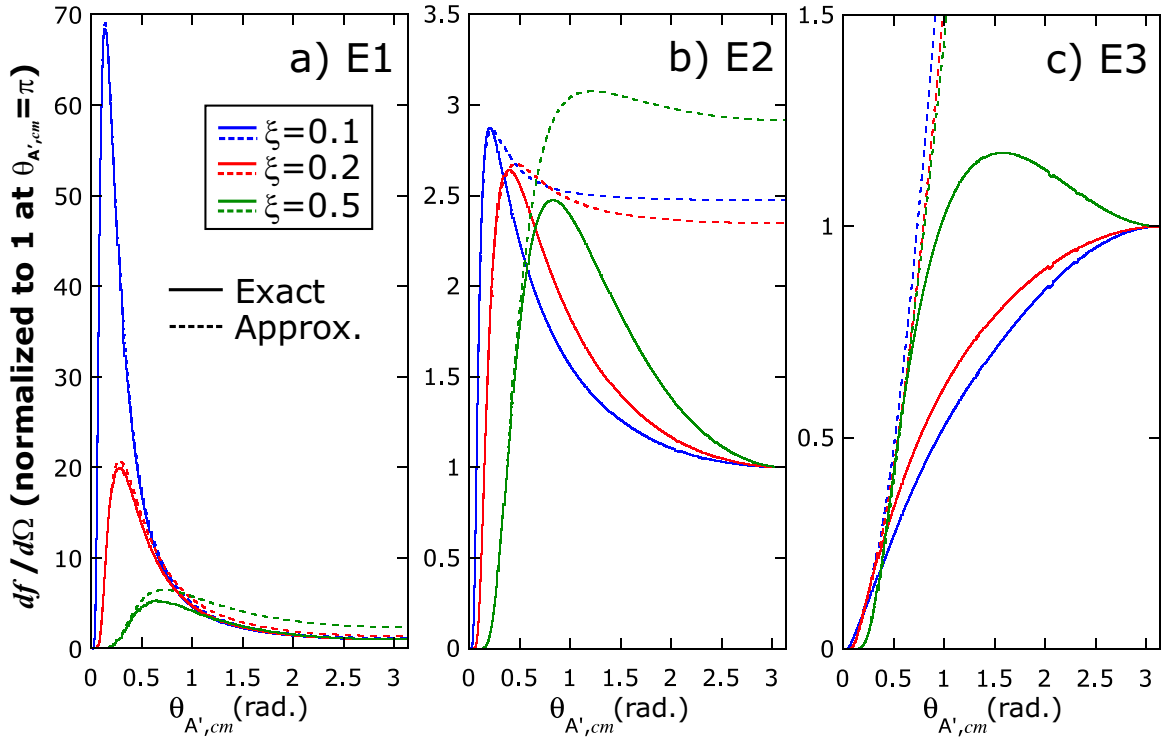


Figure B.2: Differential cross section functions, $df_{E\lambda}(\vartheta, \xi)/d\Omega$ for $E1$ (a), $E2$ (b), and $E3$ (c) excitations, shown for different values of the adiabaticity parameter, ξ . The solid curves were generated using numerical solutions for the exact expressions, $I_{\lambda\mu}(\vartheta, \xi)$ (Eq. B.11), while the dashed curves were generated using the small-angle approximate solutions for $I_{\lambda\mu}(\vartheta, \xi)$ (Eq. B.13). The functions $df_{E\lambda}(\vartheta, \xi)/d\Omega$ have been normalized such that the exact curves are unity at $\theta_{A',cm}=\pi$. Table B.1 gives the appropriate multiplication factors.

Table B.1: The factors by which the curves in Fig. B.2 should be multiplied

	$\xi=0.1$	$\xi=0.2$	$\xi=0.5$
$df_{E1}(\vartheta, \xi)/d\Omega$	9.19 E -1	5.62 E -1	1.12 E -1
$df_{E2}(\vartheta, \xi)/d\Omega$	4.97 E -2	3.89 E -2	1.32 E -2
$df_{E3}(\vartheta, \xi)/d\Omega$	4.32 E -3	3.76 E -3	1.76 E -3

Eq. B.13 to generate the $I_{\lambda\mu}(\vartheta, \xi)$'s. Some examples are given in Fig. B.2 for different values of adiabaticity ($\xi=0.1, 0.2, 0.5$) and virtual photon multipolarity. For reference, the adiabaticity parameter for the ^{20}O study was ~ 0.018 . The curves in Fig. B.2 have been normalized such that the exact solutions, shown as the solid lines, are unity at $\theta_{A', cm}=\pi$. The factors by which the curves in Fig. B.2 should be multiplied are given in Table. B.1.

As evidenced by Fig. B.2, the approximate solutions for the differential cross section functions are accurate up to $\vartheta \simeq 0.5$ radians, which is a region which extends well beyond the angular acceptance for these experiments. Moreover, the approximate solution is better for lower multipolarity. Indeed, for the specific case of $E1$ excitations, the approximate solution for small adiabaticity is seemingly valid for all ϑ . The approximate solutions, which were much less computationally demanding, were therefore used for all Coulomb cross section calculations that went into the Monte Carlo simulation, the details of which are included in Chapter 4.

Bibliography

- [1] K. Alder and A. Winther. *Electromagnetic excitation: theory of Coulomb excitation with heavy ions*. North-Holland Publishing Company, 1st edition, 1975.
- [2] P. Andersson, L. P. Ekström, and J. Lyttkens. Nuclear data sheets for $A=60$. *Nucl. Data Sheets*, **48**:251–344, 1986.
- [3] Application Software Group, Computing and Networks Division, CERN, Geneva Switzerland. *GEANT – detector description and simulation tool*, 1993.
- [4] G. Arfken. *Mathematical methods for physicists*. Academic Press, Inc., 3rd edition, 1985.
- [5] T. Aumann, A. Leistenschneider, K. Boretzky, D. Cortina, J. Cub, W. Dostal, B. Eberlein, T. W. Elze, H. Geissel, A. Grünschloß, M. Hellström, J. Holeczek, R. Holzmann, S. Ilievski, N. Iwasa, M. Kaspar, A. Kleinböhl, J. Kratz, R. Kulesa, Y. Leifels, E. Lubkiewicz, G. Münzenberg, P. Reiter, M. Rejmund, C. Scheidenberger, C. Schlegel, H. Simon, J. Stroth, K. Sümmerer, E. Wajda, W. Walus, and S. Wan. Giant resonances in unstable oxygen isotopes. *Nucl. Phys. A*, **649**:297c–304c, 1999. Proceedings of the Giant Resonance 98 conference, Varenna, Italy, 1998.
- [6] C. A. Bertulani and A. M. Nathan. Excitation and photon decay of giant resonances from high-energy collisions of heavy ions. *Nucl. Phys. A*, **554**:158–172, 1993.
- [7] M. Berz, K. Joh, J. A. Nolen, B. M. Sherrill, and A. F. Zeller. Reconstructive correction of aberrations in particle spectrographs. *Phys. Rev. C*, **47**:537–544, 1993.
- [8] M. R. Bhat. Nuclear data sheets for $A=58$. *Nucl. Data Sheets*, **80**:789–893, 1997.
- [9] B. A. Brown. Private communications.
- [10] J. A. Caggiano. *Spectroscopy of exotic nuclei with the S800 spectrograph*. PhD thesis, Michigan State University, 1999.
- [11] J. A. Cameron and B. Singh. Nuclear data sheets for $A=44$. *Nucl. Data Sheets*, **88**:299–416, 1999.

- [12] F. Catara, E. G. Lanza, M. A. Nagarajan, and A. Vitturi. Effect of large neutron excess on the dipole response in the region of the giant dipole resonance. *Nucl. Phys. A*, **624**:449–458, 1997.
- [13] H. Goldstein. *Classical mechanics*. Addison-Wesley, 2nd edition, 1980.
- [14] I. Hamamoto and H. Sagawa. Low energy strength in low-multipole response function of nuclei near the neutron drip line. *Phys. Rev. C*, **53**:R1493–R1496, 1996.
- [15] K. Heyde. *Basic Ideas and Concepts in Nuclear Physics*. Institute of Physics Publishing, 2nd edition, 1999.
- [16] J. D. Jackson. *Classical electrodynamics*. John Wiley & Sons, Inc., 2nd edition, 1975.
- [17] J. W. Jury, B. L. Berman, D. D. Faul, P. Meyer, and J. G. Woodworth. Photon-neutron cross sections for ^{17}O . *Phys. Rev. C*, **21**:503–511, 1980.
- [18] W. Klamra, T. Lindblad, M. Moszyński, and L. O. Norlin. Properties of optical greases for BaF_2 scintillators. *Nucl. Instr. and Meth. A*, **254**:85–87, 1987.
- [19] G. F. Knoll. *Radiation detection and measurement*. John Wiley & Sons, Inc., 3rd edition, 2000.
- [20] M. Laval, M. Moszyński, R. Allemand, E. Cormoreche, P. Guinet, R. Odru, and J. Vacher. Barium fluoride – inorganic scintillator for subnanosecond timing. *Nucl. Instr. and Meth.*, **206**:169–176, 1983.
- [21] A. Leistenschneider, T. Aumann, K. Boretzky, D. Cortina, J. Cub, U. D. Pramanik, W. Dostal, T. W. Elze, H. Emling, H. Geissel, A. Grünschloß, M. Hellström, R. Holzmann, S. Ilievski, N. Iwasa, M. Kaspar, A. Kleinböhl, J. Kratz, R. Kulesa, Y. Leifels, E. Lubkiewicz, G. Münzenberg, P. Reiter, M. Rejmund, C. Scheidenberger, C. Schlegel, H. Simon, J. Stroth, K. Sümmerer, E. Wajda, W. Walús, and S. Wan. Photoneutron cross sections for unstable neutron-rich oxygen isotopes. *Phys. Rev. Lett.*, **86**:5442–5445, 2001.
- [22] D. M. Manley, B. L. Berman, W. Bertozzi, T. N. Buti, J. M. Finn, F. W. Hersman, C. E. Hyde-Wright, M. V. Hynes, J. J. Kelly, M. A. Kovash, S. Kowalski, R. W. Lourie, B. Murdock, B. E. Norum, B. Pugh, C. P. Sargent, and D. J. Milener. Electroexcitation of negative-parity states in ^{18}O . *Phys. Rev. C*, **43**:2147–2161, 1991.
- [23] M. J. Martin. Nuclear data sheets for $A=208$. *Nucl. Data Sheets*, **47**:797–964, 1986.
- [24] A. M. Nathan. Statistical and nonstatistical photon emission from giant resonances. *Phys. Rev. C*, **43**:R2479–R2482, 1991.

- [25] W. H. Press, S. A. Teukolsky, W. T. Vetterling, and B. P. Flannery. *Numerical Recipes in FORTRAN: the Art of Scientific Computing*. Cambridge University Press, 2nd edition, 1992.
- [26] S. Raman, C. W. N. Jr., S. Kahane, and K. H. Bhatt. Predictions of $B(E2) \uparrow$ values. *At. Data and Nucl. Data Tables*, **42**:1–54, 1989.
- [27] H. Sagawa and T. Suzuki. Pigmy and giant dipole states in oxygen isotopes. *Phys. Rev. C*, **59**:3116–3119, 1999.
- [28] N. P. Shaw. *High energy γ -rays from highly excited thorium, californium, and meitnerium*. PhD thesis, State University of New York at Stony Brook, 1999.
- [29] B. M. Sherrill, D. J. Morrissey, J. A. N. Jr., N. Orr, and J. A. Winger. Initial operating experience with the a1200 fragment separator. *Nucl. Instr. and Meth. B*, **70**:298–303, 1992.
- [30] B. Singh and J. A. Cameron. Nuclear data sheets for $A=42$. *Nucl. Data Sheets*, **92**:1–146, 2001.
- [31] R. H. Spear. $B(E3) \uparrow$ to the First 3^- State. *At. Data and Nucl. Data Tables*, **42**:55–104, 1989.
- [32] T. Suzuki and H. Sagawa. Private communications.
- [33] O. Tarasov and D. Bazin, Aug. 2001. Documentation on program LISE is available online at: <http://www.nucl.msu.edu/~tarasov/lise/lise.html>.
- [34] D. R. Tilley, C. M. Cheves, J. H. Kelley, S. Raman, and R. H. Weller. Energy levels of light nuclei $A=20$. *Nucl. Phys. A*, **636**:249–364, 1998.
- [35] D. R. Tilley, H. R. Weller, C. M. Cheves, and R. M. Chasteler. Energy levels of light nuclei $A=18-19$. *Nucl. Phys. A*, **595**:1–170, 1995.
- [36] S. Wolfram. *The MATHEMATICA book*. Cambridge University Press and Wolfram Media, 4th edition, 1999.
- [37] J. Yurkon, D. Bazin, W. Benenson, D. J. Morrissey, B. M. Sherrill, D. Swan, and R. Swanson. Focal plane detector for the S800 high-resolution spectrometer. *Nucl. Instr. and Meth. A*, **422**:291–295, 1999.